DIRECT INK WRITING OF HIGH-STRENGTH POLYMER COMPOSITES

A Dissertation

by

ZIMENG ZHANG

Submitted to the Office of Graduate and Professional Studies of
Texas A&M University
in partial fulfillment of the requirements for the degree of

DOCTOR OF PHILOSOPHY

Chair of Committee,	Shiren Wang
Committee Members,	Alaa Elwany
	Zhijian Pei
	Choongho Yu
Head of Department,	Lewis Ntaimo

May 2021

Major Subject: Industrial Engineering

ABSTRACT

Polymeric composites with various functionalities are widely used in the aerospace, automotive, medical industries. Direct ink writing (DIW) is an extrusion-based 3D printing method that builds the object from 3D model data in a layer-by-layer fashion. In this dissertation, high-performance thermosetting polymers, thermosetting composites, and hydrogels were printed via DIW. Modifications on printing material formulations were made for either advancing the manufacturing process with improved production efficiency or enhancing the material performance.

Firstly, an energy-efficient and rapid frontal curing assisted in-situ printing-and-curing process was developed for epoxy resin-based thermosets and composites fabrication. The dual initiating systems consisting of cationic and thermal initiators were incorporated for epoxy resin's frontal propagation. Reducing the cationic initiator concentration from 2mol% to 0.05 mol% can lower the front temperature from ~290°C to ~240°C. Nano/micro-filler was incorporated as catalysts to further reduce the front temperature by tuning the reaction profile. With the incorporation of 1wt% CNT, the front temperature can be reduced to ~227.14°C while the front velocity remains (~6 cm min^{-1}). The as-developed printing process was furthered extended to continuous carbon fiber reinforced thermosetting composites (c-CFRC) fabrication with an exceptional tensile strength of ~1.147 GPa with a fiber volume ratio of 48%. This new process could potentially lead to 3.6 billion kilowatt-hours (kWh)/year energy-saving in comparison to traditional oven curing processes.

Secondly, carbon fibers with modified surface chemistry were incorporated for frontal polymerization enabled printing of dicyclopentadiene (DCPD) composites. Norbornene functional groups were grafted onto the carbon fiber surface for an in-situ filler-polymer matrix interface enhancement via frontal polymerization. Incorporation of 3wt% norbornene-grafted discontinuous carbon fibers (CFs) led to 1.7- and 2.6-folds enhancement in tensile and interlayer bonding strength with reference to the neat resin, respectively.

Lastly, single network hydrogel with phenyl acrylate (PA), and soft acrylamide (AAm) components were printed and crosslinked under ultraviolet irradiation for load bearing tissue applications. Cellulose nanocrystal (CNC) was added for rheology modifications. Hydrogel with a PA/AAm ratio of 3:2 demonstrates a tensile strength of ~4.4 MP and toughness of ~6 MJ m^{-3}.

To my parents for their scarification and constant support

ACKNOWLEDGEMENTS

I would like to express my deepest gratitude and appreciation to my advisor Dr. Shiren Wang for his constant support of my doctoral education and related research, for his instructions, motivation, patience and immense knowledge. His persistent and unwavering enthusiasm for research kept me engaged in my research. His personal generosity made my research journey more colorful and more enjoyable. Without his excellent guidance and dedication, this dissertation would not have been possible.

My appreciation also extends to my committee members, Dr. Alaa Elwany for his insightful comments, encouragement and invaluable suggestions that helps my career, Dr. Zhijian Pei for his guidance on thermosetting polymer printing related research and Dr. Choongho Yu for his profound knowledge input in heat transfer.

My sincere thanks also go to Dr. Li Zeng, who helped me revise papers on hydrogel printing for healthcare applications, as well as Dr. Lei Fang from Department of Chemistry of Texas A&M University and Dr. Jingjing Qiu from Texas Tech University for their generous support on my research.

I would also like to thank staff Shannon Caldwell and Amanda Myatt for their support on lab equipment setup and training.

Thanks also go to my husband Haochen for his encouragement and support during my Ph.D. I would also like to thank my friends (Jingyuan, Fangbing, Afrin, Asif, Qian, Yu, Jin, Jiangyue, Zimo), colleagues (Yuchen, Wei, Ruochen, Jun, Chongjie, Biran, Liming, Xin), and Aggie challenge teammates.

CONTRIBUTORS AND FUNDING SOURCES

Contributors:

This work was supervised by a dissertation committee consisting of Professor Shiren Wang (chair), Alaa Elwany and Zhijian Pei from the Department of Industrial and Systems Engineering and Professor Choongho Yu from the Department of Mechanical Engineering.

Colleague Ruochen Liu helped with the sample preparation in Chapters 4 and 5.

All other work conducted for the thesis (or) dissertation was completed by the student independently.

Funding Sources

Graduate study was supported by a fellowship from Texas A&M Engineering Experiment Station and a dissertation research fellowship from National Science Foundation (CMMI-1634858, CMMI-1933679).

TABLE OF CONTENTS

Page

LIST OF FIGURES

Page

LIST OF TABLES

Page

CHAPTER I

INTRODUCTION

The emerging technology, additive manufacturing, also known as 3D printing, was first introduced by Charles Hull in the year of 1983 to serve the customized needs of model making and rapid prototyping specifically for polymeric materials. In contrast to traditional manufacturing, objects are constructed and formed in a layer-by-layer fashion in the 3D space. Recent decades witnessed the ever-changing development of 3D printing, expanding its capability in a wide range of materials including polymers (thermosets and thermoplastics) metals as well as ceramics. Meanwhile, a number of different printing modalities have been discovered including stereolithography (SLA), filament fused fabrication (FFF), material jetting (MJ), binder jet (BJ), selective laser sintering (SLS), selective laser melting (SLM), and etc. to improve the manufacturability as well as the production rate for industrial applications. To date, 3D printing has presented its potential in a variety of industries including but not limited to aerospace, automotive, marine, medical, coating, oil & gas. With the new materials discovered and process advances, 3D printing technology could further expand its application and advance industrial production with more flexibility and versatility. In this dissertation, novel polymeric materials, thermosets, and synthetic hydrogels were designed and studied for their printability and processability in the direct ink writing (DIW) field, and their applications in the corresponding industries.

1.1 Motivation

1.1.1 Energy efficient and rapid manufacturing for thermosetting polymers

Thermosetting polymers such as epoxy resin, polyimide, cyanate ester, etc., have wide-spread applications in aerospace, military, automotive, infrastructure, sports, pipeline industries and etc. for their lightweight, exceptional mechanical performance as well as outstanding thermal and chemical resistance[1-6]. The thermosetting polymers are conventionally fabricated by molding and subsequent thermal curing[7]. Conventional photo-curable thermosets are restrained in this molding process due to their limited penetration depth. In addition, for conventional molding, it is difficult to produce parts with complex geometries and the mold significantly increases the manufacturing cost especially in industrial applications[8, 9]. 3D printing constructs objects in a layer-by-layer fashion providing a mold-free solution to overcome the drawbacks of conventional molding.

Previous endeavors of 3D printing thermosets and their composites include extrusion-based printing, stereolithography (SLA), digital light processing (DLP), and selective laser sintering (SLS). Compared to the other three technologies, extrusion-based printing eliminates the use of energy-intensive and costly laser apparatus, an incomplete cure for limited light penetration depth, and light pollution problems. Thus, it demonstrated great promise in constructing thermosets and composites. Current 3D printing of high-performance thermosetting polymers involves a typical two-step process similar to the molding-based process, printing the structure and subsequently ex-situ

thermal curing in ovens or autoclaves. The ex-situ curing at high-temperature and extended curing time (usually several hours) after printing consume an excessive amount of energy[8, 9]. Therefore, in the consideration of energy-efficiency in the manufacturing of high-performance thermosetting polymers, the one-step mold-free method is highly desirable.

Frontal curing is a process in which curing occurs directionally in a self-propagating reaction zone by coupling thermal diffusion and the exothermic Arrhenius reaction. Specifically, the reaction process can be described as below. The front is generated by an initial thermal energy or light irradiation and sustained from the exothermic reaction. Then, the heat dissipates into the adjacent area increasing the temperature and accelerating the reaction temperature in that region. The reaction is propagating along the print-path as a thermal wave. Applying frontal curing reaction in the 3D printing process has the potential to realize the one-step fabrication of printing and in-situ curing of thermosetting polymer and composites. By eliminating the ex-situ process, it is able to save the manufacturing time by up to 100 times and reduce energy consumption by up to 10 billion times for manufacturing an airplane fuselage composites part[10]. The research covered in this dissertation will focus on localized frontal curing-assisted 3D printing of thermosetting polymers and composites.

1.1.2 High-performance hydrogel printing for healthcare application

Donor shortage is a commonly faced scenario for clinical treatments. Limited donor supply, shape mismatch, and biocompatibility are the limitations for traditional organ/ tissue transplantation. Artificial tissues produced by the various bio-fabrication

techniques are one promising method to deal with those issues. The meniscus, a wedge-shaped piece of fibrocartilaginous tissue that acts as a "cushion" in the knee joint is a typical type of tissue targeted for tissue regeneration. It is reported that each year about 1.5 million people need meniscus treatments in the US and Europe[11-14]. Thus, fabricating the artificial meniscus is highly demanded.

Hydrogels that contain 90% of water and macromolecules serve as one common biomaterial for artificial tissues because of their similarity to extracellulose matrix (ECM) and it is prevalent in today's load-bearing tissue fabrication. Different types of hydrogels were fabricated via molding, such as nanocomposites (NC) gel[15-17], double network (DN) gel[18-20], slide-ring (SR) gel[21, 22], and ionic-covalent entanglement (ICE) gel[23, 24]. However, the molding process is difficult to keep the precise geometry features of the fabricated tissue. Geometrical inaccuracy will lead to mismatch problems in transplantation, especially for meniscus which requires high dimensional accuracy. 3D printing is a state-of-art technique to fabricate biological tissues for its geometry flexibility and ease-of-process comparing to traditional fabrication methods.

1.2 Technical challenge

1.2.1 Energy efficient and rapid manufacturing for thermosetting polymers

Though 3D printing offers exceptional flexibility and complexity, the mechanical performance of the printed part is relatively low compared to conventional molded ones because there only exists physical contact between the two adjacent filaments and lacks the strong interlayer bonding. Efforts have been made to improve the interlayer adhesion via introducing additives onto the filament surface or forming new chemical bonds. Both

methods require external thermal treatment after printing which causes extra energy consumption. Thus, there lacks an energy-efficient way of improving interfacial bonding and further enhancing the overall mechanical performance.

Another technical challenge for 3D printing is the limited functionalities of the printed parts. Thus, there is a critical need to develop novel printable thermosetting polymers and their composites materials, especially for frontal curable thermosetting polymers with great promise in energy-efficient manufacturing. Previous attempts demonstrated printing and in-situ curing concept to highly reactive thermosets, dicyclopentadiene (DCPD)[10]. However, the expansion of the frontal assisted in-situ curing to other thermoset resins with relatively lower reactivity remains to be challenging. So it is imperative to explore highly efficient catalytic systems for low reactivity thermoset resins for frontal curing.

In addition to the study of frontal curable resins, recent research trends lie in the direction of developing automated manufacturing technology for low-cost continuous carbon fiber-reinforced polymer composites (c-CFRC) with high design flexibility. One of the technical challenges here is the printing process modifications to improve the mechanical performance of the printed part. These modifications include resin incorporation, continuous fiber feeding, print path generation, and control of the fiber volume fraction which will affect the mechanical performance. The incorporation of frontal curable resin introduces another challenge in the manufacturing of c-CFRC: the sustaining front requires a sufficient number of reactive resins for Arrhenius dependent exothermic reaction, which in turn limit the fiber volume fraction in c-CFRC. Thus, further

improvement of resin reactivity, resin-fiber contact for better thermal transport, and fiber thermal conductivity for efficient heat conductance plays an important factor in achieving high-performance part fabrication. Besides, the analysis of thermal transport in the combination with the reaction kinetics is critical in determining the effect of each component in the frontal curing assisted c-CFRC printing process.

1.2.2 High-performance hydrogel printing for healthcare application

The main challenge of printing hydrogels for load-bearing tissue applications would be the deficiency in mechanical performance. Previous endeavors have been devoted to modifying the polymer networks with different types of chemical bonds, or the chain-chain interaction when multiple types of networks are included. For the traditional molding process, the constructs formed as a whole piece without any interfacial gaps. However, the nature of successive layer fashion of 3D printing tends to interfere with the overall mechanical performance of the printed constructs. Further, for high-performance hydrogel (especially high-performance DN gel), polymer chain interpenetration among different types of networks influences a lot of mechanical performance. But in 3D printing, it is hard to control the polymer formation sequence in one step. For example, the PAMPS/PAAm DN gel demonstrated tensile strength up to 10 MPa for the molded part, but only a tenth of the tensile strength was achieved for 3D printed one[19, 25, 26]. The exceptional properties of the molded gel were due to the well-controlled crosslinking density (tightly crosslinked first network and loosely crosslinked second network) and well interpenetration of the networks[27]. So, herein, the major challenge is to improve the

mechanical properties of printed hydrogels via polymer network modification as well as the process advances.

1.3 Research objectives

To realize the full potential of frontal curing in printing thermosetting polymer and composites as well as the high-performance hydrogel printing for healthcare applications, three research objectives will be proposed and studied in this dissertation.

First, a frontal curable epoxy will be studied and discussed in Chapter III. A sustaining front of epoxy is generated with the addition of a two-component initiating system followed by a radical-induced cationic frontal curing (RICFC) mechanism. The frontal velocity and frontal temperature were analyzed for the adoption in the 3D printing process. Further research will aim at reducing the frontal temperature while maintaining the frontal velocity, the regulation of frontal curing, and synchronized printing process by both numeric modeling and experiments. Cationic initiator and thermal initiator concentration will be used tuned to control the frontal velocity and frontal temperature. Further, thermal conductive micro-/nanofillers will then be incorporated to help reduce the frontal velocity. The frontal curable resins will be coated onto the continuous carbon fiber tows for the fabrication of the epoxy resin-based thermosetting continuous carbon fiber reinforced composites (c-CFRC). The printing setup for the fabrication of c-CFRC was designed and printing capability was demonstrated. A resin reservoir will be added for better resin-fiber coating. The effect of thermal transport for the frontal process with the incorporation of continuous fiber will be studied theoretically and experimentally.

Second, a method of enhancing the mechanical performance of frontally cured and in-situ printed parts is proposed with the incorporation of functionalized carbon fibers. The proposed method incorporates micro-filler with surface modification for forming the covalent bonds between polymer chain and micro-filler, thus may improve the interlayer bonding between resins and fibers. The formation of the covalent bonds follows the same reaction mechanism as the monomer in polymer matrix without external energy supply. So, no further treatments are needed after printing. Chemical modification, composites printing, and mechanical performance measurement of the printed composites were investigated. The effect of degree of functionalization on the mechanical performance of the printed composites is proposed for future study. This research topic will be elaborated in Chapter IV.

Third, a super-strong P(PA-co-AAm) copolymer that contains both soft (AAm) and hard (phenyl acrylate (PA)) components with different hydrophilic and hydrophobic properties will be studied. The single network P(PA-co-AAm) copolymer undergoes the simple one-step crosslinking process. PA is chosen to introduce the hydrophobic region in the copolymer chain to achieve high mechanical performance with the presence of hard phenol groups. Cellulose nanocrystals (CNCs) will be added to tune the viscosity of printable gels. The mechanical properties of the synthesized copolymer will be tested and analyzed under different PA, AAm, and crosslinker concentrations. A meniscus shape is also printed to demonstrate the feasibility of healthcare applications. The dimensional accuracy will be checked.

CHAPTER II

LITERATURE REVIEW

2.1 Background and present state of knowledge

3D printing was first described by Charles W. Hull in the year of 1986. He developed a system for generating 3D objects by creating a cross-sectional pattern of the object via UV light to cure thin layers of a UV curable material and named it 'stereolithography' [28]. Then, 3D printing has been widely studied for its advantages including geometric complexity, dimensional accuracy, customizable structures, automated and tool-less manufacturing processes, material cost-effectiveness, and many others [29]. The 3D printing of polymeric object can be described as follows: first, use the computer-assisted design (CAD) to create a virtual design of the printed object; then digitally sliced in the layer-by-layer fashion use the slicing software and generating g-code to control the print path (support structure may need for overhanging structures to prevent collapse during the build). Lastly, the build starts with the materials dispensing out of the orifice and dispenser moves in 3D spaces by steering the printer motors with movement. The concept of 3D printing process is demonstrated in Figure 2.1a. Comparing to traditional polymer processing techniques such as subtractive (Figure 2.1b) and formative manufacturing (Figure 2.1c) methods, 3D printing has more flexibility in complex geometries with more functionalities where the production rate and performance need further improvement.

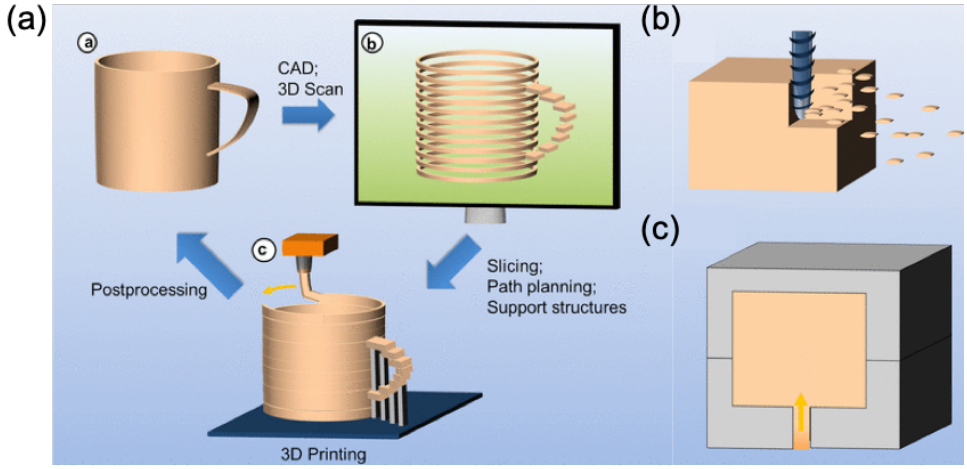

Figure 2.1 (a) additive process vs. (b) subtractive process vs. (c) formative technique, reprinted with permission from[30].

With rapid advances in 3D printing technology in recent years, many 3D printing modalities have been proposed and investigated to fit various applications. The 3D printing modalities can be categorized into different processes including material extrusion, material jetting, binder jetting, sheet lamination, vat polymerization, powder bed fusion, and direct energy deposition.

Among all of the 3D printing process listed above, one most commonly used and low-cost method is extrusion-based printing for polymeric materials. The material extrusion process has limited requirements for printing, thus, is suitable for a wide range of materials, especially polymeric ones. Besides, the equipment requirements are relatively simple and can be installed in any condition. Modifications on these printing modalities are easier compared to other processes such as SLS, SLM, binder jetting and etc. Based on the advantages of the extrusion-based printing process, it is selected as the printing process for the research conducted in this dissertation.

2.2 Material Extrusion

In the material extrusion process, materials are dispensed through a nozzle and deposited onto the platform. This is one of the most common categories for 3D printing technologies and has widely used in industrial applications.

2.2.1 Fused Filament Fabrication (FFF)

FFF modality is prevalent in 3D printing, and it is a low-cost modality suitable for printing thermoplastic materials, including polylactic acid (PLA)[31], acrylonitrile butadiene styrene (ABS)[32], acrylonitrile styrene acrylate (ASA)[33], Nylon[34] as well as many other composite materials with organic and inorganic fillers. In the FFF process, filaments are fed from a large spool via a moving, heated extruder printhead, and it is deposited on the platform or the growing work. The printhead moves under computer control to define the shape of printed constructs. The printhead moves in two dimensions to construct shape in the horizontal plane before it then moved vertically by a small distance to start a new layer. The working principle and printing process demonstration of the FFF process is shown in Figure 2.2a. From the fundamentals of the FFF process, this process is suitable for thermoplastics and thermoplastic-based material printing. But for other materials, their precursors are in liquid form and form irreversible polymer chains after crosslinking.

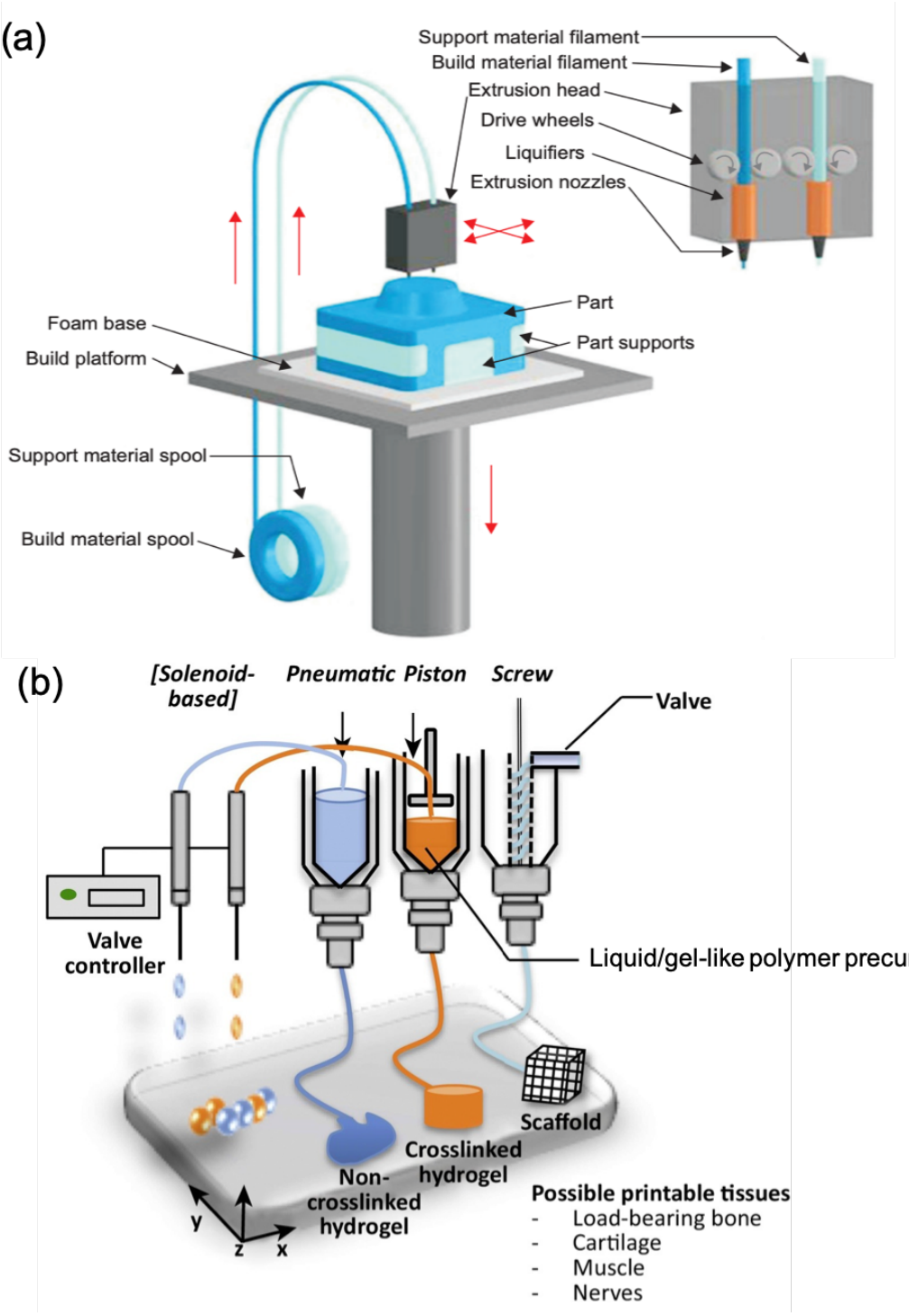

Figure 2.2 Scheme of material extrusion-based printing process. (a) FFF, reprinted with permission from [35]; (b) extrusion based 3D printing, reprinted with permission from [36, 37].

2.2.2 Direct ink writing (DIW)

The desktop direct ink writing modality was developed in 2000, inspired by the spatial position of adhesives lines dispensing out of the orifice. The extrusion-based printing process was first used in printing biomaterials, known as 3D dispensing.

Different from FFF, direct ink writing does not change the material phase during the extrusion process, and the extruded materials are solidified and formed the different shapes after deposited onto the platform. The extrusion is driven by different forces including pneumatic, piston, and screw-driven, as shown in Figure 2.2b.

For extrusion-based printing process, the extruder comprises a nozzle and a cartridge. The liquid/ gel-like materials sit in the cartridge before extrusion. The extruder head moves horizontally and vertically following the coordinates instruction in the g-code. The printed materials were then solidified via a variety of different solidification methods. These methods include: first is the physical processes like crystallization or glass transition of thermoplastics, dispersed polymer coagulation, solvent drying as well as precipitation of polymer solutions. Second is the chemical reaction such as the thermosets/ reactive monomers/ oligomers crosslinking networks formation and the ionomers and polyelectrolyte complexes formation. Thirdly, 3D print in liquid media for zero-gravity printing, viscosity changed reactive printing[30]. Among them, the chemical reaction is commonly used for reactive thermosets (including their composites) and hydrogel materials printing and will be discussed in sections 2.3 and 2.4, respectively.

2.3 Extrusion printing of thermosets and composites

High-performance and lightweight thermosetting polymers are known to be mechanically robust and capable of withstanding high service temperature for extended time periods that are more suitable for harsh environment applications compared to thermoplastic polymers. They are highly crosslinked polymer structures with irreversible chemical bonds. To date, thermosetting polymers have been widely used in various industries including aerospace[38, 39], coating[40], marine[41-43], automotive[44], and electrical[45] as a substitute for heavy-duty materials. The advances in lightweight, high-temperature resistance, and high-impact resistance led to the widespread application of thermosetting polymers in nowadays' aerospace, automotive, marine, energy, and coating industries. There have been a great number of thermosetting materials have been studied including epoxy resins[46-48], phenolic resins[49-52], cyanate esters[53, 54], benzoxazine[55-57], and bismaleimide[58, 59]. Their composites with mechanical-improved or thermal-resistant-improved properties are deemed as next-generation high-performance materials.

Many efforts have been devoted to 3D printing of thermosets, short fiber-reinforced composites, continuous carbon fiber composites and frontal curing of thermosets will be reviewed in this section.

2.3.1 Thermosets and short fiber composites

3D printing shows great flexibility in constructing objects with complex structures with the desired functionalities[60]. The low energy consumption, more efficiency, and easy operation make them more popular. Despite the popularity of 3D printing thermoplastics, only limited efforts have been devoted to print thermosets. This is due to the intrinsic

difference between thermoplastics and thermosets, which results in different process requirements[61]. Unlike thermoplastics, which have low melting points, thermosets undergo a phase transformation process where liquid monomers irreversibly cured while forming highly-crosslinked networks, and are hard to comply with conventional FFF process[62]. Thus, improvements and modifications of either material chemistry or the printing process are highly imperative to successfully adopt thermosets in the printing process.

To date, efforts have been devoted to designing different types of thermosetting polymers which are able to undergo solidification through gelation, solvent evaporation or on-the-fly photopolymerization process that are suitable for 3D printing[62]. Previous attempts regarding 3D printing thermosets can be classified into two categories: ex-situ and in-situ curing. The schematic illustration of the ex-situ and in-situ printing and curing process is shown in Figure 2.3 ab and Figure 2.4, respectively.

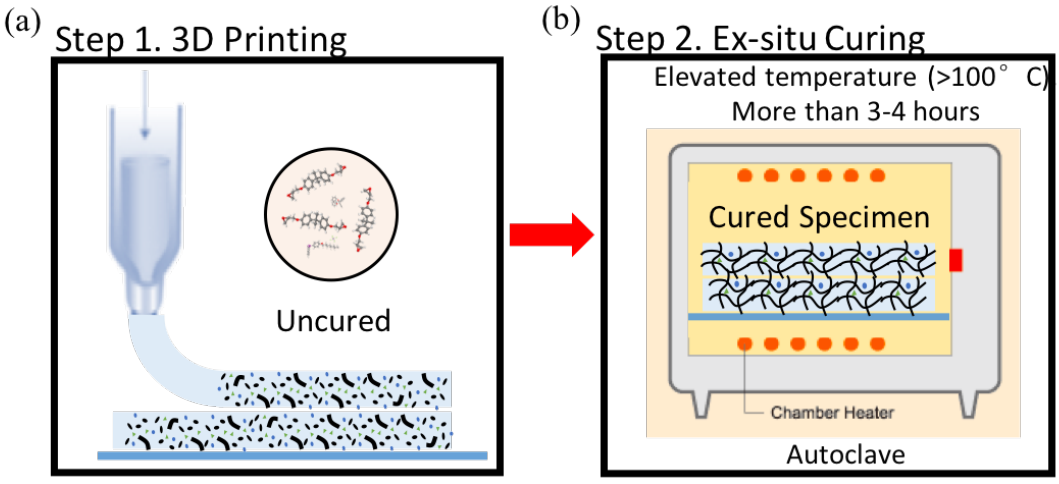

Figure 2.3 Schematic illustration of a current two-step process: printing and ex-situ curing.

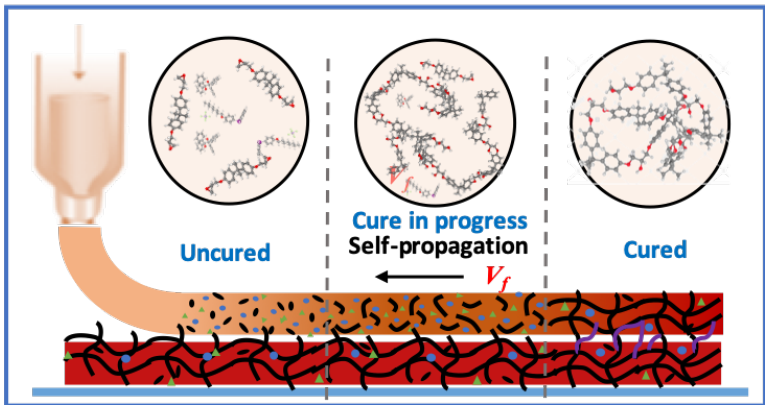

Figure 2.4 Schematic illustration of printing and in-situ curing process.

2.3.1.1 Ex-situ printing

The ex-situ process is based on the conventional curing method where various crosslinking processes have been explored including the thermally induced[38, 62, 63], photo-induced[64, 65], and the integration of both thermal and photo-induced crosslinking[66, 67]. The first attempt of 3D printing thermosets was reported by Lewis et al.[62] The epoxy-based ink filled with a high concentration of fibers was prepared for printing lightweight cellular composites. The printing process is demonstrated in Figure 2.5. The filled fibers with a high aspect ratio and tuned alignment embodied the essential rheological properties including sufficient viscosity, viscoelasticity, and shear-thinning behavior of epoxy-based inks. The constructs were not formed until post-curing at elevated temperature (100-220 °C). A similar concept of using silica fibers to enhance shear thinning behavior to meet rheological requirements for extrusion printing was reported by Lewicki et al.[63] Highly thermal resistant cyanate ester thermoset polymers with a high glass transition temperature (T_g) were printed. Unlike the prior ink design, a solid-liquid reversible ink enabled by strong hydrogen bonding was introduced to adjust the rheological behavior of the epoxy-

based ink[68]. The viscosity and viscoelasticity of the ink were decreased with the dissociation of hydrogen bonds induced by shear force along with the printing head. This was accompanying by a phase transition from a low-viscosity liquid to a self-supportive solid.

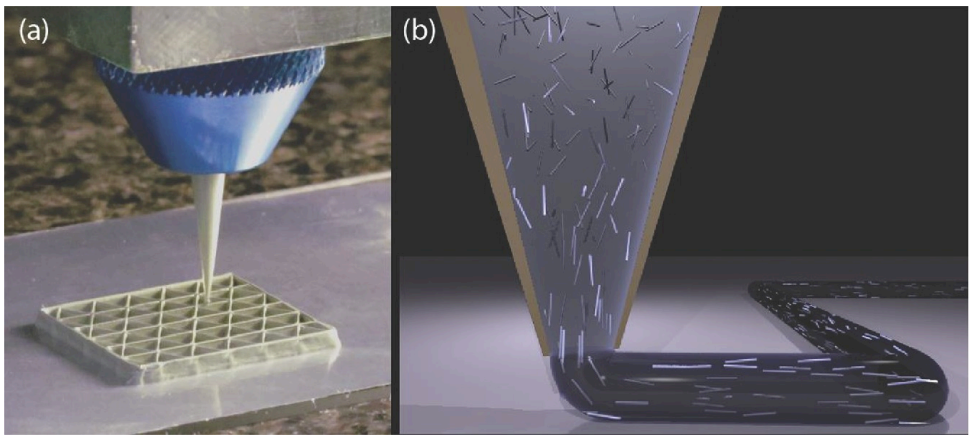

Figure 2.5 (a) Optical image of 3D printing of a triangular honeycomb composite. (b) Schematic illustration of the progressive alignment of high aspect ratio fillers within the nozzle during composite ink deposition, reprinted with permission from [62].

2.3.1.2 In-situ printing

Though extrusion-based printing is a more common way to construct thermosetting polymers, other methods such as stereolithography (SLA) and digital light processing (DLP) were also explored for thermosetting polymers. Specifically, the polymer structure formed directly after printing without post-curing process with in-situ light initiation for crosslinking reaction. These methods provide alternative ways to process polymers with melting challenges. One straightforward way was preparing light-responsive thermosets resin for these light assisted curing process. Long et al. printed all-aromatic pyromellitic dianhydride and 4,4′-oxydianiline (PMDA–ODA) polyimide

(Kapton) with the addition of UV initiator via mask projection SLA[65]. Though the feasibility of SLA based polyimide printing was demonstrated, the constructed parts exhibited a deteriorated tensile strength (~80 MPa), only half of the tensile strength compared to the commercial Kapton (~ 165 MPa) parts[65]. Later, Qi et al. fabricated high-performance epoxy via a two-stage curing process, which involves both ex-situ and in-situ curing process[66]. Their ink contains both photocurable resin and thermally curable resins. The ink first undergoes DLP and formed its initial structure before thermally cured at elevated temperature. Thermal curing was introduced to obtain the interpenetrating polymer network of epoxy so the mechanical performance can be improved. But the dual process is complicated and takes a longer time to fabricate a piece. Another facile method to improve the printed structure performance was introducing dynamic covalent bonds[67]. Qi et al. first used the dynamic covalent bonds to print recyclable vitrimer epoxy, followed by Ge et al[63, 67]. Generally, the modified epoxy resin with hydroxyl and ester functional groups were prepared, followed by a transesterification reaction at elevated temperatures. The dynamic covalent bonds also enable the printed thermosets to be reshaped, repaired, and recycled. Similarly, Smaldone et al. used the reversible bonds of furan and maleimide to fabricate recyclable thermosets with improved mechanical performance[69].

Besides, the light-induced process to achieve in-situ curing, more recently, frontal polymerization was introduced for in-situ thermosets print-and-cure in an extrusion-based printing process. White et. al demonstrated the process based on a frontal ring-opening metathesis polymerization (FROMP) of dicyclopentadiene (DCPD) with sufficient exothermal energy to sustain the front[38]. The process was highly energy-efficient which

saved tons of energy needed in the post-curing process. The proposed FROMP process is demonstrated in Figure 2.6a and the printed constructs are shown in Figure 2.6b, c. However, the proposed frontal polymerization is only limited to one typical thermosetting material due to its high reactivity. Compared to the popular epoxy resin and other high-performance resins, the application of DCPD is limited. However, there still lacks a general in-situ print-and-cure method that is suitable for a variety of thermosetting materials. Its development requires improvements in today's manufacturing process, a deeper insight into chemical reactions in relation to the material process and performance[70]. The integration of polymer chemistry and the state of art 3D printing process paves the way for high-performance thermosets and composites with enhanced processability, performance, and durability[62, 63, 71, 72].

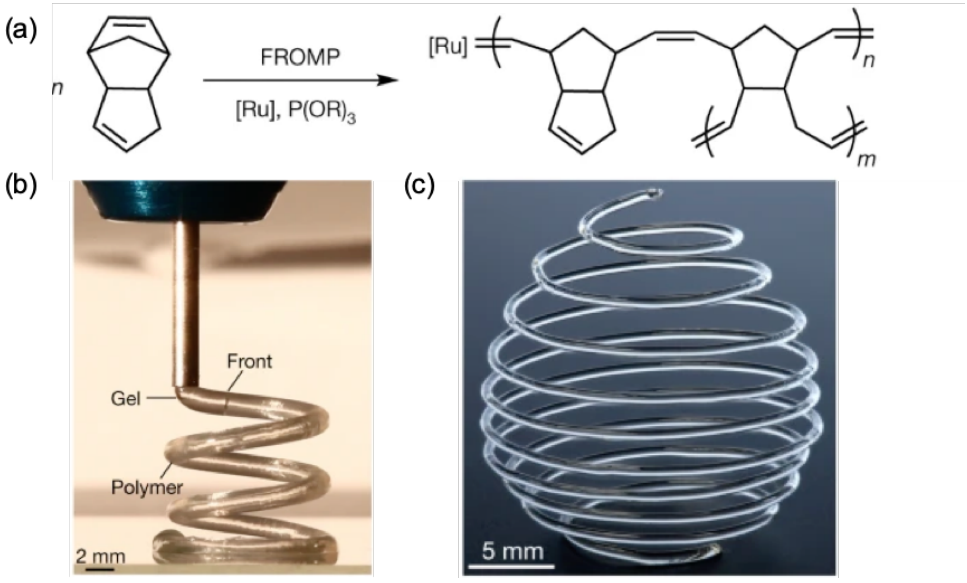

Figure 2.6 Frontal ring-opening metathesis polymerization (FROMP). (a) Scheme for the FROMP of DCPD using a ruthenium catalyst; (b) 3D printing of gel DCPD solution that is solidified by FROMP immediately following extrusion from the print head; (c) Free-form 3D-printed structures produced via FROMP, reprinted with permission from [38].

2.3.2 Interlayer adhesion of 3D printed parts

3D printing is an efficient way of constructing complex structures in a layer by layer fashion[73]. Construct quality is closely related to the effectiveness of the manufacturing process. For high-performance thermosetting polymers, the mechanical property is one critical criterion in the field of aerospace, marine and etc. Unlike the traditional molding process in which integral parts with covalent bonds were formed, in many cases, there only exist physical contacts without interlayer bonding between every two adjacent layers in 3D printed parts[65]. Especially, for the light-assisted printing process, the limited penetration depth of the light source further damages the overall integrity and leads to a less mechanical strong part.

Previous attempts have been focused on introducing the second crosslinking network after the initial printing process[66, 67, 69]. Qi et al. prepared the ink with both thermal and photo initiators to form two interpenetrating polymer networks[66]. The photocurable resins composed of ethoxylated trimethylolpropane triacrylate with additional glycidyl methacrylate diluent were cured in a DLP process to form the first network with a designed structure. Then the part underwent a thermal curing process forming the second network. The printed interpenetrating network exhibited significant enhancement (~90 MPa) in fracture stress compared to neat epoxy (~50MPa)[66].

Except for the two-step crosslinking, other methods incorporated modified epoxy monomers with dynamic covalent bonds[67, 69, 72]. After the monomers were solidified, transesterification occurs at an elevated temperature between adjacent hydroxyl and ester

groups. After the bonding transformation, the crosslinking network reorganized and formed covalent bonds between originally printed layers. Other researchers also reported improved mechanical performance by introducing dynamic covalent bonds in the monomers[69]. In addition, the reversible thermosetting materials obtained a smoother surface compared to the conventional thermosets[69].

Fiber-reinforced composites were also claimed to have higher interfacial bonding strength due to fiber-polymer interaction[74]. Decorated functional fibers with reactive chemical groups would yield the enhanced performance accredited to the covalent bonding formed between two extruded fibers and surrounding resins[75].

The aforementioned 3D print-and-cure poly (DCPD) also yields a high mechanical performance, not as high as over cured poly (DCPD), but only exhibited ~5% reduction regarding the printed parts[38]. This may be due to the integrated process of printing and curing, curing of the upper layer produce the second chance for the uncured resins left in the bottom layer.

Previous attempts over the improvement of printed interlayers involve additives and may complicate the printing process and change other characteristics of the thermosetting materials. Among all, frontal polymerization exhibited the potential in strengthened interlayer interactions. However, previous research did not mention the interlayer interaction in relation to the frontal polymerization process.

2.3.3 Frontal curing of thermosets

Frontal curing was first discovered by Chechilo inspired by self-propagating high-temperature synthesis in 1972[76]. It is an autocatalytic polymer reaction that instantaneously transforms monomers to linear or crosslinked polymers, which is notably different from the frontal curing of linear polymers proposed in this research. The scheme of a photo-induced thermal frontal polymerization process is shown in Figure 2.7. The polymerization starts with an initial energy trigger, and the reaction propagates along the vessel. The essential of frontal polymerization is an exothermal reaction where the released energy further initiator the adjacent monomer polymerization[77]. Thus, frontal polymerization needs an external energy source to initiate the process and exothermic energy exceeds activation energy even at room temperature to sustain the reaction. With the depletion of reactive monomers or initiators, the propagation stops. Frontal polymerization has been applied to synthesis hydrogels[78], thermoplastics[79, 80] as well as thermosets[81]. According to the initiation process, frontal polymerization has been categorized into three types: thermal-induced, photo-induced, and isothermal-based frontal polymerization. The former two methods dominate the fabrication of thermosetting polymers.

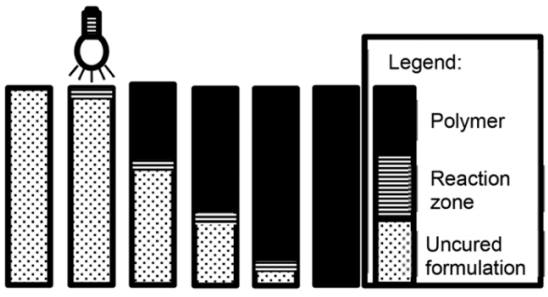

Figure 2.7 Scheme of a photo-initiated thermal frontal polymerization, reprinted with permission from [81].

Thermal-induced frontal polymerization uses a thermal energy source to initiate the reaction. One typical example is frontal ring-opening metathesis polymerization of DCPD with the presence of highly efficient ruthenium Grubbs'-type II (GC2) catalyst[82]. By tuning the molar ratio of Exo-DCPD monomer and GC2 catalyst to 15,000:1, the frontal velocity can reach its summit of 8 cm/min[83]. This reaction is rapid and energy efficient. However, the principal drawback of the frontal polymerization chemistry lies in the limited system pot life. The pot life of DCPD, first-generation GC catalyst and triphenylphosphine inhibitor system was only about 60 seconds at room temperature, reported by Mariani et al[84]. To increase the pot life, the solution was frozen before use. Later, a more efficient inhibitor, 4-dimethylaminopyridine (DMAP), successfully extended the pot life up to 30 minutes at room temperature[85]. More recently, Moore et al. increased the pot life by ~140 times with the efficient alkyl phosphites serving as an inhibitor added to DCPD, GC2 system. Though the addition of alkyl phosphites deteriorated the reactivity of the polymerization, there is a balance between pot life and frontal velocity. When tuning the tributyl phosphite/ catalyst molar ratio to 1:1, the pot life extended to 5 hours, while frontal velocity still high enough (~6 cm/min) for fast and energy-efficient reaction[86]. The extended pot life enables in-situ print-and-cure of poly(DCPD) where DCPD monomers were extruded and transformed to a fully cured structure with precisely controlled reaction kinetics. This invention was a breakthrough that facilitates the manufacturing of thermosetting polymers and composites in a more rapid and energy-efficient way. Though neat poly (DCPD) exhibited comparable mechanical performance of epoxy, the glass transition temperature T_g and thermal

resistance limited its application in the aerospace industry. Thus, the generalization of this 3D in-situ print-and-cure method to other thermosets is highly imperative. The principal challenge lies in the high molar enthalpy of the reaction process and rapid reaction rate to minimize energy loss to the environment and prevent quenching of the exothermic wave.

Previous attempts of curing epoxy using frontal polymerization were reported in the year 1997[77]. The commercially available diglycidyl ether of bisphenol F (DGEBF) epoxy (EPON 862) was frontally cured with the addition of aliphatic amine (Epicure 3371) in a stoichiometric ratio. The velocity of the front was measured with a different amount of amine addition. Though higher frontal velocity was observed with the increasing amount of amine added, the highest frontal velocity was only ~8 mm/min, which is 10 times lower than DCPD, GC2 frontal polymerization system. The frontal velocity is too slow to sustain in an ambient condition when comes to the 3D printing system. Moreover, the obtained cured epoxy exhibited better mechanical performance with a stoichiometric amount of amine addition. Thus, the pure thermal-induced frontal polymerization may not provide sufficient exothermic energy for epoxy-based thermosets. To achieve 3D in-situ print-and-cure, an alternative method is needed to compensate for the non-efficient thermal curing.

Liska et al showed the feasibility of radical-induced cationic frontal polymerization in energy-efficient bulk curing of epoxy[81]. The idea is to introduce a photoinitiator along with the carbon-carbon labile compound based thermal radical initiator to lower the threshold of generating a self-sustaining front. The initiation process was triggered by UV irradiation or local heat accompanied by the generation of Lewis-

acid for further polymerization[87]. Differ from DCPD, which has limited pot life and low activation energy with the addition of highly efficient GC2 catalyst, epoxy resins are relatively inert with higher activation energy and uneasy to cure at room temperature. Thus, the epoxy system can be stored at room temperature for an extended time, even more than a week. The most efficient pair of thermal radical initiator and cationic photoinitiator was 1,1,2,2-Tetraphenyl-1,2- ethandiol (TPED) and p(octyloxyphenyl)phenyliodonium hexafluoroantimonate (IOC-8 SbF_6), respectively. Except for DGEBF, additional epoxy resins such as glycidylethers neopentanediol diglycidylether (NPDGE), hexanediol diglycidylether (HDDGE) and cyclohexanedimethanol (CHDGE) were also studied. The proposed mechanism of the initiating system is shown in Figure 2.8. The frontal velocity was achieved its summit of 37.9 cm/min for CHDGE resins with addition of 1 wt% thermal and photoinitiator, respectively. Similarly, Mariani et al. explored the cationic frontal polymerization in cyclohexyl epoxy ester (CE) while using the iodonium salt (HOPH SbF_6) as photo-initiator and dibenzoyl peroxide (BPO) as thermal initiators. It has been proved that both initiators are critical for a successful and complete curing[88]. The capability of the photo-, thermal dual initiators in epoxy and polyurethane hybrids systems was later proved by Hu et al[79]. Despite the neat resins, UV-activated cationic frontal polymerization was applied in glass fiber reinforced epoxy composites by Liska et al[89]. Though glass fiber is not a highly thermal conductive fiber, its presence does not influence the frontal curing. The frontal cured epoxy composites exhibited a comparable tensile strength and tensile modulus of conventional thermal curing method.

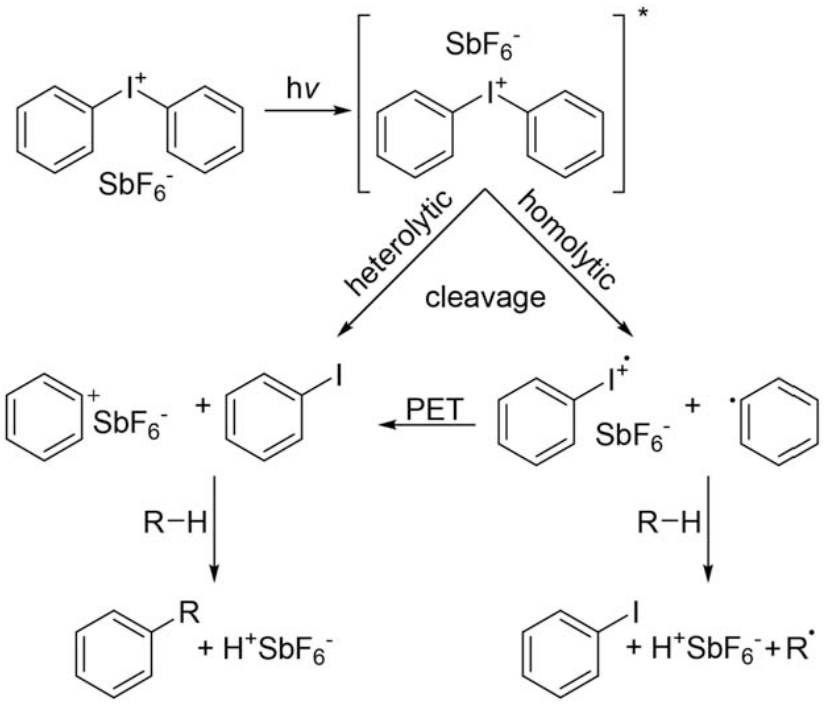

Figure 2.8 Possible photoinduced electron transfer (PET) from the radical-cation, reprinted with permission from[90].

Previous attempts demonstrated the potential of frontal polymerization in thermoset fabrication. It is easy to achieve in-situ print-and-cure of highly reactive thermosetting materials such as DCPD via frontal polymerization. But for low reactivity thermosets, the conventional thermal-induced process does not provide sufficient energy for rapid front propagation.

2.3.4 Continuous carbon fiber composites

3D printing of continuous carbon fiber composites holds the promise as the next-generation composite manufacturing technique for their design flexibility and automation, which gained the spotlight in recent studies. Unlike discontinuous carbon fiber that can be easily adapted to many 3D printing technologies including fused filament deposition, liquid deposition modeling, vat polymerization, selective laser sintering, and etc., existing

3D printing technology for continuous carbon fiber fabrication is limited to fused filament deposition and vat polymerization. For fused filament deposition, small modifications on the print head are needed to pull out the continuous fiber and the epoxy resin. A variety of thermoplastic-based carbon fiber reinforced composites were studied, including acrylonitrile butadiene styrene (ABS)[91, 92], polylactic acid (PLA)[93, 94], and etc. The printing process is illustrated in Figure 2.9a. Among those previous endeavors, the highest ultimate tensile strength is reported by Tian et al. The PLA filament was fused and coated onto the carbon fiber before extrusion. Their PLA-carbon fiber (recycled, 8.9 vol%) reached about 260 MPa, comparably lower than current thermosets reinforced carbon fiber composites (~1GPa)[94, 95]. Hao et al. developed epoxy reinforced carbon fiber printing and achieved a mechanical strength of 792 MPa[96]. The printing process is demonstrated in Figure 2.9b. The mechanical performance was greatly improved compared to thermoplastic ones, but still not comparable to the conventional manufacturing process. The limitation of this technology lies in the layering effect in the printed composites which resulted in the inferior mechanical performance of the printed part[95]. Besides, the thermosets reinforced carbon fiber process requires a post-curing process which increases the manufacturing time and raises the energy intensity of the composite's fabrication. Thus, researchers are seeking for low-cost, energy-efficient, rapid, and automated fabrication process with high design flexibility.

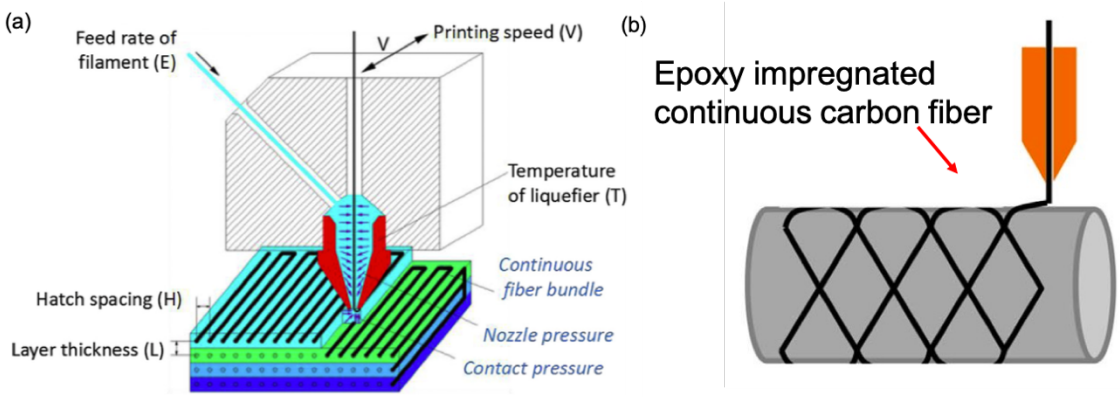

Figure 2.9 (a) thermoplastic polymer based continuous carbon fiber composites printing, reprinted with permission from [92]; (b) thermosetting polymer (epoxy) based continuous carbon fiber composites printing, reprinted with permission from [96].

More recently, Shi et al. reported a process in-situ printing of continuous carbon fiber composites via a dynamic capillary-driven AM approach, called localized in-plane thermal assisted (LITA) 3D printing, as shown in Figure 2.10.

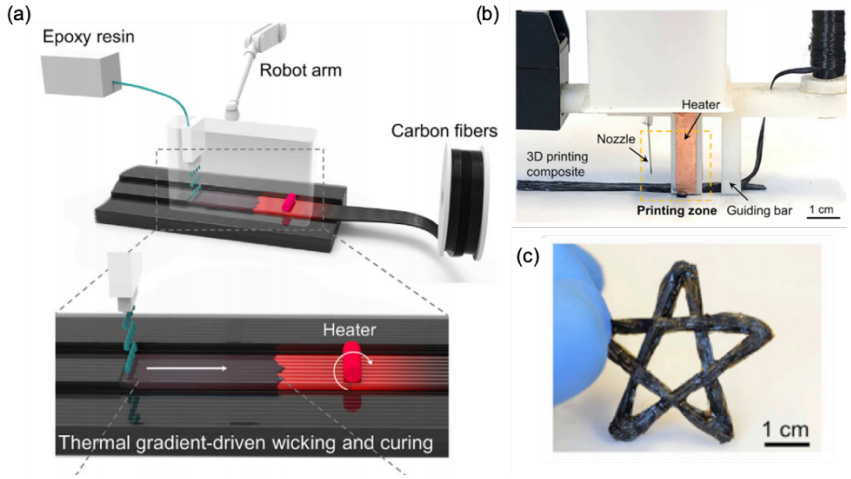

Figure 2.10 (a) Schematic of LITA 3D-printing approach based on dynamic capillary-driven infusion and curing of thermosetting polymer; (b) LITA 3D-printing system; (c) examples of 3D-printed composites: a star, reprinted with permission from [97].

Frontal curing bulk fabrication of continuous carbon fiber composites was proposed and demonstrated by Tran et al in 2020[98]. The process showed great promise of epoxy-based continuous carbon fiber composites fabrication since the tensile performance

achieved here was comparable to conventional ones. The formation of composites highly relied on the epoxy formation and the mechanism is similar to pure epoxy resin-based frontal curing, as shown in Figure 2.11.

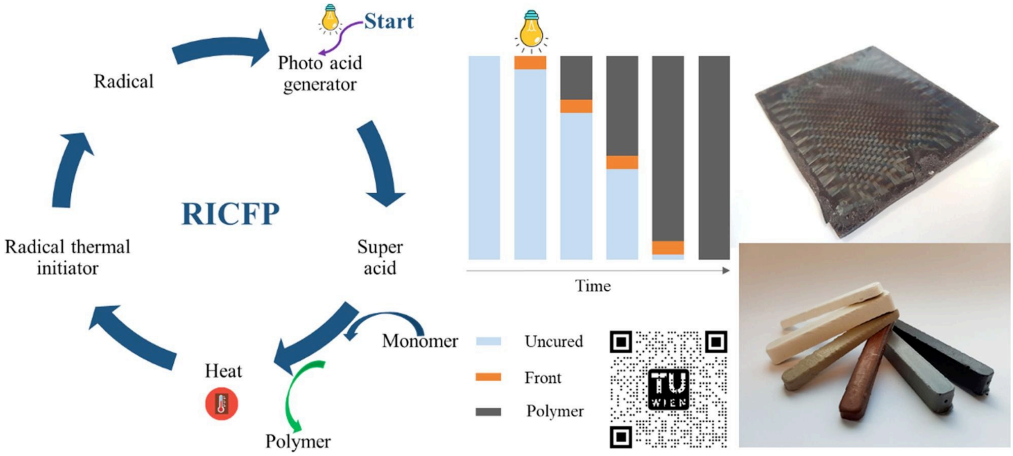

Figure 2.11 bulk fabrication of continuous carbon fiber composites via frontal curing, reprinted with permission from [98].

2.4 Extrusion based printing of hydrogels*

Parts of this chapter/section are reprinted with permission from [99]

Hydrogels consisting of crosslinked macromolecules and water is a class of biomaterials prevalent in today's load-bearing tissue fabrication[100, 101]. To date, four types of hydrogels have been fabricated via mold processing, including nanocomposites (NC) gel[15-17], ionic-covalent entanglement (ICE) gel[23, 24], slide-ring (SR) gel[21, 22], and double network (DN) gel[18-20]. Among them, DN gels attracted extensive attention for their excellent mechanical performance. The exceptional properties observed on DN gels were attributed to the synergistic effect of interpenetrated hard and soft polymer networks via an energy dissipation mechanism. The most attractive DN gels are poly(2-acrylamido,2-

methyl,1-propanesulfonic acid) (PAMPS)/PAAm, alginate/PAAm[20], agar/PAAm[18], etc., which demonstrated mechanical performance superior to their components. Especially, the PAMPS/PAAm DN gel fabricated by molding process demonstrated tensile strength ranging from 1 to 10 MPa, a compressive strength of 20-60 MPa, and toughness of 10^3-10^4 kJ m^{-3}, which are superior to other types of hydrogels and comparable to the natural meniscus[19, 25]. The formation process (chemical crosslinking formation and interpenetration of different polymer networks) was shown in Figure 2.12. Such exceptional properties were accredited to a primary rigid and brittle network interoperated with a secondary soft and ductile network and well-controlled crosslinking density (tightly crosslinked first network and loosely crosslinked second network)[27].

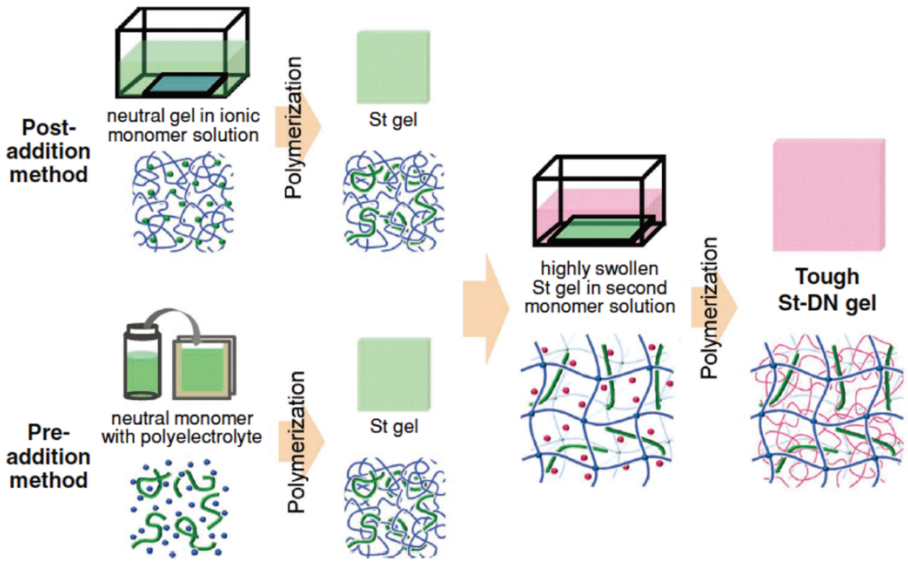

Figure 2.12 Formation of tough DN hydrogel, reprinted with permission from [102].

2.4.1 Significance of printing hydrogels

Challenges of engineering an artificial meniscus include mimicking the complex structure of meniscus with individualized features and superior mechanical performance

required to mimic the natural meniscus (e.g., high compressive strength, tensile strength, toughness, shock absorption, and low friction).

Although molded hydrogels could achieve high mechanical properties, the molding process is difficult to produce the precise geometry features of the meniscus. Lack of geometry precision will lead to mismatch and many transplantation problems of the meniscus. Emerging 3D printing technology can construct the freeform structure by the addition of successive layers of materials which offer high geometric fidelity, structure complexity, and design flexibility. Therefore, it allows patient-specific tissue fabriaction[99, 103]. Among them, the mechanical performance of 3D printed artificial meniscus highly depends on the material properties[104]. Seeking suitable materials to achieve the mechanical performance of natural meniscus is a real challenge. Though endeavors of synthesizing different hydrogels by varying proportions of ingredients were reported, the resultant mechanical performance is still far inferior to the natural tissues and not able to meet the demand[104]. Another concern is the biological response to the selected material, which in turn directed the biocompatibility. The understanding of biocompatibility is critical in determining tissue longevity and functionality. The most and fundamental step is developing printable material and the materials preserve the required mechanical performance for load-bearing tissue applications.

2.4.2 Progress of hydrogel printing

2.4.2.1 Macro-scale printing

Many attempts have been devoted to preparing printable inks with suitable viscosity, viscoelasticity, and instant sol-gel transition for printing[105, 28, 29]. Yang et al.

reported a suitable printing viscosity ranging from 10^3 to 10^4 Pa s to store the ink in the cartridge and avoid high extrusion pressure[26]. To achieve instant sol-gel transition, both ion responsive and temperature responsive[23] polymer were incorporated. Besides, the introduction of high aspect ratio nanostructures (nanosilicates) induced shear thinning behavior and formed secondary electrostatic crosslinking with charged polymer chains to improve the viscoelastic properties[18]. Chimene et al. incorporated gelatin methacryloyl (GelMA) and nanosilicates to functionalize their bioinks with temperature-responsive sol-gel transition and improved shear thinning and viscoelasticity[23]. Recently, the PAMPS/PAAm DN hydrogel was printed via a two-step method where the second PAAm network was formed after the first PAMPS network was printed and crosslinked[26], as shown in Figure 2.13a. The resulting DN gel showed a tensile strength of 1.4 MPa[26]. The printed meniscus is placed in the artificial knee joint as a cushion for demonstration, as shown in Figure 2.13b. Later, Li et al. reported a dual ionic crosslinking method for printing alginate/poly(acrylamide-co-acrylic acid)/Fe^{3+} DN gel. The printed DN gel exhibited higher strength of 3.24 MPa[106]. However, the mechanical performance of 3D printed hydrogel is still inferior to the molding-processed hydrogel, and not able to meet the transplantation demand.

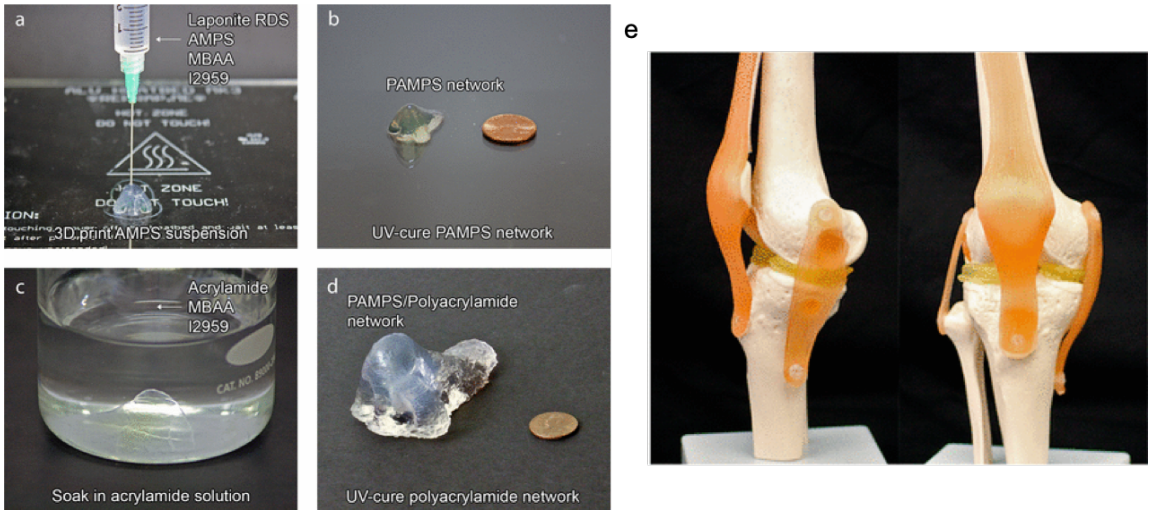

Figure 2.13 Steps for 3D printing a DN hydrogel: (a) 3D print the AMPS suspension; (b) UV-cure to obtain the PAMPS network; (c) soak the PAMPS network in an acrylamide solution; and (d) UV-cure to obtain a PAMPS/polyacrylamide double network; (e) printed meniscus is placed in the artificial knee joint as a cushion, reprinted with permission from [26].

2.4.2.2 Micro extrusion-based printing (MEB)

The MEB technique is the integration of two processes: extrusion and bioprinting. They are controlled by a fluid-dispensing system and 3D spatial automatic movement controlling system [107]. MEB is one of the most commonly studied methods in 3D bioprinting [36, 107, 108]. It is the most cost-effective printing method among the three above mentioned printing techniques. The working principle of the extrusion printing system is that it dispenses the ink using either pneumatic [109] or mechanical (includes piston or screw) dispensers [110, 111]. Some examples will be introduced in the following sections, as shown in Figure 2.14.

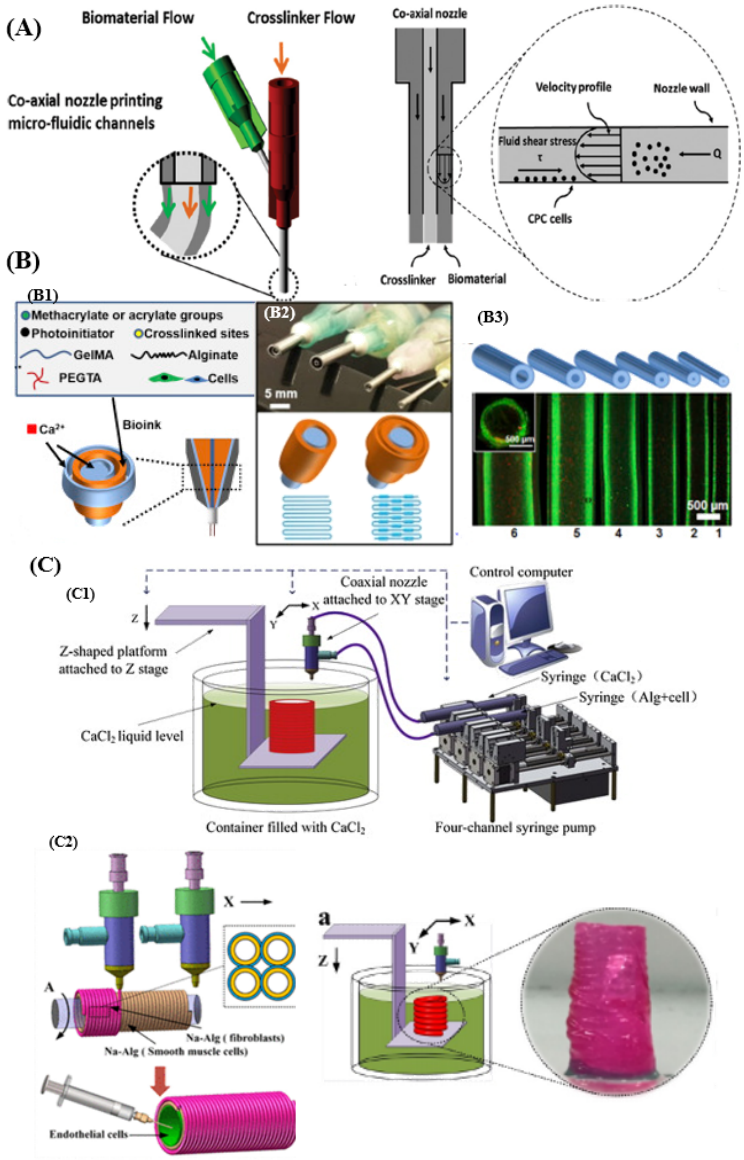

Figure 2.14 Coaxial 3D Bioprinting for MEB (a) Coaxial nozzle assembly and associated mechanical forces demonstration, reprinted with permission from [112]; (b) Direct 3D printing perfusable vascular structure, reprinted with permission from [113] (b1) Biomaterial composition and coaxial nozzle demonstration; (b2) The designed multilayered coaxial nozzles and schematic diagram showing fabrication of perfusable hollow tubes with constant diameters and changeable sizes; (b3) Schematic diagram and representative fluorescence micrographs showing the bioprinted perfusable tubes displaying different outer diameters; (c) 3D bioprinting three-layered vascular structure, reprinted with permission from [114] (c1) Fabrication process of 3D alginate vessel-like structures with multiscale fluidic channels; (c2) Vertically printed vascular structure and horizontally printed vascular structure with inner and outer hollow structure.

The suitable printing material viscosity for MEB ranges from 30 mPa/s to more than 6×10^7 mPa/s[115]. The materials which meet this requirement include biocompatible hydrogels, copolymer as well as spheroids (a type of cell aggregates)[116]. Materials with higher viscosity are easier to form structure but come with lower cell viability. Studies reported that the cell survival rates range from 40% to 97% depending on the material and the dispensing system [116]. Some studies used the two-step crosslinking method of the hydrogel to improve cell viability. Specifically, they prepared the partially polymerized alginate-based hydrogel[117]. In MEB, the materials used are non-Newtonian and can be thermally crosslinked. For non-Newtonian material, the increase of shear rate will cause the decrease in viscosity[118], due to pseudo-plastic or shear thinning effect. Shear thinning enables the formation of the desired structure by the material when it endures a high shear rate at the nozzle head, where the viscosity of the material increase and form the structure after flowing out the nozzle upon deposition[116].

Increasing printing resolution is a challenge to all printing methods. The current MEB technique enables to print 5 μm to millimeters wide resolution at low printing speed (5-10 μm /s), referred to Table 2.1. But the real tissues require even nanoscale printing resolution [119] which is still a technology gap for researchers to overcome. Cell viability of MEB can be lower than other printing methods, possibly due to the shear stresses applied to the biomaterials while extruding them out from the nozzle. Higher viability can be achieved at the cost of resolution.

Aortic valves, vascular, branched vascular trees have been fabricated using MEB [116]. Adaptation has been made to both the nozzle and printing process which to be more

compatible to complex structure formation. Yu et al. designed a pressure-assisted freeform fabrication process using coaxial nozzles where two different fluids flow through the tubes, and then meet and trigger the gelation process to print hollow filaments[112]. Later, the printing principle and the mechanics' models were established by the same group[120]. They also developed a multi-arm bioprinter that can print multiple materials concurrently with independent motion path and dispensing parameters[121]. Gao et al.[122] modified the printing process by the motorized XY stages and with the coaxial nozzle attached to form hollow filament in a precise location. A Z-shaped platform moves up and down to print vertical layers. Recently, Gao's group designed a new fabrication method using the rolling process [114]. Besides, Jia et al. published a method where nozzle size can be tuned to satisfy multiple dimension requirements[113].

Though MEB is not the first printing technique used in bioprinting, it is the most widely studied one [107] for its advantages including the ability to deposit high cell densities, relatively precise spatial control of the desired constructs. The flexibility of nozzle size and shape design also facilitates the improvement of MEB in vascular tissue construction. For example, one possible way to form hollow structure and branching structures toward vascular structures is adapting the coaxial nozzles and introducing the rolling process.

Table 2.1 List of parameters of printing process and ink requirements for hydrogel printing

	Extrusion based printing	Reference
direct/indirect	Both direct and indirect	108
Scaffold/Non-scaffold based	Scaffold-based and scaffold-free	36
printing resolution (um)	200	123
Printing Homogeneity	Uniform	36

Table 2.1 Continued

3D Bioprinting Capability	High	[123]
Degree of Research	High	[124]
Printing Cost	Low	[123]
Print Speed	Slow (10-50 mm/s)	[124]
Cell Density	High (>10^6 cells/ml), Cell-only Bioink	[124]
Types of Materials for Bioink	Cell-free, Cell-laden Cell-only Bioink	[108]
Vertical mechanical structure quality	High	[125-128]
bioink viscosity (mPa/s)	High (30 - >6*10^7)	[124]
Advantages	High cell density, Spatial control, Support scaffold-free printing	[36, 107, 108, 120, 123, 124, 129-135]
Disadvantages	Moderate speed, Clogging issue (at 150um)	

2.4.3 Technical requirements for extrusion-based hydrogel printing

2.4.3.1 Rheological performance

Rheology is the study of the flow of matter under application of an external force and is, therefore, is one of the major physiochemical parameters that determine the printability of a hydrogel [129]. Investigation of rheological property and its relationship with the results of the deposition processes are necessary to bio-fabrication study. However, a large number of investigations do not take it into account. Herein, several rheological parameters including viscosity, shear thinning as well as yield stress are concluded in this literature review.

2.4.3.1.1 Viscosity

Viscosity is the resistance of a fluid to flow upon the application of stress. In 3D printing process, high viscosity hydrogel impedes extrusion or injection of the material out of the nozzle and the collapse of deposited structures. The viscosity also affects the cell proliferation and tissue formation after the constructs have been printed out. The viscosity of the hydrogel precursor can be tuned via molecular weight and polymer concentration. But, the viscosity required for different printing processes varies[136]. For meniscus printing, tough hydrogels are needed. Efforts are made to improve the strength of printed hydrogel constructs[26, 137, 138]. Double network hydrogels are developed for achieving extremely tough constructs that can endure the stress between two bones as a synthetic meniscus. Viscosity is optimized for printing with the addition of a rheology modifier. Yang et al. [26] has found out that, for their hydrogel printing system, 14.48−37.72 kPa·s is sufficient to enable an object to retain its shape after extrusion without the frequent clogging of the nozzle. In some work, simulations have been done to evaluate the shear rates that would be experienced during printing at deposition temperatures to more accurately characterize the rheology of inks [139]. The majority study of the rheological property has focused on solution viscosity[140]; however, since these inks are gels, other types of analyses are necessary[141].

2.4.3.1.2 Shear Thinning

Shear thinning refers to the Non-Newtonian fluid behavior where the viscosity decreases while the shear rate increases. Shear thinning behavior is often observed in high molecular weight polymer solutions. Sodium alginate is an example that shows shear

thinning behavior[142] were with an increased shear rate but decreased shear stress inside a printing nozzle; when the hydrogel ink comes out of the nozzle, a sharp increase in viscosity is observed to ensure high printing fidelity[26].

2.4.3.2.3 Yield Stress

Yield stress is the minimum stress to initiate flow. The addition of yield stress can prevent the flow of collapse of a deposited structure[143]. In comparison, high viscosity only delays the collapse[136]. However, the study of printed hydrogel yield stress is limited.

The aforementioned information is listed in Table 2.2.

Table 2.2 Hydrogels applied for fabricating 3D-structures and their rheological property study

Hydrogel composition	Fabrication technique	Rheology study	reference
Alginate		Rational analysis: Power law index is calculated, n<1 indicates shear thinning property; Oscillatory analysis	[142]
modified hyaluronic acid (HA)	Material extrusion	Shear thinning	[144]
Silk gelatin/silk gelatin glycerol	Material extrusion	Viscoelasticity behavior of inks, flow behavior including shear stress, shear rate, shear viscosity and shear thinning behavior.	[139]
Acrylamide and N,N,N′,N-tetramethylethylenediamine (TEMED)	Material extrusion	Viscosity, Yield stress, Shear thinning, viscoelastic moduli	[145]
Alginate/Agar	Material extrusion	Viscosity	[137]

Table 2.2 Continued

Sodium 2-acrylamido-2-methylpropanesulfonate/ acrylamide	Material extrusion	Shear thinning, viscosity	[26]
alginate/acrylamide gel precursor solution and an epoxy adhesive	Material extrusion	Viscosity, shear thinning	[138]

2.4.3.2 Solidification process

The liquid-form or gel-like hydrogel precursors without any crosslinking formation were loaded into the cartridge for extrusion, and phase transformation to solids is needed to maintain the shape of the printed constructs. Thus, the solidification process would be important in the extrusion-based process for hydrogel printing. Two commonly used methods for the solidification of hydrogels are print into the liquid and chemical reaction.

2.4.3.2.1 Print into the liquid

This solidification process does not need to build support structures and postprocessing. When the extruded material flows into the liquid, the extruded filament strand is either constrained by the buoyancy force according to the Archimedes principle or form new chemical bonds in the polymer network to maintain its shape and prevent structural collapse, as shown in Figure 2.15a. This print into the liquid method is suitable for 3D printing of hydrogels, which is tend to collapse after extrusion[146]. One requirement for the Archimedes principle-based method (also named zero-gravity process) is the matching densities of printed materials and liquid media[30]. Another one is to add the

initiators, coagulation agents, or activators in the liquid media and induce the chemical reaction when the material contacts with the liquid media[30]. One example is the crosslinking of alginate using calcium ions in the liquid media, as shown in Figure 13b.

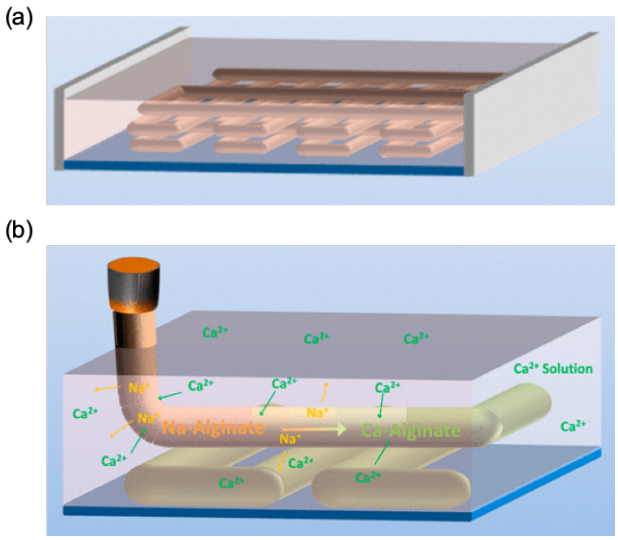

Figure 2.15 Solidification process. (a) print into the liquid; (b) chemical reaction, reprinted with permission from [30].

2.4.3.2.1 Chemical reaction

The common, straightforward, and simple way of hydrogel printing is to formulate highly viscous precursors and cured the via a chemical reaction. The high viscosity and proper viscoelasticity are achieved by loading of high aspect ratio nanofiller/ microfiller materials. The chemical bonds are formed via thermal or light energy input with the presence of initiators and crosslinkers in the ink formulations. The chemical reaction could happen during the printing process and after the part is fully printed. For an in-situ chemical reaction, it gives a larger range of materials rheological properties, but the

crosslinking rate must match with the print speed to ensure the polymer inter-diffusion and minimize the polymer network defects[30]. Wang et al. used the ex-situ curing to print the hydrogel, as shown in Figure 2.15b. The hydrogel was crosslinked via ultraviolet light.

CHAPTER III

FRONTAL CURING ASSISTED ENEERGY-EFFICIENT 3D PRINTING OF EPOXY AND COMPOSITES

3.1 Introduction

Previous research realized printing and in-situ curing of thermosets involving a highly reactive DCPD. However, DCPD monomer is toxic, volatile, and relatively low thermal stability comparing to the state-of-art high-performance epoxy-based thermosets. Though epoxy resins exhibit high mechanical performance, good thermal and chemical resistance, they are difficult to cure frontally due to their lower reactivity. For ring-opening polymerization, the driving force is the ring strain. The reported ring strain of three-member epoxide is ~ 54.4 kJ/mol, which is twice lower than the ring strain of DCPD (109.2 KJ/mol)[147]. Thus, lower reactivity epoxy requires higher curing temperature and extended curing period. Besides, UV-induced free radical polymerization is capable of curing epoxy within minutes, but limited UV penetration depth leads to weak interlayer bonding of the prints, thus affected the overall mechanical performance. 3D printing and in-situ curing of epoxy is still a challenge.

Previous literature used radical-induced cationic frontal curing (RICFC) to achieve frontal curing of epoxy with the assistance of iodonium hexafluoroantimonate (IOC-8 SbF_6, noted as I-Sb in this dissertation proposal) and tetraphenylethanediol (TPED, noted as I-TI) co-initiators[81]. Cationic polymerization is known to be less insensitive to curing temperature which makes them easier to initiate the monomer propagation than the

corresponding free radical polymerization. In the RICFC system, two mutually reactive initiators were introduced which facilitate the radical generation and utilize the heat released from the propagation reaction. Also, for RICFC, the front can be initiated using UV light and/or heat. More recently, another less nucleophilic counterion, tetrakis (perfluoro-tert-butyloxy)aluminate anion (noted as I-Al), was used to replace the hexafluoroantimonate with higher nucleophilicity to prevent chain termination as a result of the combination with the protonated alkene[148].

In this work, epoxy resin mixing with I-TI/I-Al initiating system is selected for frontal curing assisted direct ink writing (FCDIW). Front propagation behavior is measured and calculated. Meanwhile, one-dimensional (1D) and two-dimensional (2D) nano-/micro materials were incorporated in the epoxy resin-based frontal curable inks to tune the cure kinetics as well as the front propagation behavior. Bisphenol A diglycidyl ether (BADGE) epoxy resins were chosen as the thermosetting polymer matrix, for its exceptional mechanical, chemical and thermal performance. Furthermore, the proposed frontal curable resins are then used for printing continuous carbon fiber composites (c-CFRC) for high-performance applications. The epoxy resin ink formulations are illustrated in Figure 3.1 Ink Design and Preparation section. Neat epoxy resin and discontinuous filler incorporated epoxy resin printing is illustrated in Figure 3.2 FCDIW of Neat/ Discontinuous-Filler Incorporated Epoxy Resin section. The c-CFRC printing process is demonstrated in Figure 3.2 FCDIW of the c-CFRC section.

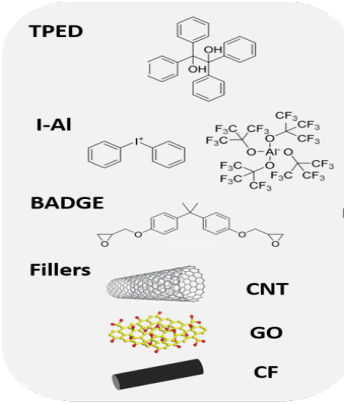

Figure 3.1 Scheme of FCDIW process. Ink Design and Preparation: frontal curable ink components and their chemical structures

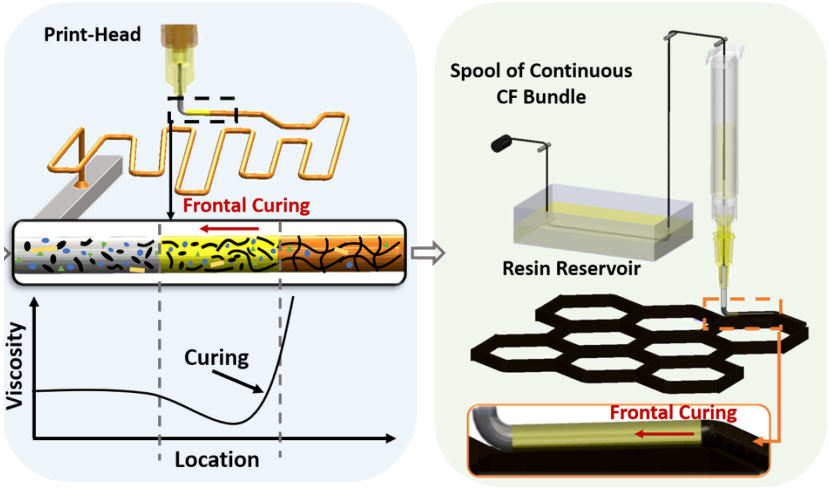

Figure 3.2 FCDIW of Neat/ Discontinuous-Filler Incorporated Epoxy Resin: scheme of FCDIW of neat epoxy and composites. The resin rapidly transforms from liquid or gel to solid-phase; FCDIW of the c-CFRC: scheme of FCDIW of the c-CFRC.

3.2 Experiment

3.2.1 Frontal curable epoxy resin preparation

I-Al (bis[4-(tert-butyl)phenyl]iodonium Tetra(nonafluoro-tert-butoxy)aluminate, TCI America) and I-TI (1,1,2,-tetrapheny-1,2-ethandiol, TPED, Sigma Aldrich) were

dissolved in Dichloromethane (DCM, Sigma Aldrich) before mixing with epoxy resin (EPON 828, Hexion). The mixture was then undergone rotary evaporation to remove the DCM solvent to obtain frontal curable epoxy resin inks. Different initiator concentrations of I-Al (0.02 mol%-1mol%) and I-TI (2mol%-8mol%) were prepared. Fillers including carbon nanotubes (multiwall CNT, Sigma Aldrich), carbon fibers (CF, kindly provided from NASA), graphene oxide (GO, prepared from flake graphite powder using modified Hummus method[149], used graphite powder Grade 230 is kindly provided from Asbury Carbons) were dispersed in DCM solvents before mixing with initiators and epoxy resins. Residual solvents were removed via rotary evaporation before printing.

3.2.2 Frontal curing assisted printing

The prepared epoxy resin was loaded in the cartridge before undergoing the extrusion-based printing process in the commercial Allevi 1 3D bioplotter. The bioplotter is a pneumatic pressure driven equipment and the pressure can be controlled in the computer printing program. A thermocouple is applied to the print-bed to control the bed temperature. During printing, the print bed was set to 100-150°C for frontal propagation initiation. Resins that sit in the cartridge were kept at 25 °C throughout printing. The curing starts and propagates along the print path in 3D space. For constructing different structures, the designed structure is first created in SolidWorks and converted into g-code.

3.2.3 Data capture and Image analysis

Non-destructive analysis (NDA) was used for analyzing frontal velocity (V_f) and frontal temperature (T_f) of the frontal curing assisted 3D printing process. A forward-looking infrared camera (FLIR A325sc) was applied to record the temperature profile of

the frontal curing and printing process. The recorded IR videos were converted into multiple IR heat maps at constant time intervals and used frontal velocity and frontal temperature calculations. Besides, a digital camera was used to record the actual printing process (optical videos). The NDA image analysis scheme and experiment setup are shown in Figure. 3.3.

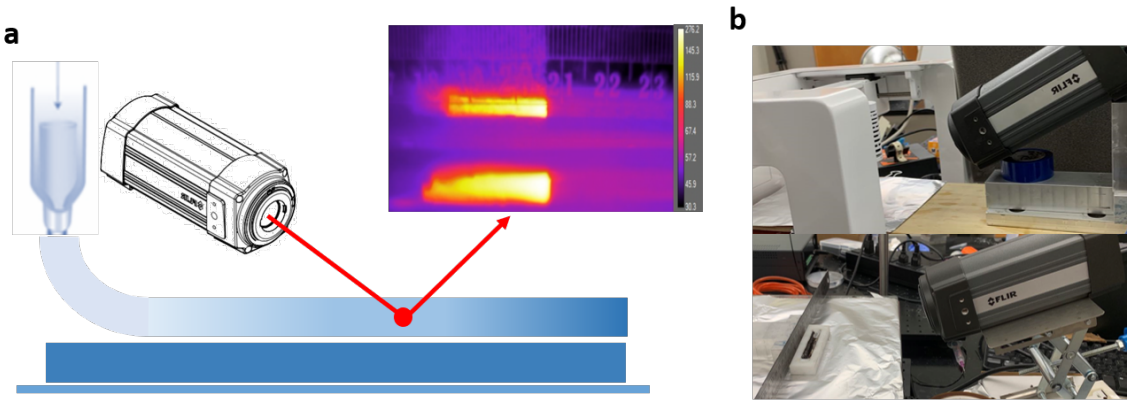

Figure 3.3 IR Image Analysis. a, IR image capture scheme and b, set up.

3.2.3.1 IR camera calibration

Before measurement, the FLIR IR camera was calibrated by the vendor (FLIR) and conducted a temperature check using the in-house thermocouple. The object's temperature is recorded by both the IR camera and thermocouple at the same time, the setup is shown in Figure 3.4a. The difference in temperature is in the range of ± 0.1°C, as shown in Figure 3.4b.

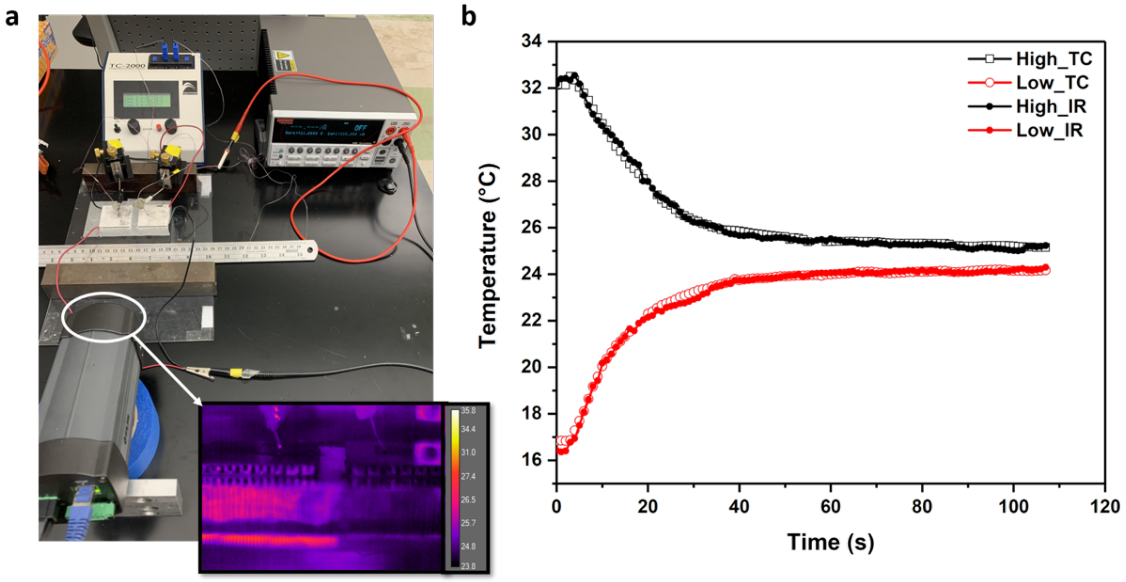

Figure 3.4 Calibration of IR camera. a, calibration setup. Two thermocouples are placed on two separate thermoelectric generators to capture the temperature. An IR camera is placed in front to capture the temperature. Both temperatures are recorded, processed and compared for temperature calibration. b, Temperature vs. time curve, TC stands for thermocouple and IR stands for the infrared camera.

3.2.3.2 Set up and preparation

IR camera was placed in front to capture the IR heat map during the epoxy frontal process with a ruler behind to record front locations and. A captured IR heat map is shown in the inset of the IR image capture scheme (Figure 3.3a). The resolution of the image is 320 x 240 pixels, and the pixels are converted to actual dimensions (in mm) referring to the ruler. The scale bar on the right side of the IR heat map indicates the temperature at each pixel shown in the image and temperature variation over time. The IR video is recorded for the overall printing process and saved for later frontal velocity and frontal temperature calculation. The actual set up is shown in Figure 3.3b.

3.2.3.3 Front temperature analysis

Reaction front is a zoon that propagates and moves forward to the adjacent region along with the uncured resins. The boundary of the propagation zone is defined as the locations where temperature dramatically changed from room temperature to onset temperature between two adjacent time frames. The onset temperature is referred to the corresponding DSC curves of that specific epoxy resin formulation. The temperature profile of each propagation zone is recorded that demonstrating the resin curing behavior. The maximum temperature at each time frame versus the front center point location is plotted, showing the temperature range and stability of the curing process. The temperature range is collected and compared among different resin formulations.

From the temperature distribution of the frontal process, the temperature increases significantly when reached the onset temperature and further increases when the front continues propagating to the adjacent region. This reveals the nature of the frontal curing process: heat dissipates to adjacent locations; initiates curing at that location and release exothermic heat for initiating the next region reaction.

3.2.3.3 Front velocity analysis

Front velocity is calculated by the distance moved by the front zone between each time frame. Each center point location of the front region at different time frames is recorded and plotted for calculating front velocity. The majority of data points have followed the trend. The slope of location vs. time curve is determined as the front velocity. Three series of heat maps were analyzed for one epoxy resin formulation.

3.2.4 Rheology measurement

Rheology performance was measured via a rheometer (TA Instruments AR-G2) and a 10 mm diameter parallel plate were used for characterization. Epoxy resin inks with different initiator concentrations and filler concentrations was used for measurement. Strain sweep, frequency sweep, and time sweep were measured at room temperature (25°C) and temperature sweep was characterized in the range of 20-80 °C at a constant frequency.

3.2.5 Heat of reaction, reaction kinetics, and thermal degradation

DSC analyses were employed on a DSC (Q20, TA Instruments) installed with a CFL-50 cooling system. Test specimens were loaded into aluminum hermetic pans and sealed with lids at room temperature (25°C). The weight of the specimen was determined through the analytical balance. Each specimen's weight was carefully controlled in a range of 2-5mg because of its highly exothermic nature, thus a higher loading mass may cause large temperature variation and affect results' accuracy. The curing profile measured a temperature range between 50 to 250 °C at a constant ramping rate (10°C). The reaction enthalpy is calculated by the total area of heat flow after baseline correction. Thermal degradation was measured via TGA (Q50, TA Instruments) equipment in air. Specimens were put in the chamber and chamber temperature was elevated from 25°C to 600°C at a constant ramping rate (10°C min^{-1}). The weight was measured at different temperatures and weight loss is calculated compared to the initial weight.

3.2.6 Mechanical characterization

Mechanical performance was conducted to analyze the printed tensile bars via the FCDIW process.

3.2.6.1 Neat resin/ discontinuous filler-filled epoxy composites

ASTM Type V tensile bar was fabricated via FCDIW. Tensile bars with different I-TI/I-Al molar ratios and composites with different filler types and filler concentrations were printed. Tensile bars with 4mol% I-TI and 0.05mol% I-Al and 2mol% I-Sb and 2mol% I-TI were prepared via conventionally oven cured (at 120°C for 4 hours) or bulk frontally cured as control specimens. Also, epoxy resin tensile bars with a stochiometric amine-based curing agent (CA 3300) were prepared (oven curing). The PTFE mold was used for conventionally cured specimens. Epoxy resins were poured into the mold and degassed under a vacuum to remove voids and bubbles before curing. Tensile tests were employed in the MTS Insight machine with a 30kN load cell. The crosshead speed was set to 2mm min^{-1}. The strain was measured by the increased crosshead distance over the original distance. Young's modulus was calculated overstrain ranging from 0.1% to 0.3%.

3.2.6.2 c-CFRC mechanical testing

c-CFRC was printed using the same printer with a self-modified coaxial nozzle to control the fiber/epoxy ratio of printed composites. The continuous carbon fiber tow was immersed in the frontal curable resin reservoir before printing. Later, the fiber tow was threaded through the cartridge and tip. For dual nozzle setup, frontal curable resins were loaded into the syringe and flew out via pneumatic pressure. And for single nozzle ones, inks were grafted onto the fiber tow and dragged out via dragging force with the nozzle

movement. The fiber/resin weight ratio was adjusted by tuning the nozzle gauge size and/or using coaxial nozzles (18G + 14G). Same as the neat epoxy resin printing, frontal curing starts instantaneously once the resin contact with the print bed and propagates along the print path.

Specimens were printed with different fiber/epoxy volume fractions and subject to tensile testing (ASTM D3039). The volume fiber/resin fraction of the fabricated c-CFRC was calculated via ASTM D3171. The crosshead speed is the same as neat resin specimens. Extensometer was employed for displacement measurement for strain and Young's modulus calculation. Young's modulus is determined by a strain rate of 0.3% - 0.6%.

3.3 Results and Characterization

3.3.1 Reaction kinetics study and thermal analysis

The rate of reaction, exothermicity, and thermal diffusion determine the front propagation behavior, which influences the polymer network structure and ultimate properties of printed parts are essential for FCDIW of epoxy resin-based process. The effects of initiator structure and concentration and nano-/micro-catalysts addition on epoxy resin frontal curing were studied to understand the relationships between ink composition, frontal behavior, and cure kinetics.

In frontal reaction, reaction exothermicity is the main driven force for constant front propagation. The heat of reaction (H_r) and its curing profile as a function of temperature are analyzed via Differential Scanning Calomerity (DSC). Figure 3.5a compares the curing profile of I-TI/I-Al epoxy resin inks to I-TI/I-Sb epoxy resin,

DCPD/GC2 and stochiometric amine-based epoxy resin system. In Figure 3.5, an accelerated rate of propagation was observed when a reaction was activated and the temperature rose quickly beyond 120 °C, suggesting an increased reactivity for I-TI/I-Al epoxy resins. The improved reactivity could be accredited to the in-situ formation of new catalyst species during the reaction[86] referring to the proposed RICFC reaction mechanism (Figure 3.6). A sharp heat flow of curing reaction with a steep slope upon initiation is shown in the curing profile of epoxy resins filled with 4 mol% I-TI/ 0.05 mol% I-Al initiator concentrations (Figure 3.5a). In contrast to the flattened heat flow profile with a much lower exothermic peak for stoichiometric aliphatic amine-based epoxy curing, the sharp peak and steep slope indicate the large exothermicity and high rate of reaction upon activation, similar to the thermal curing profile of DCPD frontal polymerization system with GCII catalyst. But a greater exothermic peak value and a right-shifted onset temperature indicate a more substantial exothermicity as well as a greater amount of energy needed for activation, and thus may yield a higher frontal processing temperature. Frontal processing at high temperature may cause undesirable resin curing pathway with the presence of second or even third exothermic peak as well as the color change from transparent to black or scarlet after curing if the thermal energy does not properly and timely dissipate, especially for resins with a higher level of initiator concentration (Figure 3.5b i). Also, the cured parts turn black, drastically different from conventionally cured epoxy with an orange color (Figure 3.5b ii) indicating that a higher reaction temperature leads to the lower molecular weight of cured polymer network and the incomplete and

irregular reaction pathway. The color change could also imply the occurrence of polymer degradation.

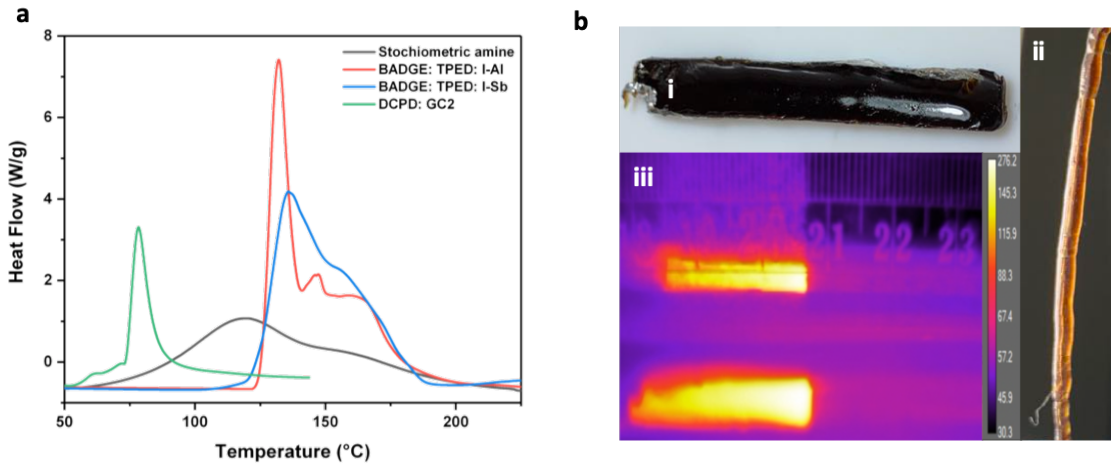

Figure 3.5 a, Cure kinetics characterization of stochiometric amine, TPED: I-Al, TPED: I-Sb cured epoxy and GC2 cured DCPD. b, Infrared (IR) image analysis of bulk resin front propagation and FCDIW front propagation. i, IR image of bulk resin front propagation; ii, picture of the frontal cured part (bulk, dark and opaque); iii, picture of FCDIW part (orange color).

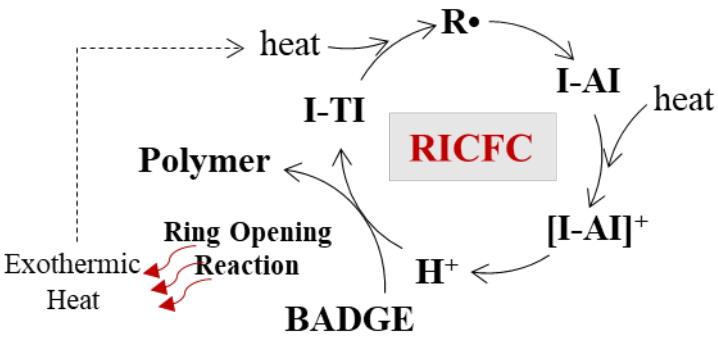

Figure 3.6 Radical induced cationic frontal reaction mechanism.

To evident the conjecture, the frontal curing process was analyzed via thermogravimetric analysis (TGA) to track reactant mass loss with increasing temperatures. The curve indicates an approximate 3% weight loss when the reaction

temperature exceeds ~260 °C and the degradation accelerated when the temperature reached ~280 °C (Figure 3.7).

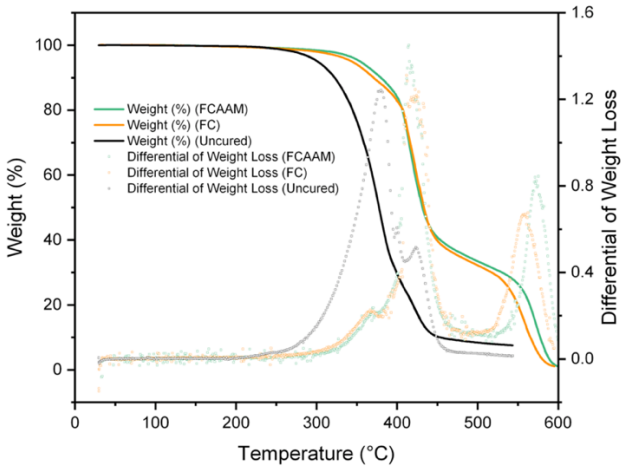

Figure 3.7 Thermal degradation in the air of cured / uncured epoxy with 4mol% I-TI and 0.05mol% I-TI initiator concentrations. Lines correspond to weight (%) and scatter plots correspond to a differential of weight loss.

The pot life of I-TI/I-Al epoxy resins was also determined via DSC (Figure 3.8). Different from DCPD, the RICFC system exhibited a much longer pot life up to several months.

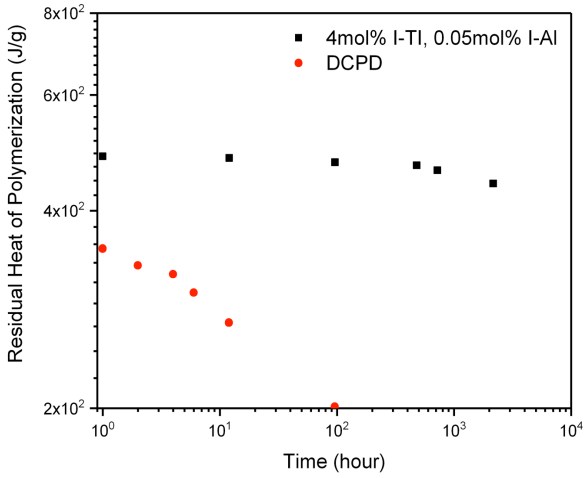

Figure 3.8 Pot life of the frontal curable epoxy resin

The inclusion of highly thermal conductive fillers such as carbon nanotube (CNT), graphene oxide (GO), and short carbon fiber (s-CF) is known to modify the curing kinetics of epoxy resins[150]. Specifically, the addition of CNT reduced activation energy in the early curing stage and facilitate the ring-opening in later reaction[150]. The effect of filler incorporation on the cure kinetics and frontal behavior in the proposed inks and compared the effect of different types of fillers were analyzed. 1D CNT, 2D GO, and microscale s-CF were incorporated in epoxy resin inks and their DSC profile was measured (Figure 3.9). The heat flow curve of all filler-incorporated resins exhibited a similar profile as the neat resins with a single sharp exothermic peak. The curve of all filler-incorporated resins exhibited a decreased onset temperature and peak temperature, suggesting a positive effect of filler incorporations on reactivity and cure kinetics.

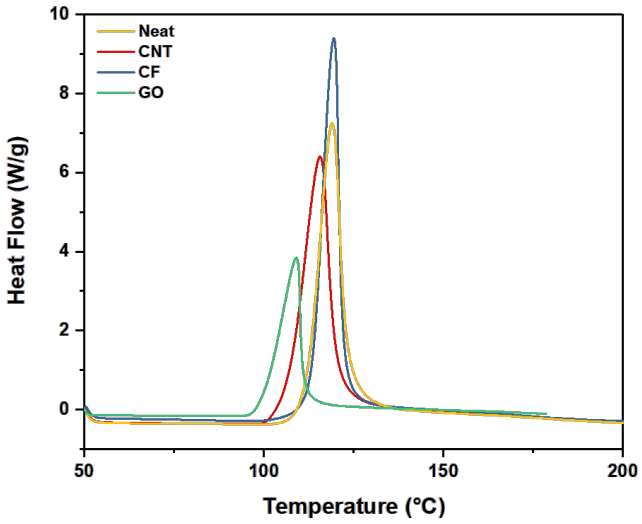

Figure 3.9 DSC of epoxy resins with different types of filler incorporated (CNT, GO, and CF)

The concentration effect of CNT fillers on curing profile was also analyzed and presented in Figure 3.10. With the increasing CNT concentrations, the initiating temperature is left-shifted while peak heat flow is lowered.

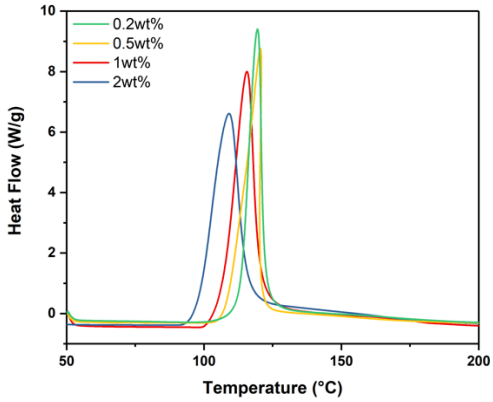

Figure 3.10 DSC of epoxy resins with different CNT concentrations

3.3.2 Front propagation analysis

The frontal behavior was characterized with front velocity (V_f), the distance that a frontal region could transport in unit time, and frontal temperature (T_f), the temperature of the reaction front, and front stability, the variation of the temperature range in the reaction front region. To provide insight on frontal behavior analysis, a high-resolution Forward-looking infrared (FLIR) camera was employed for in-situ monitoring of frontal reaction profile including front temperature and front velocity. A clear propagation zone is presented in each infrared (IR) thermal map representing the front temperature range and front zone location for this time (Figure 3.5b iii). The reaction front was generated a few seconds after initiation of the curing reaction, which released thermal energy,

diffused, and increased the temperature in the nearby region. These recorded IR thermal maps were used for V_f and T_f analysis (detailed description were noted in Section 3.2.2). One example of V_f and T_f analysis is shown in Figure. 3.11.

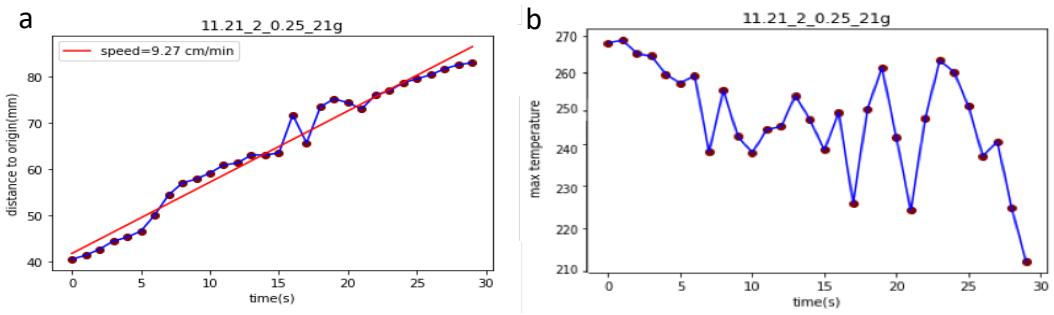

Figure 3.11 Illustration of a, frontal velocity and b, frontal temperature measurement of printing and in-situ curing of BADGE with the addition of TPED and I-Al (TPED: I-Al molar ratio = 2mol%: 0.25mol%).

Thermal initiator concentrations ranging from 2 mol% to 8 mol% and the cationic initiator concentrations ranging from 0.02 mol% to 2 mol% were analyzed via IR image analysis and corresponding V_f and T_f for each formulation were shown in Figure 3.11. From the figures, both initiators exhibited a positive effect on V_f and T_f, but I-Al presented a more significant effect comparing to I-TI. Moreover, the error bar indicates the stability of the front propagation. It is shown in the figures that the front is less likely to stabilize with higher T_f.

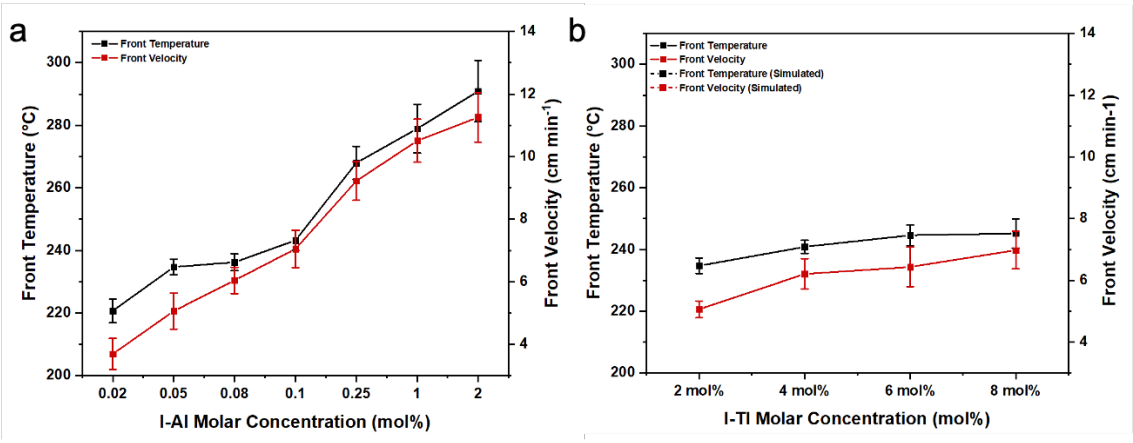

Figure 3.12 a, Effect of I-Al concentration on front temperature and front velocity. Dashed lines represent simulation results. b, Effect of I-TI concentration on front temperature and front velocity.

Further, the simulation was included to analyze the frontal curing behavior of different resins. It is conducted based on a numerical model including two partial differential equations of heat transfer and polymer reaction. The principles of the computational modeling were illustrated as below:

Computational modeling was conducted for the current RICFC system in addition to infrared (IR) in-situ monitoring and image analysis. The front propagates via the coupling of thermal diffusion and Arrhenius reaction kinetics[151]. Thus, the propagation can be described by the following two partial differential equations (PDE):

$$\begin{cases} \kappa\left[\frac{\partial^2 T}{\partial x^2}+\frac{\partial^2 T}{\partial y^2}+\frac{\partial^2 T}{\partial z^2}\right]+\rho H_r\frac{\partial \alpha}{\partial t}=\rho C_p\frac{\partial T}{\partial t} & (3.1) \\ \frac{\partial \alpha}{\partial t}=Aexp(-\frac{E}{RT})(1-\alpha)^n\alpha^m f_d(\alpha) & (3.2) \end{cases}$$

where T (K) is the temperature; α is the degree of cure; κ (W m^{-1} K^{-1}) is thermal conductivity; C_p (J kg^{-1} K^{-1}) is the specific heat; ρ (kg m^{-3}) is density; H_r(J kg^{-1}) is the total enthalpy of the reaction; r and z (m) are the radial and longitudinal coordinates; and

t (s) is the time. The first PDE corresponds to the heat dissipation at x, y, z directions at each time interval. Different from conventional heat transfer equations, here the system's heat supply comes from the exothermic reaction and the amount of heat varies according to time and degree of cure, which comes to the second PDE. The second equation represents the cure kinetics of the frontal polymer reaction. In the model, A is the pre-exponential factor, E is the activation energy, R is the universal gas constant and n and m are the two orders of reaction constant correlated with the Prout-Tompkins model for autoactivation effects. Isothermal thermoset curing has two distinct stages: chemically dominated and diffusion dominated. The time scale for reaction includes chemical reaction time and time for the reactant's diffusion. Initially, the reaction was driven by a chemical reaction. Later, when the time of diffusion of chemical is larger than a chemical reaction, the diffusion of reactant dominates the reaction. For the nth-order model, it is unable to describe the diffusion control dominated stage[152]. Initial and boundary conditions used in the computational model was set as follows:

$$T(x, y, z, t = 0) = T_0 \tag{3.3}$$

$$\begin{cases} \alpha(0 \le x^2 + y^2 \le r^2, z, t = 0) = \alpha_0 & (3.4) \\ T(0 \le x^2 + y^2 \le r^2, z = 0, t) = T_{initiate}\ 0 \le t \le t_{initiate} & (3.5) \end{cases}$$

$$\frac{\partial T}{\partial z}\ (0 \le x^2 + y^2 \le r^2, z = 0, t) = 0\ t > t_{initiate} \tag{3.6}$$

The heat source supply was given in phase one, while other phases were assumed to be in adiabatic conditions. T_0 is initial temperature, set to 25 °C and α_0 is the initial degree of cure of the ink, set to 0.01. r is the radius of printed filament and the printed filament is deemed as a round shape. The equations 3.3-3.6 includes the following information for

the numerical simulation: the temperature of the rod is at the room temperature; the rod is at an uncured state at the beginning; we apply the initial heat to the bottom of the rod; and the initial heat supply only last for a short period of time. The computational modeling implemented in COMSOL. All material data used in the numerical simulation was shown in Table 3.1.

Table 3.1 Physical and thermal properties of the various components used in numerical simulation

	κ (W m^{-1} K^{-1})	ρ (kg m^{-3})	H_r (J g^{-1})	C_p (J kg^{-1} K^{-1})
BPA epoxy resin	0.14[1]	1,190[a]	484[b]	1,200[1]
CNT	6.6[153]	1,600[153]	-	686[153]
Carbon fiber	10.45[38]	1,760[38]	-	795[38]

[a] Calculated by Archimedes method
[b] Obtained from DSC heat flow curve

The simulated results of V_f and T_f are shown as the dashed lines in Figure 3.14, a complement to experimental analysis. The numerical simulation presented similar processing trends trend in front temperature and front velocity for the neat epoxy resin to experiment results. The simulated IR heat maps for the FCDIW process were similar to the actual ones (Figure 3.13). Based on the neat resins frontal curing study, 4mol% I-TI and 0.05mol% I-Al showed a suitable V_f and T_f, and was selected as the initiator concentration in the rest of the study.

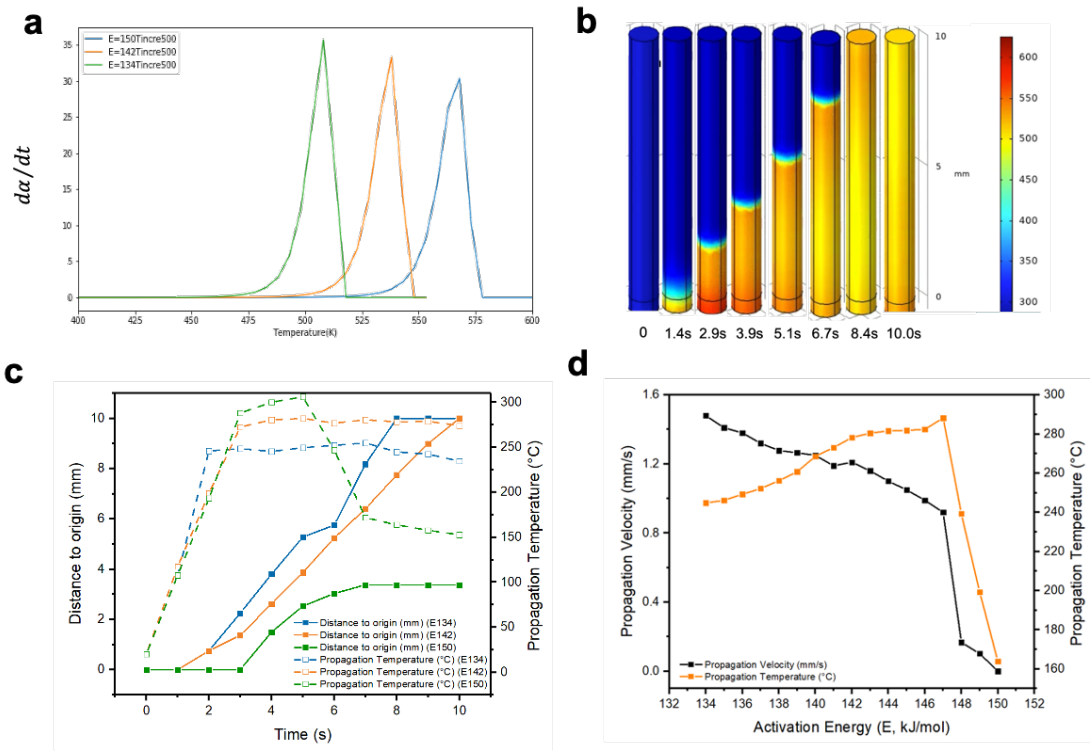

Figure 3.13 Numerical simulation (temperature scale bar is in Kelvin (K)). a, reaction rate vs. temperature. b, front propagation with increasing time (strand diameter: 1 mm; strand diameter: 0.3 mm; E: 134kJ/mol). c, Propagation distance and propagating temperature vs. time plot. d, Propagation velocity and temperature with activation energy ranging from 134 to 150 kJ/mol.

IR analysis were also conducted for calculating V_f and T_f of nanofiller incorporated epoxy resins printing (Figure 3.14).

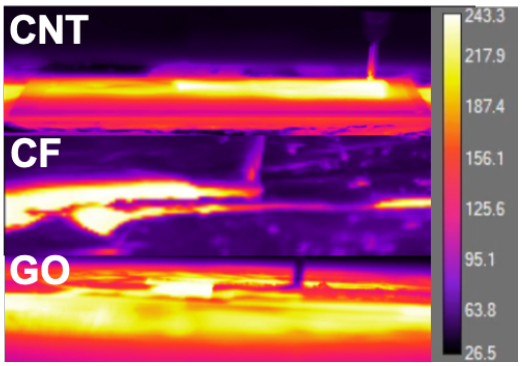

Figure 3.14 Non-destructive IR analysis for V_f and T_f of epoxy resin frontal printing with different nanofiller incorporation.

An analysis example was shown in Figure. 3.15 for CNT incorporated epoxy resin system.

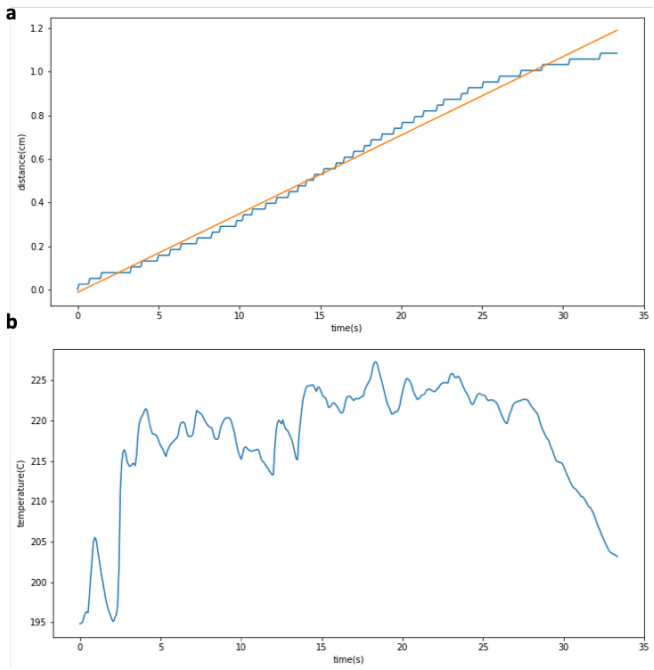

Figure 3.15 Demonstration of frontal velocity and frontal temperature measurement results for filler incorporated epoxy resin printing (I-TI: I-Al=4mol%: 0.05mol%, CNT 1wt%)

The overall V_f and T_f results are calculated and demonstrated in Figure 3.16. From Figure 3.16, CNT-incorporated resins showed a lower front temperature and more uniform temperature distributions in comparison to neat resins, indicating a more effective heat transfer in reaction propagation direction overheat loss in surroundings. Compared to 1D CNT, the inclusion of 2D GO further reduces the front temperature to ~220°C but presented a lower front velocity due to the entrapment of epoxy monomers or oligomers, and thus, reducing the free molecular segments[25]. Further, the inclusion of microscale carbon fiber shows a higher V_f and T_f corresponding to a retarded cure kinetics due to the

significant steric hindrance effect on the epoxy curing pathway, not compelling to the catalytic effect of nanoscale fillers[26].

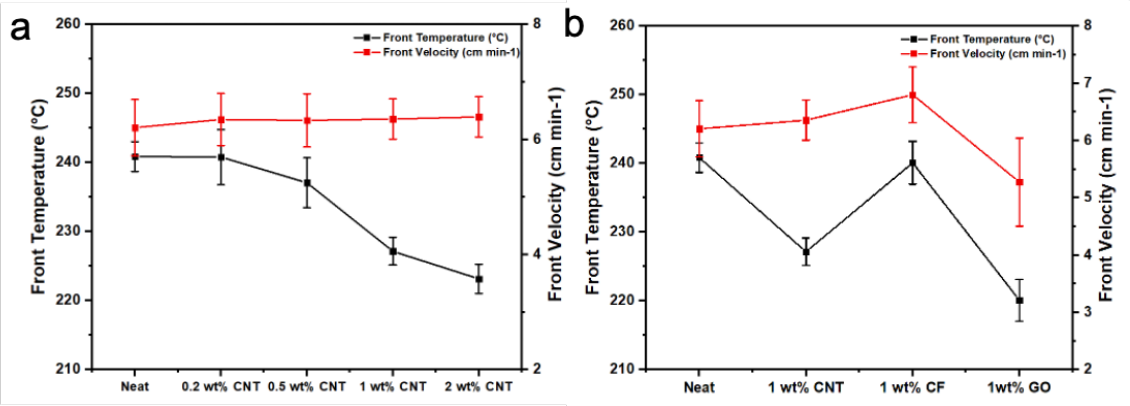

Figure 3.16 Effect of (a) filler concentration and (b) type of filler on front temperature and front velocity.

From the experimental analysis, a process map for FCDIW epoxy resin with the proposed I-TI/I-Al initiating system with/ without the inclusion of nanofillers is shown in Figure 3.17. The processability of a given ink composition was determined by its front behavior and followed by the qualifications that a certain V_f (~6 cm min^{-1})[18] should be met for continuous and rapid production while keeping the T_f below 260 °C to avoid overheating and resulting in the undesired polymer network. From the process map, initiator concentrations in a range of 0.05 mol% to 0.08 mol% for I-Al while I-TI concentration stays between 2mol% and 6mol% meet the criteria. In this proposed range, printed specimens exhibited a clear yellowish color similar to conventional oven-cured specimens (Figure 3.18), thus were categorized as the printable region (noted as 'Ideal' in Figure 3.17) for FCDIW. According to previous frontal propagation analysis, discontinuous micro/nano-fillers inclusion facilitates the frontal propagation with reduced

T_f and similar V_f, also falls in the printable region. Specimens that were fabricated with higher initiator concentrations exhibited T_f higher than 260 °C and caused degradation (as shown in Figure 3.5b i), thus is categorized to the 'degradation' region which is not ideal for printing even though its V_f qualified. Previous efforts regarding frontal curing of BPA epoxy resins are reviewed as below:

Attempts for frontal curing of BPA-epoxy resins can be traced back to 1975 with amines[154, 155]. Later, in 1997, Chekanov et al. reported an aliphatic amine and boron trichloride/ amine complex-based bisphenol-A-diglycidylether (BADGE) frontal curing system with a maximum front velocity of 0.8 cm/min, far below the required front velocity (~6 cm min^{-1}) for frontal curing assisted manufacturing[38, 151]. Cationic polymerization is known for its high reaction rate and exothermicity. If incorporated into the current radical polymerization system, it will be a favorable approach to overcome the low reactivity of epoxy[81]. Radical induced cationic frontal curing (RICFC) of BPA-epoxy resins has been demonstrated with a dual initiating system, hexafluoroantimonate (SbF_6^-)-based iodonium salt (denoted as I-Sb) as cationic initiator and thermo-labile compounds 1,1,2,2-tetraphenyl-1,2-ethanediol (TPED) as a radical thermal initiator (I-TI)[81,88]. Such a reaction system obtained a front velocity of 2.7 cm/min, more than three times higher than Chekanov's result, but still difficult for self-supported frontal propagation[38, 81]. Recently, iodonium salt with weaker nucleophilicity counterion (fluorinated alkoxyaluminate (p-octyloxyphenyl)phenyliodonium salt, denoted as I-Al) was developed and the new I-TI/ I-Al initiating system increased the front velocity of BPA-epoxy reaction to 10 cm/min[98, 148]. Though a highly efficient initiating system provides enough exothermicity and obtains

a high reaction rate, the resultant epoxy resins turned scarlet or even black after curing, indicating undesired and uncontrolled reaction pathway occurred during curing caused by a large evolution of exothermicity. Also, excessive exothermicity increases the reaction temperature (nearly 300°C) and may cause polymer degradation. To provide an insight on the significance and challenges toward the FCDIW process, the energy-saving index was defined as the amount of energy-saved in consideration of the demand for a specific polymer, and frontal reaction capability was defined as the ratio of exothermic energy to the activation energy. DCPD shows high frontal capability while the energy-saving index is very low. Epoxy resin is a common thermoset in the industry, but its frontal reaction capability depends on the curing agents. Amine-based agents show very low capability for frontal curing of epoxy resins. I-Al or I-Sb-based agents demonstrate a high energy-saving index and also high frontal reaction capability. The previous experiment results are summarized in a process map as a guidance for epoxy resin front curing under current initiating and catalyst system, shown in this slide. The processability of a given ink composition was determined by its front behavior, followed by two qualifications: firstly, a certain front velocity (~6 cm min-1 according to the ref) should be met for continuous and rapid production, secondly, keeping the T_f below 260 °C to avoid overheating. Based on these criteria, the map was separated into overheating, printable and low-rate region. And parts cured with front temp below 240°C is ideal since almost no weight loss for parts frontally cured below this temp according to the TGA analysis. And by tuning of the ink formulation with nanostructured catalyst, we could get the front temp below 240 °C and

get the front velocity and front temp closer to the DCPD ones (noted as the grey square in this process map).

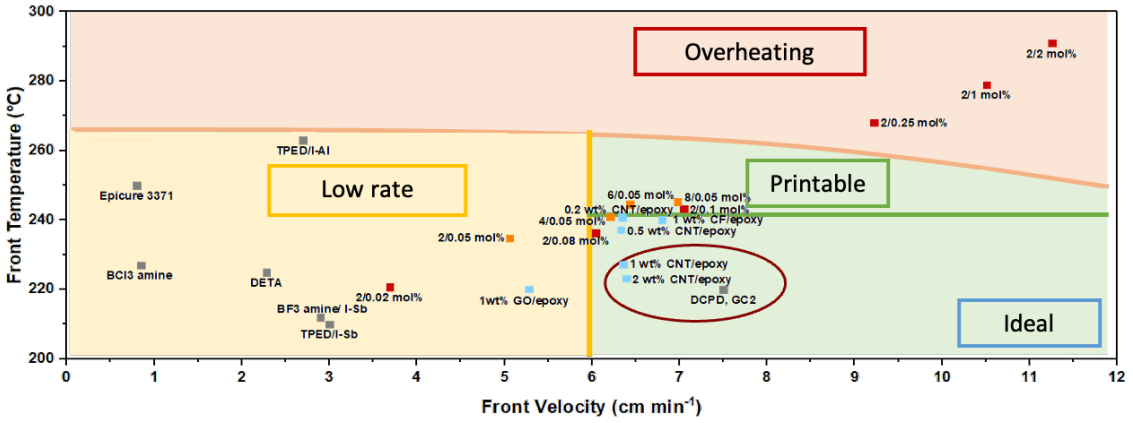

Figure 3.17 FCDIW Process Map: Blue, green and orange areas represent three processability regions of 'Low rate, 'Printable', 'Overheating' and 'Ideal' for FCDIW process, respectively. Data points located in the Front Ceased region stands for the resin/initiator systems with limited exothermicity and yielding a low processing speed insufficient for FCDIW[18]. Data points fell in the Ideal region is proved to be suitable for FCDIW with adequate processing speed and moderate processing temperature. Data points in the Degradation region presented exceeding processing temperature that turns the specimens from clear to dark color. Symbol color: grey is for previously reported values; red is for I-TI/I-Al with 2mol% I-TI and varying I-Al; orange is for I-TI/I-Al with 0.05mol% I-AI and varying I-Tl; blue is for discontinuous-filler incorporated specimens[38, 81, 151, 154, 155,38, 81, 88, 98, 148].

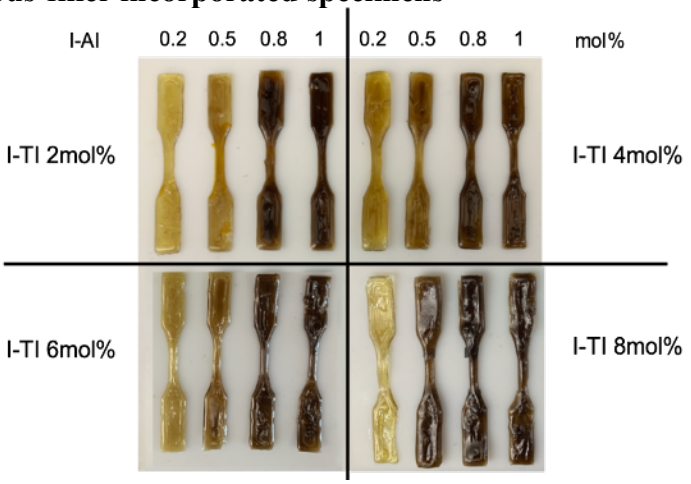

Figure 3.18 Printed specimens with different imitator concentrations.

3.3.3 Reaction kinetics modeling

As mentioned in Section 3.2.5, the DSC of frontal curable epoxy resins were analyzed. The conversion rate and reaction rate were calculated. The reaction kinetics of epoxy resin with different I-TI/I-Al molar concentrations and filler concentrations/ types were tested using the method introduced above and the results were integrated to Figure 3.19-3.21.

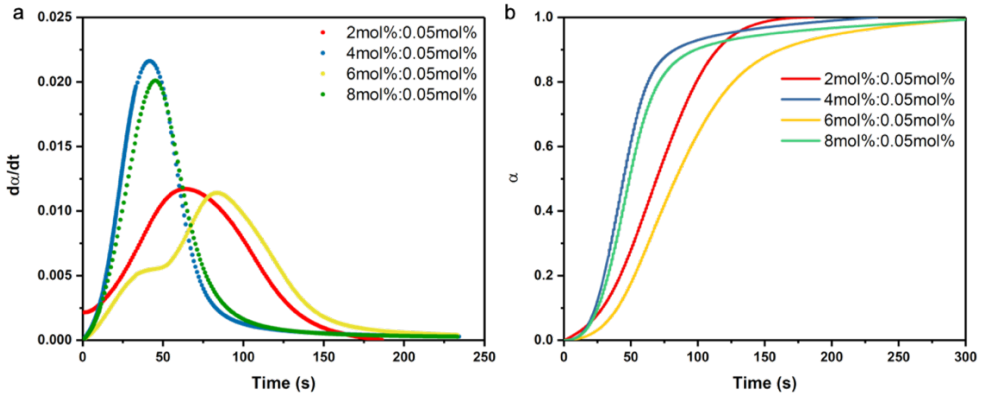

Figure 3.19 I-TI molar concentration effect on reaction kinetics (a) $\frac{d\alpha}{dt}$ vs. time; (b) α vs. time.

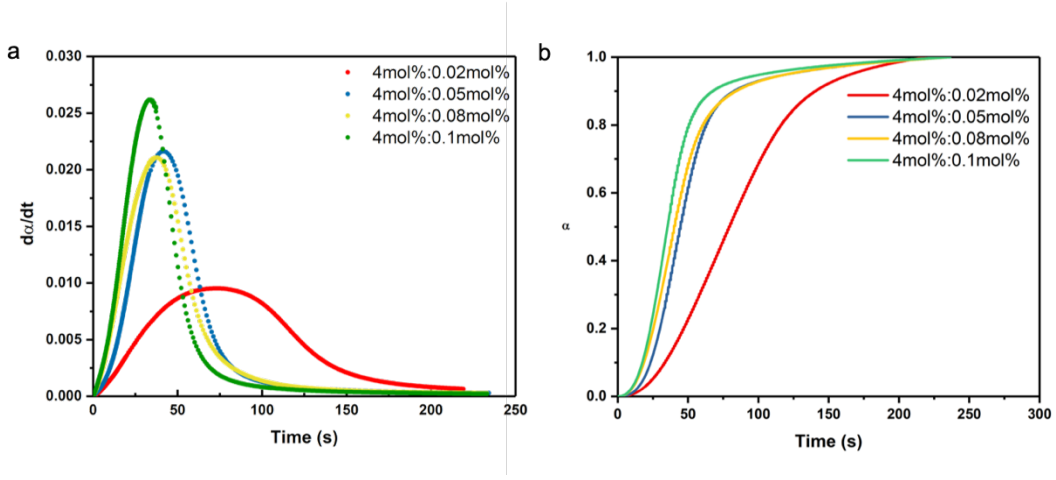

Figure 3.20 I-Al molar concentration effect on reaction kinetics (a) $\frac{d\alpha}{dt}$ vs. time; (b) α vs. time.

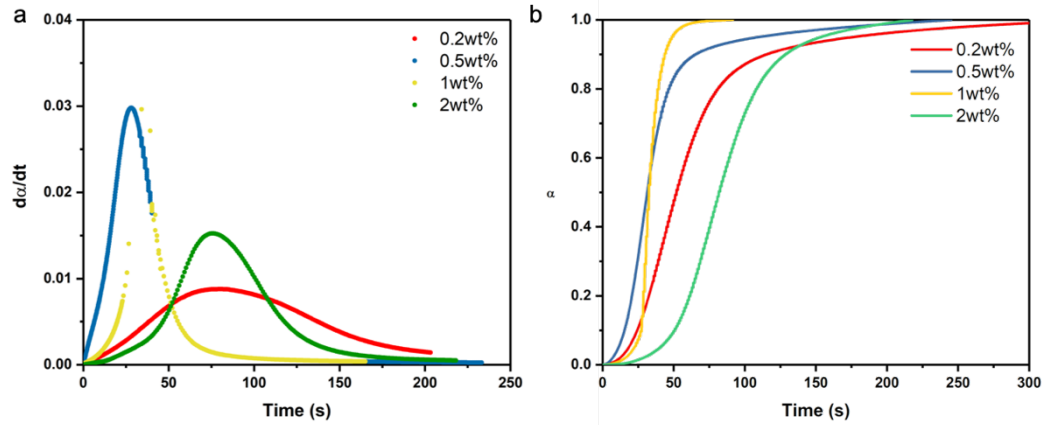

Figure 3.21 Filler molar concentration effect on reaction kinetics (a) $\frac{d\alpha}{dt}$ vs. time; (b) α vs. time.

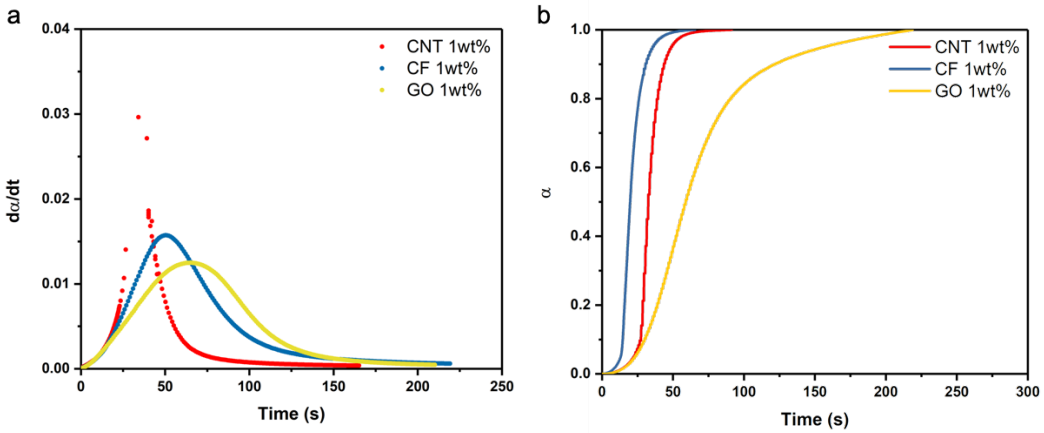

Figure 3.22 Filler type effect on reaction kinetics (a) $\frac{d\alpha}{dt}$ vs. time; (b) α vs. time.

In the thermal model, front propagation is described in thermal diffusion and Arrhenius reaction model. From the model, the driving force is the exothermicity of the frontal reaction, represented as H_r and $\frac{\partial \alpha}{\partial t}$ in equation (3.2). These H_r and $\frac{\partial \alpha}{\partial t}$ along with

activation energy (E_a), time (t), temperature (T) and conversion rate (α) all together describe the reaction kinetics of the frontal reaction.

Reaction kinetics of the frontal reaction was determined by DSC analysis of different resin formulations and analyzed by using the empirical models to fit the DSC experimental data.

Curing reactions of frontal curable epoxy resins are highly exothermic, the healing flow measured in DSC is proportional to both the overall heat release and curing rate:

$$\frac{dQ}{dt} = Q_{cure}\frac{d\alpha}{dt} = Q_{cure}k(T)f(\alpha) \tag{5.4}$$

Here, $\frac{dQ}{dt}$ is the heat flow, t is the time, Q_{cure} is the total heat released for complete curing, $k(T)$ is the temperature-dependent the reaction rate constant, and $f(\alpha)$ is the differential conversion function based on reaction mechanism. Mechanically, the polymerization reaction. The RICFC reaction is not limited to one chemical reaction, and the consecutive reaction process occurs simultaneously. Thus, an autocatalytic reaction model was selected, shown as below:

$$f(\alpha) = \alpha^m(1-\alpha)^n \tag{5.5}$$

Here, m and n are reaction orders. $k(T)$ is dependent on temperature according to the Arrhenius equation:

$$k(T) = Aexp(-\frac{E}{RT}) \tag{5.6}$$

Where A is the pre-exponential factor, E is the activation energy, T is the absolute temperature. For non-isothermal curing, temperature varies with time at a constant heating rate, then:

$$\frac{d\alpha}{dt} = \beta\frac{d\alpha}{dT} = Aexp(-\frac{E}{RT})f(\alpha) \quad (5.7)$$

Here $\beta = \frac{dT}{dt}$. Thus, the equation becomes:

$$\frac{d\alpha}{dt} = Aexp(-\frac{E}{RT})\alpha^m(1-\alpha)^n \quad (5.8)$$

For model fitting, using the phenomenological model (Kama et al.[156] kinetic model):

$$\frac{d\alpha}{dt} = (k_1 + k_2\alpha^m)(1-\alpha)^n \quad (5.9)$$

$$k_i = k_{i0}\exp(-\frac{E}{RT}) \quad (5.10)$$

Before model fitting, the parameters of kinetic models were determined via model fitting using the above Kama kinetic model. The model fitting was conducted in MATLAB and the code and output were included in Figure B1-2 (Appendix B). One demonstration of the fitted curve of $\frac{d\alpha}{dt}$ vs. α was demonstrated in Figure 3.23 to determine the set of parameters in kinetics models. All calculated reaction kinetics parameters are listed in Table B1-2.

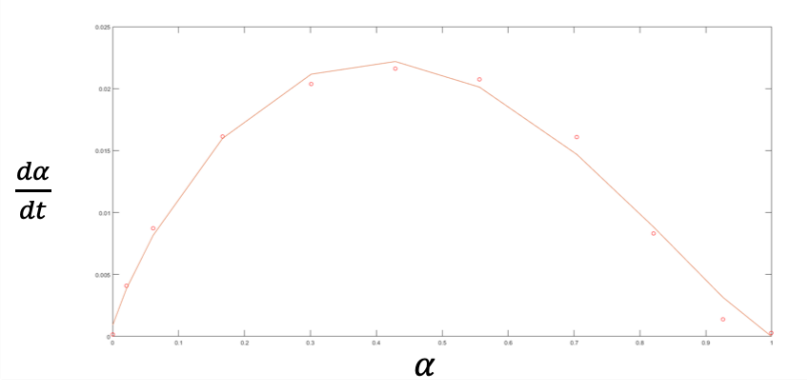

Figure 3.23 Demonstration of fitted $\frac{d\alpha}{dt}$ vs. α

And the fitted $\frac{d\alpha}{dt}$ vs. time and α vs. time curves of different formulations were plotted and compared with the experimental data, as shown in Figure 3.24-3.27.

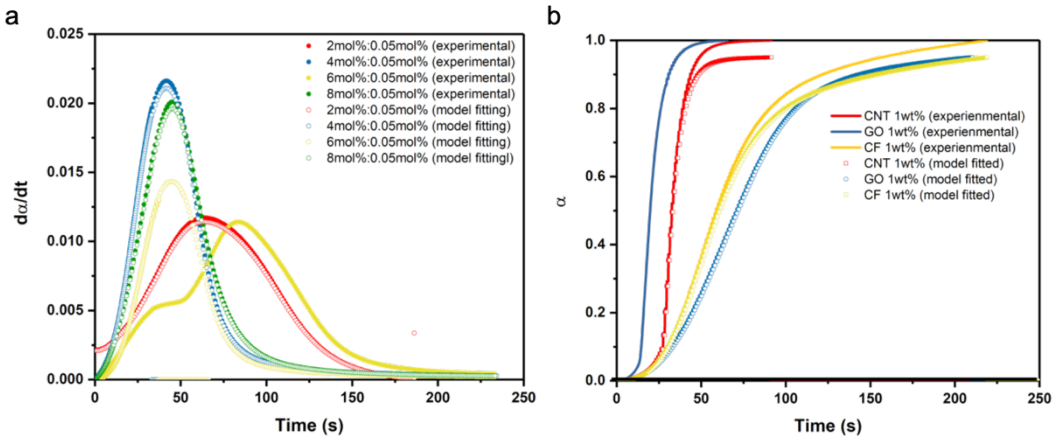

Figure 3.24 I-TI molar concentration effect on reaction kinetics (a) $\frac{d\alpha}{dt}$ vs. time; (b) α vs. time.

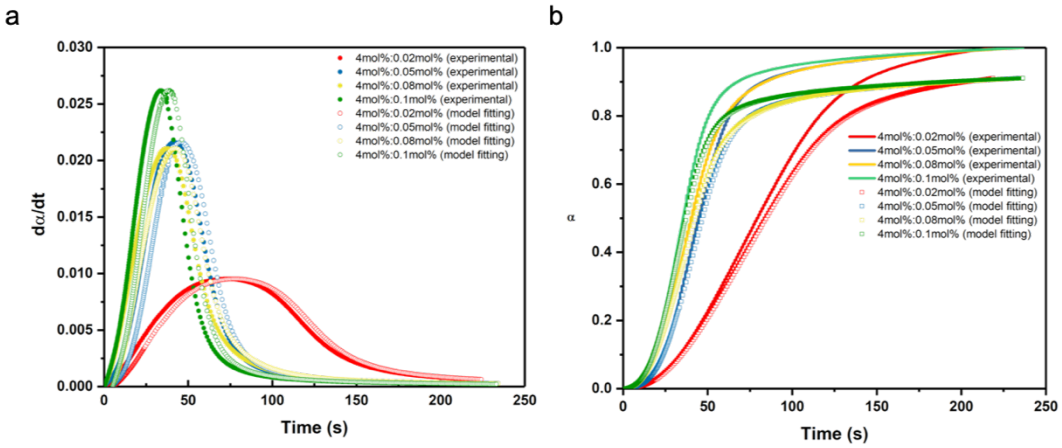

Figure 3.25 I-Al molar concentration effect on reaction kinetics (a) $\frac{d\alpha}{dt}$ vs. time; (b) α vs. time.

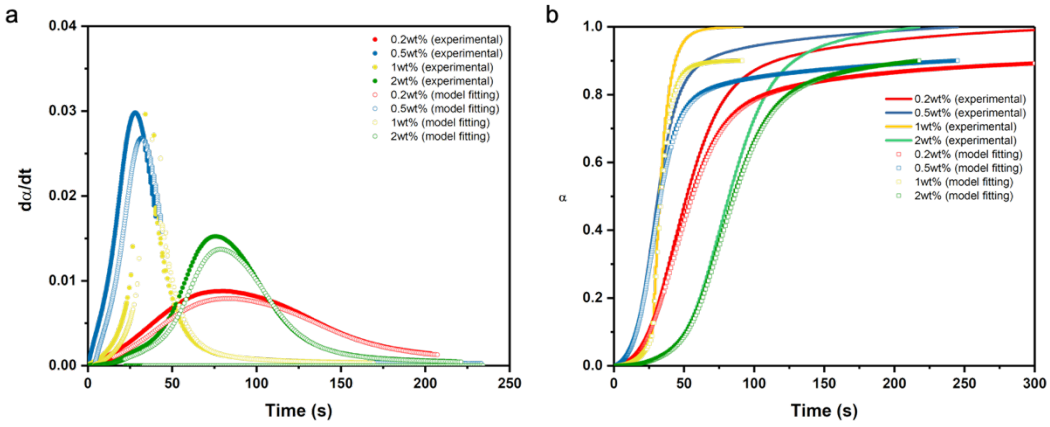

Figure 3.26 Filler molar concentration effect on reaction kinetics (a) $\frac{d\alpha}{dt}$ vs. time; (b) α vs. time.

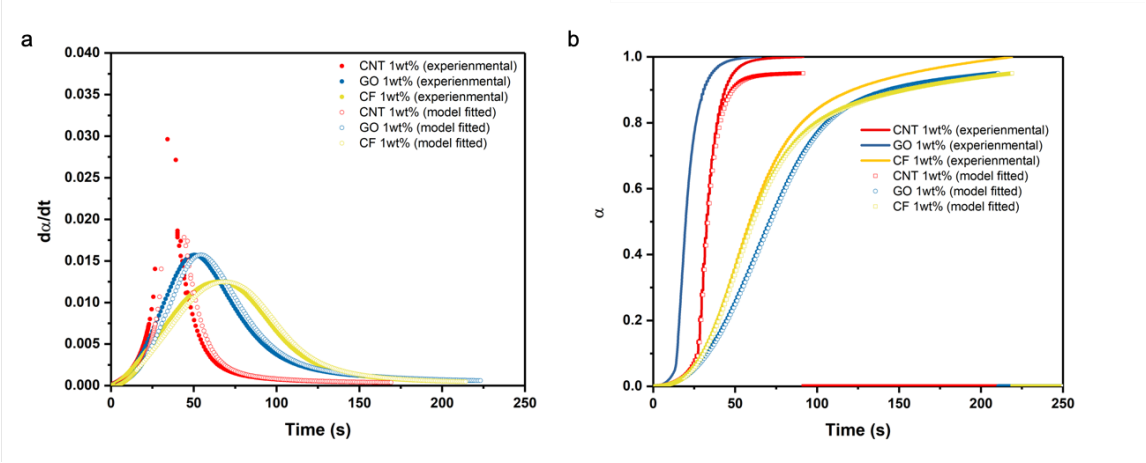

Figure 3.27 Filler type effect on reaction kinetics (a) $\frac{d\alpha}{dt}$ vs. time; (b) α vs. time.

3.3.4 Rheology measurement

3.3.4.1 Viscosity

Rheology behavior determines the ink printability. The viscosity of neat resin inks is not sensitive to time and initiator concentrations and exhibited a shear thinning tendency

at high shear rates (Figure 3.22). But viscosity increases with increasing CNT concentrations and CNT/ epoxy resin demonstrated a noticeable shear thinning behavior facilitating the extrusion process (blue and grey lines in Figure 3.22). With increasing filler concentrations, more obvious shear thinning behavior was observed, especially when CNT concentrations reached 1wt% and 2wt%, thus, resulting in a higher tolerance on fluid flow rate.

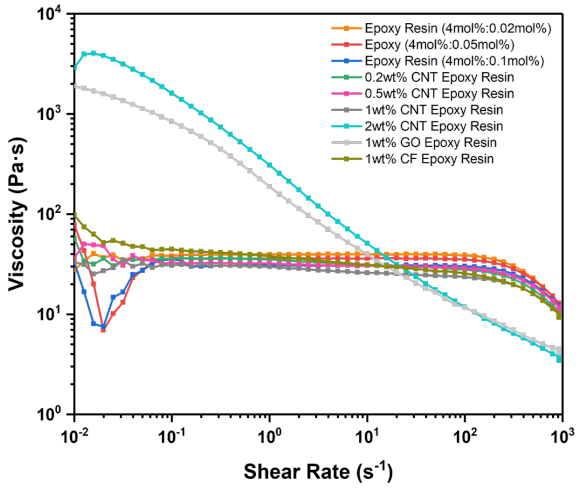

Figure 3.28 Viscosity changes over shear rate for different ink formulations

The frontal reaction is an active propagation process, temperature effects on viscosity affect the printing process and print job quality, thus, were also analyzed and shown in Figure 3.29.

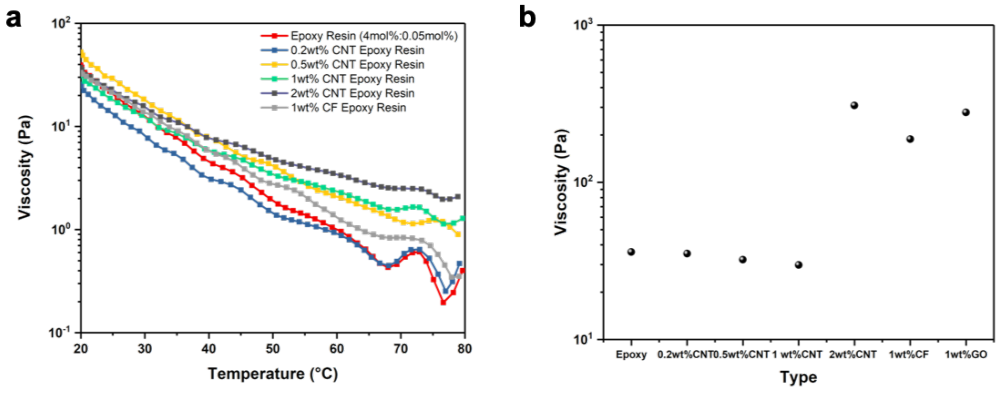

Figure 3.29 Rheological behavior characterization. a, Viscosity vs. shear rate of neat epoxy resins (different initiator molar ratio and incorporated CNT); b, Effect of initiator ratio and molar filler addition on viscosity.

3.3.4.2 Viscosity modeling

Due to the limitation of temperature vs. viscosity experimental analysis, the overall curve of viscosity behavior of the reactive matrix before gelation will be studied. The effect of temperature on the resin viscosity was first analyzed via rheology measurement (temperature below 80°C). The viscosity between 80°C and reaction start point and any points beyond reaction start point were analyzed via viscosity modeling. The Arrhenius type equation and Williams-Landel-Ferry (WLF)[156] function were applied to experimental data:

$$\eta(T) = \eta_g \exp[-\frac{C_1(T - T_{g0})}{C_2 + T - T_{g0}}] \tag{5.11}$$

Here T_{g0} is the glass transition temperature, η_g is the viscosity at T_{g0}, and constant C_1 and C_2 are determined from the rearranged WLF function:

$$T - T_{g0} = -C_2 - C_1 \frac{T - T_{g0}}{\ln(\eta/\eta_g)} \tag{5.12}$$

The calculation and analysis are shown in Figure 3.30.

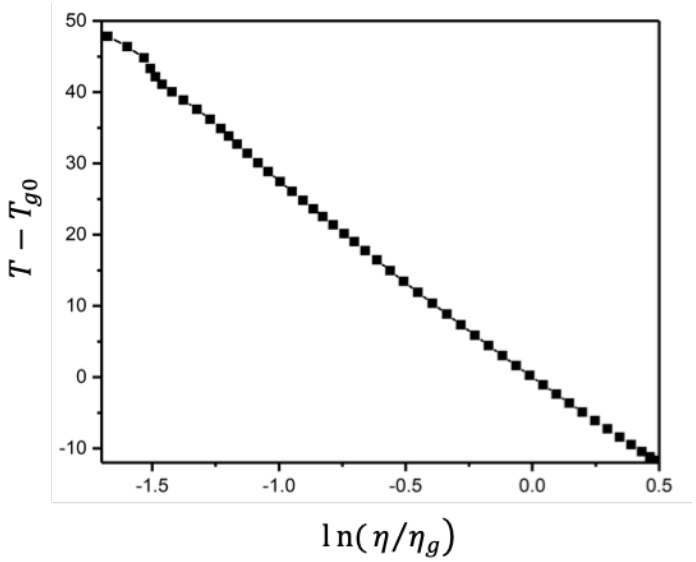

Figure 3.30 Determine the constant C_1 and C_2 of the WLF equation.

In order to describe the change of viscosity during curing reaction, chemo-rheological models proposed by Castro and Macosko[156] were applied to the isothermal data:

$$\eta(T,\alpha) = \eta_0(T)\left(\frac{\alpha_g}{\alpha_g - \alpha}\right)^{A+E\alpha} \tag{5.13}$$

Define $n = A + E\alpha$, then the equation becomes:

$$\eta(T,\alpha) = \eta_0(T)\left(\frac{\alpha_g}{\alpha_g - \alpha}\right)^{n} \tag{5.14}$$

modified by WLF:

$$ln\frac{\eta}{\eta_g} = -\frac{C_1(T)[T - T_g(T,t)]}{C_2 + T - T_g(T,t)} \tag{5.15}$$

Substituting

The slope of $ln(\frac{\alpha_g}{\alpha_g-\alpha})$ vs. $ln(\frac{\eta}{\eta_g})$ linear plot (Figure 3.31) is the exponent n in the above equation. The n was determined to be 1.79.

$$\eta(T,\alpha) = \eta_g \frac{C_1(T)[T - T_{g0}]}{C_2 + T - T_{g0}} (\frac{\alpha_g}{\alpha_g - \alpha})^n \quad (5.16)$$

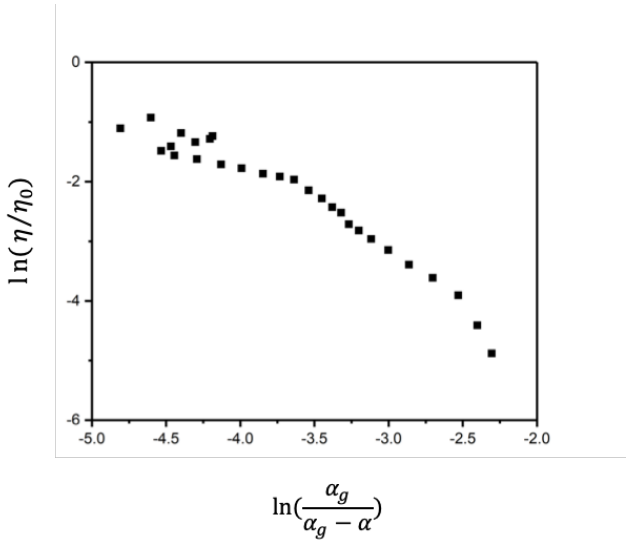

Figure 3.31 $ln(\frac{\alpha_g}{\alpha_g-\alpha})$ vs. $ln(\frac{\eta}{\eta_g})$ linear plot

All the parameters used in the chemo rheological model were calculated and listed in Table 3.2.

Table 3.2 Parameters of chemo rheological model

η_g (Pa s)	C_1	C_2	T_{g0} (K)	α_g	n
10^{12}	27.611	16.4893	324.8	0.013	1.79

[a] fractional conversion (α_g) (at gel point) and gel temperature T_{g0} are obtained from the DSC curve

[b] data referred to reference [156].

The results of the modeling are presented in Figure 3.32. The results are informative for governing the process parameters during the printing and in-situ curing process.

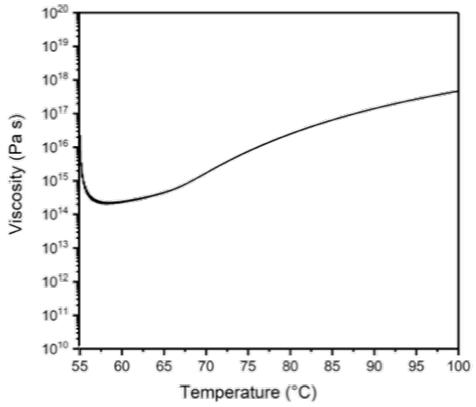

Figure 3.32 The complex viscosity as a function of temperature (model fitted)

3.3.4.3 Viscoelasticity

Resin's viscoelastic behavior was analyzed in Figure 3.33. a set of oscillatory experiments were conducted for viscoelastic measurements of the inks. First, an oscillation strain sweep was tested suggesting the linear viscoelastic region is under 1% strain amplitude (Figure 3.33a). Then the subsequent oscillatory frequency sweep measurements were conducted at 1% strain (Figure 3.33b). The results presented that the resins will remain its shape after extrusion.

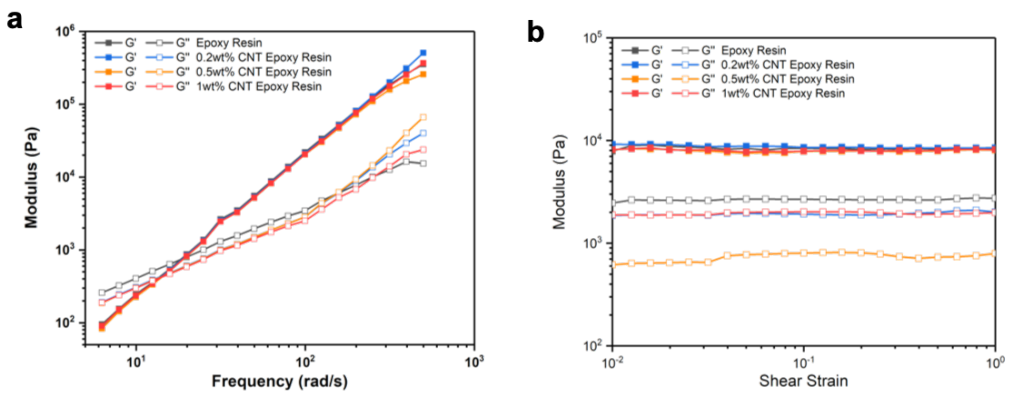

Figure 3.33 a, Effect of CNT filler concentration with the different frequency (G', storage modulus, G'' loss modulus); b, Effect of CNT filler concentration on Modulus at the different shear strain.

3.3.5 Printing Demonstration

The aforementioned epoxy resin-based inks containing I-Al/I-TI initiating system are loaded in the cartridge and placed in the printhead with a pneumatic pressure source. The print-bed temperature can be heated up to 150 °C. When the viscous resin fluid was extruded out of the nozzle and placed on the print-bed, the frontal reaction starts within a few seconds. The printed structure remains its shape when curing starts instantaneously after extrusion and can be frontally cured into many possible shapes via FCDIW, including free-standing structures which is hard to be achieved for conventional additive manufacturing. Also, typical usage of a support structure for thermoplastics additive manufacturing is not compatible with direct ink writing (DIW) of thermosets. We demonstrated the successful printing of a free-standing structure, a spiral, with carefully selected process parameters (Figure 3.34a). A clear propagating front with resins transforming from liquid to solid. A matching print-head speed to V_f is crucial for FCDIW

to keep a continuous propagating front. Other structures are also printed either on the substrate (Texas A&M University logo: ATM) (Figure 3.34b) or in free-space (Capital letter A: Figure 3.34c). The logo and the letter are completed in a single run in minutes. Figure 3.34d is a free-standing spiral structure printed in CNT incorporated epoxy resin inks.

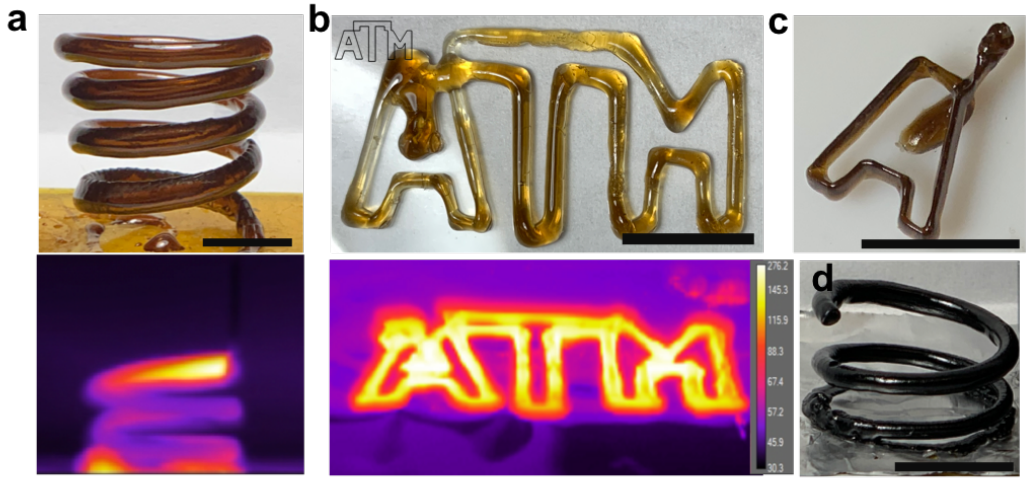

Figure 3.34 FCDIW of epoxy and discontinuous filler composites. a, FCDIW of neat epoxy resin. Inset is the IR heat map indicating processing temperature. b, print and in-situ cure of ATM (logo of Texas A&M University) on a flat substrate. Inset is the designed pattern. Below a, b are the corresponding IR images. c, neat epoxy resin FCDIW of a free-standing letter 'A'. d, free-form printed of the spiral with CNT incorporated epoxy resin.

Size of the printhead, extrusion pressure, and print-bed temperature are the adjustable process parameters for DIW. The size of the printhead and extrusion pressure both control the material feeding rate, and the extrusion pressure is tuned while the printhead gauge keeps constant to obtain the same shear rate in the extrusion process. Besides the material feeding rate, the surface area-to-volume ratio is also altered along with the strand diameter. In general, higher extrusion pressure resulted in increasing

material volume and strand diameter and further affecting the front behavior as well as the outlook of the printed part. Printing with the same ink compositions, the color of the printed parts gradually turns yellow with the decreasing pressure with a decreased V_f and T_f (Figure 3.35). In FCDIW, extrusion pressure has an impact on thermal diffusion, and thermal diffusion together with exothermicity affects front behavior. Tough thermal diffusion and exothermicity have a contradictive effect on front behavior; thermal diffusion starts to dominate when surface-area-to-volume ratio reaches 2.75, exhibiting lower V_f and T_f (Figure 3.35). In DIW printing, increased extrusion pressure will result in higher filament diameter, thus, yielding a lower surface-area-to-volume ratio. For FCDIW, there is a suitable range of surface-area-to-volume ratio from 2.75 to 3.35, which can be reached with a 5-7 psi printing with inks keeps at room temperature in the cartridge.

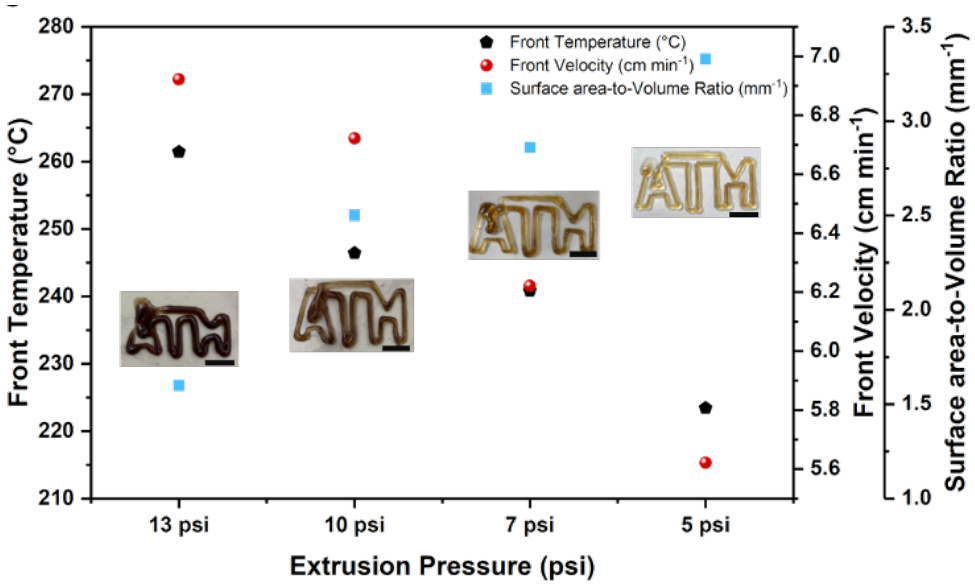

Figure 3.35 Extrusion pressure effect on V_f and T_f. Insets are the image of printed parts under the corresponding extrusion pressure. Surface area-to-volume ratio was calculated based on the measured strand diameter.

Another parameter, print-bed temperature, is also adjusted in the range of 100 °C to 150°C, where only slight differences were observed for front propagation behavior (Figure 3.36).

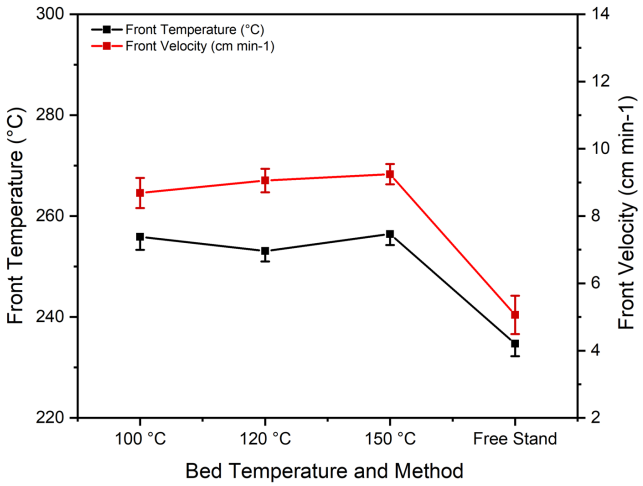

Figure 3.36 Activation temperature effect on front temperature and front velocity.

3.3.6 Mechanical performance

The original strain stress curves corresponding to the specimens fabricated in each category are shown in Figure 3.37. The printed epoxy parts using the current initiating system exhibit a tensile strength of ~ 42 MPa, slightly lower (~17 %) than the oven cured specimens but ~18% higher than the frontally cured specimens.

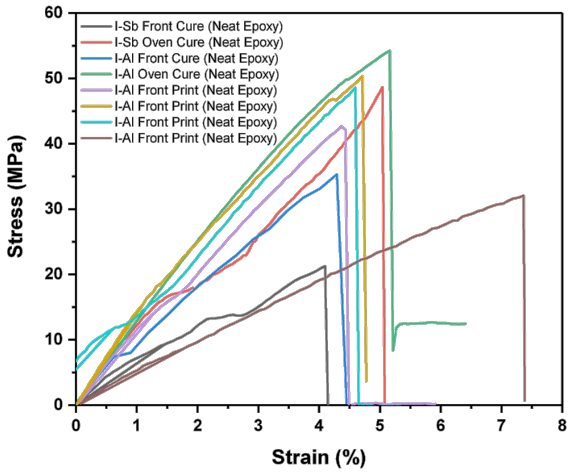

Figure 3.37 Strain stress curve of test specimens fabricated by different methods: Conventional oven cured, RICFC frontal cured neat epoxy (with either I-Sb or I-Al as cationic initiator); FCDIW fabricated neat epoxy, d-filler incorporated epoxy, and d-filler incorporated epoxy/c-CFRC

FCDIW printed specimens showed a ~98% degree of cure indicating that enough exothermicity was provided and complete crosslinkage of epoxy resins was formed during the FCDIW process (Figure 3.38 and Table 3.3).

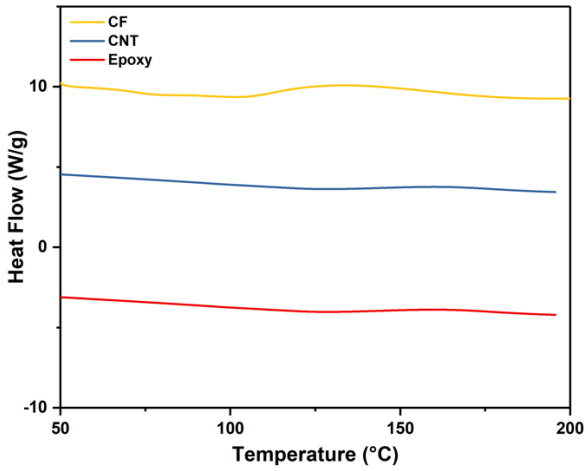

Figure 3.38 Comparison of the heat flow curves of different resin formulation

Bulk frontally cured specimens exhibited a slightly lower degree of cure compared to FCDIW produced parts, which correlates with their mechanical properties.

Table 3.3 Epoxy degree of cure under different manufacturing process

Manufacturing process	Degree of cure (%)
FCAAM cured epoxy	98.1 ± 2.8
Conventional oven cured I-TI/I-Al BPA-epoxy	98.3 ± 1.9
FCAAM continuous CFRC	85.4 ± 1.2
Frontal cured pDCPD CFRC	80.5 ± 3.9[38]
Conventional oven cured pDCPD continuous CFRC	89.6 ± 1.3[38]
Conventional oven cured amine-based BPA-epoxy continuous CFRC	98.7 ± 1.7[38]

The mechanical properties of parts printed by varying ink compositions were tested and compared (Figure 3.39). With 4mol% I-TI/ 0.05mol% I-Al initiator concentrations, the printed specimens exhibited the highest tensile properties. Generally, lower initiator concentrations presented higher mechanical properties due to the effective moderation over the T_f. The incorporation of discontinuous filler in epoxy resins strengthens the tensile properties. When increasing the CNT ratio to 1wt% the tensile strength and Young's modulus improves to ~51 MPa and ~1.4 GPa respectively (Figure 3.39).

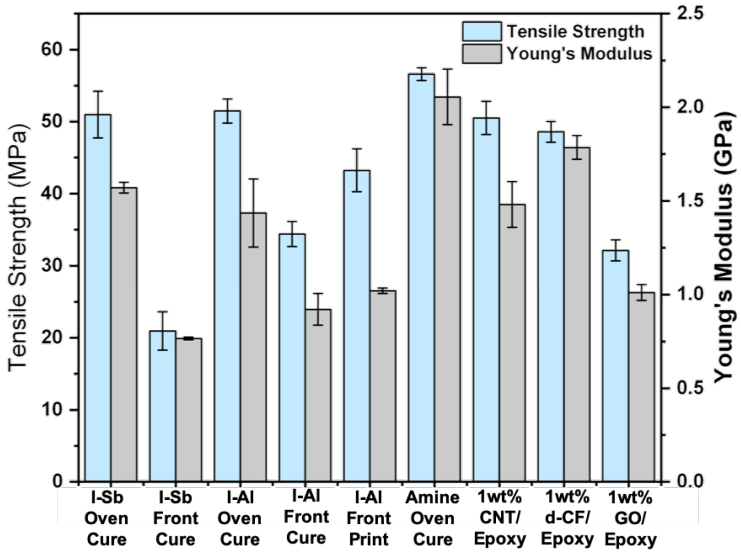

Figure 3.39 Tensile strength and Young's modulus of test specimens fabricated by different methods: Conventional oven cured, RICFC frontal cured neat epoxy (with either I-Sb or I-Al as cationic initiator); FCDIW fabricated neat epoxy, d-filler incorporated epoxy, and d-filler incorporated epoxy/c-CFRC

However, toughness did not increase with the CNT incorporation due to the reduction in strain (Figure 3.40). The 1wt% GO and CF loaded specimens exhibited a tensile strength of 48 MPa and 31.5MPa, lower than the CNT incorporated one.

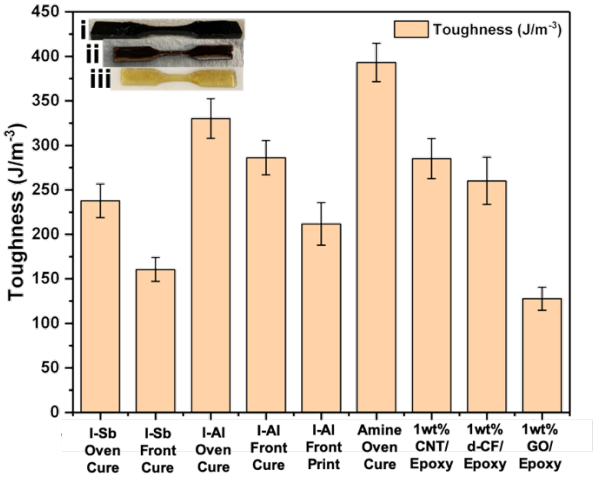

Figure 3.40 Toughness. Inset: i, frontal cured I-Sb/I-TI; ii, frontal cured I-Al/I-TI; iii, printed.

The printed CNT incorporated tensile bars were shown in Figure 3.41. The CNT concentration effect on the tensile performance is shown in Figure 3.42 and Figure 3.43.

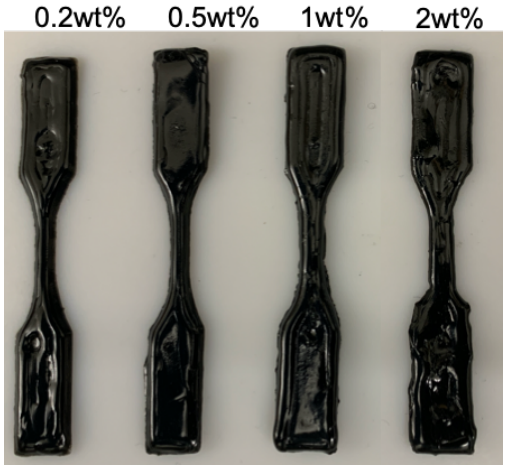

Figure 3.41 Printed CNT/epoxy resin specimens with different CNT concentrations

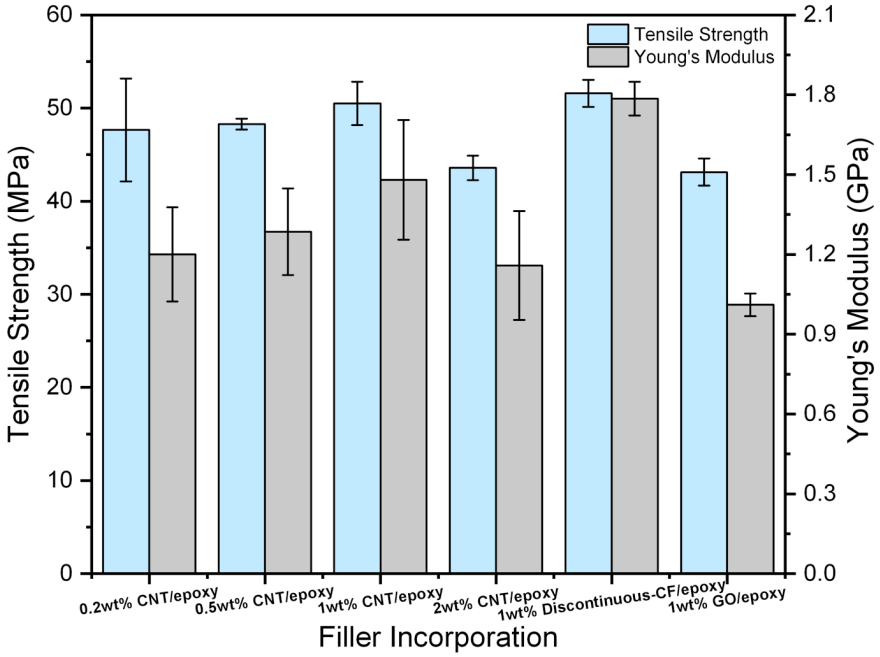

Figure 3.42 Tensile strength and Young's Modulus of printed CNT/epoxy resin with varying CNT concentration, filler types (I-TI: I-Al initiator concentration: 4mol%: 0.05mol%)

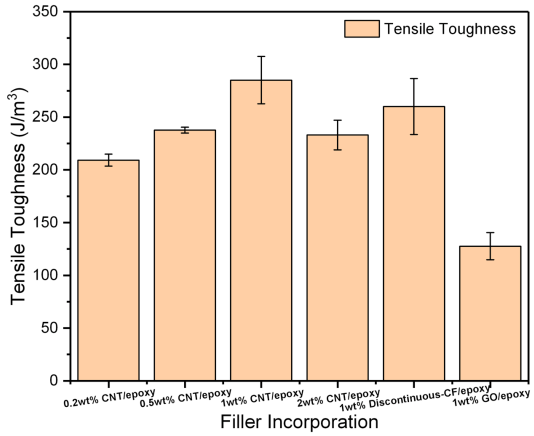

Figure 3.43 Tensile toughness of printed CNT/epoxy resin with varying CNT concentration, filler types (I-TI: I-Al initiator concentration: 4mol%: 0.05mol%)

In comparison to previous reported tensile properties of 3D printed thermosets and discontinuous carbon-filler incorporated composites, our results showed comparable tensile properties with a simplified manufacturing process (Figure 3.44 and Table 3.4). The fractured surface of printed tensile specimens underwent interlayer delamination characterization.

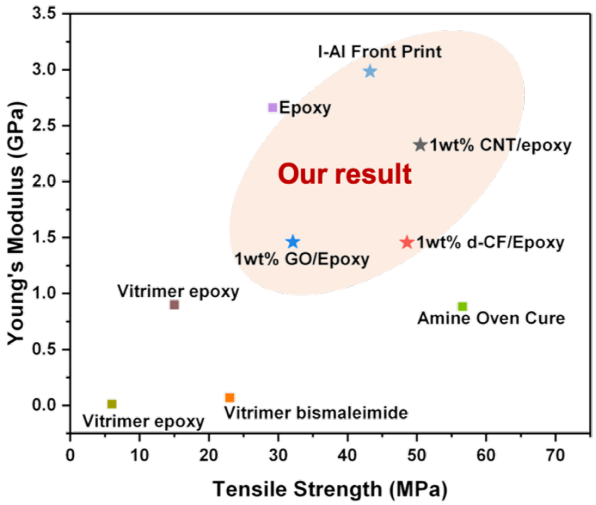

Figure 3.44 Comparison of FCDIW printed specimens with other 3D printed epoxy[157-160] (our results are label as star symbol while others' results are labeled in square symbol).

Table 3.4 Comparison among state-of-art printed epoxy, epoxy-based discontinuous fiber composites

	Material	Tensile strength (MPa)	Modulus (GPa)	Reference
DIW	Epoxy	29.2 ± 4.8	2.66 ± 0.17	[161]
DIW	Epoxy/SiC	69.8 ± 2.9	16.10 ± 0.03	[161]
DIW	Epoxy/SiC/C	43.9 ± 4.1	24.5 ± 0.83	[161]
SLA	Vitrimer epoxy	15	0.9	[157]
DIW	Vitrimer epoxy	6	0.01225	[158]
DIW	Vitrimer bismaleimide	23 ± 3	0.07	[159]
DIW	Acrylate/epoxy	29	0.82	[160]

3.3.7 Continuous carbon fiber printing

Enabled by the superior manufacturability, the frontal curable and printable inks provide a facile and energy-efficient route for continuous carbon fiber reinforced composites fabrication (c-CFRCs). Here, the process illustration of FCDIW c-CFRCs is shown in Figure 3.45a. In this process, frontal curable inks were coated onto the continuous carbon fiber tow through continuous wetting CF in the resin reservoir. The coated epoxy inks helped to condense the flexible fiber tow in the desired shapes and structures. The printed demonstration is shown in Figure 3.45b. The resin volume was tuned by using a printhead with different gauges as well as the co-axial printhead (Figure 3.45c-d). The experiment setup of single/ dual nozzle printing is shown in Figure 3.46a, b, respectively.

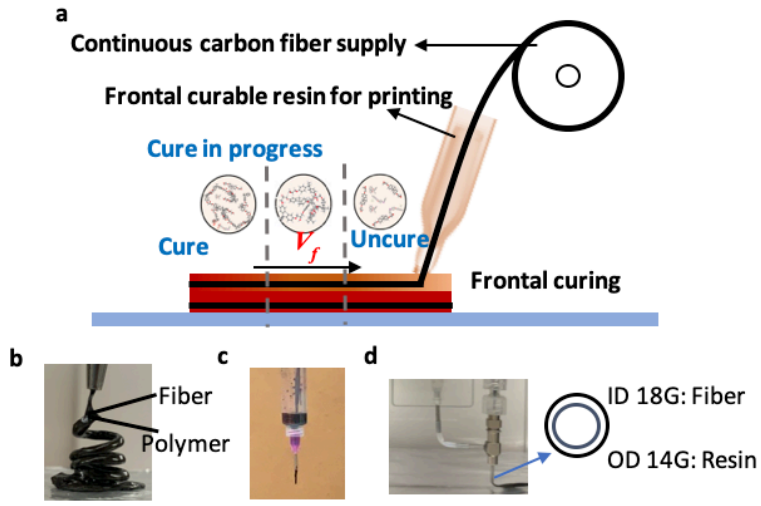

Figure 3.45 Concept and set up for c-CFRC FCAAM. d, demonstration of FCAAM based continuous CFRC fabrication. e-g, continuous fiber printing using both the coaxial and single nozzle.

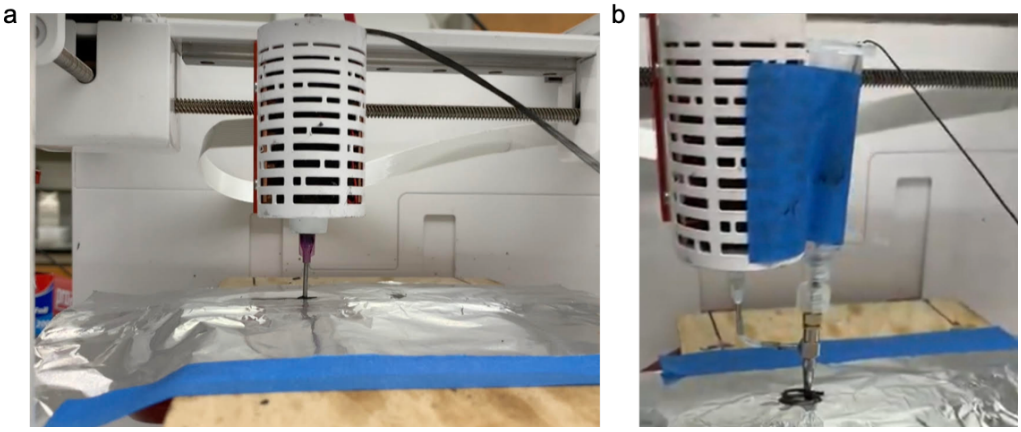

Figure 3.46 Experiment setup for c-CFRC. a, single nozzle printing. b, dual nozzle printing.

The front propagation is analyzed via IR, as illustrated in Figure 3.47. With the inclusion of highly thermal conductive fiber tows, thermal diffusion in propagation direction resulted in a higher front velocity.

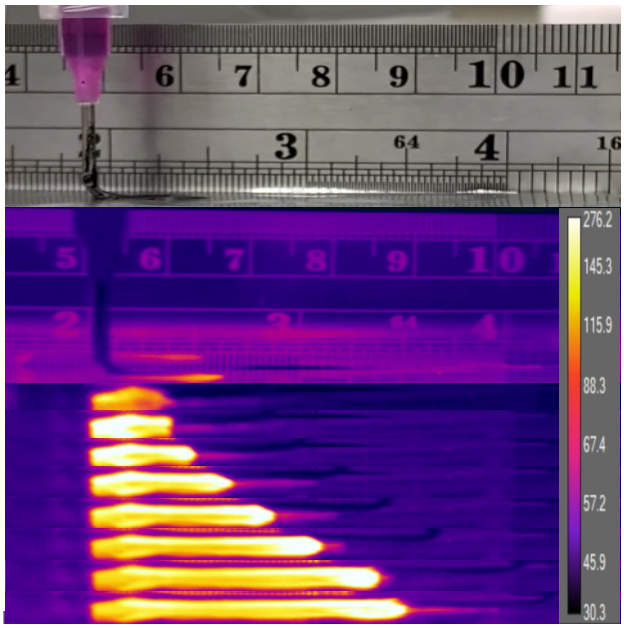

Figure 3.47 Front behavior study via IR image analysis

Still, high exothermicity and rate of reaction of the ink help to minimize the resin volume for high fiber volume fraction and exceptional mechanical performance. Thus, slightly higher initiator concentrations (4mol% I-TI/ 0.08mol% I-Al) were used for c-CFRCs fabrication. The V_f and T_f of c-CFRCs were analyzed using the same method for neat resins. With the inclusion of highly thermal conductive fiber tows, thermal diffusion along the fiber direction is improved. This helps increase the temperature and preheat the resins ahead of the frontal reaction zone, thus, resulted in a higher V_f. Here, printheads with 800 um diameter (18 gauge) and 1630 um diameter (14 gauge) were used for frontal curing enabled c-CFRC printing and the printed parts with the fiber volume ratio of 48 and 18, respectively. For the parts printed with 18vol% in fiber, a higher volume of ink coated on the fiber tow yields higher V_f and T_f, because more reactants help to provide

more thermal energy to sustain the reaction, this also causes a slight temperature increase, as shown in Figure 3.48. With the inclusion of highly thermal conductive fiber tows, thermal diffusion in propagation direction resulted in the front velocity of ~ 7.5 cm/min (48vol% in fiber) and ~13.8 cm/min (18vol% in fiber), both higher than the neat resins printing (~6.2 cm/min) with the same initiator concentration in the same propagation direction (Figure 3.48).

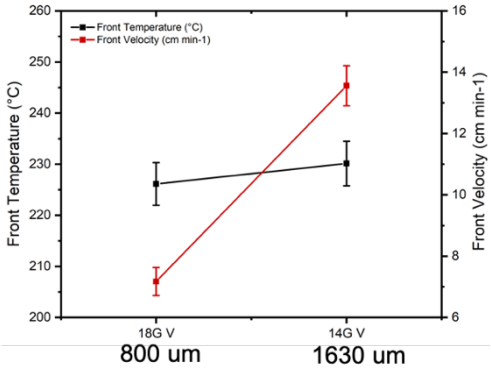

Figure 3.48 Front velocity and front temperature of printing with varying resin volume

Numerical simulation was also conducted to explore the function of continuous carbon fiber tows in thermal transport of epoxy resin frontal reaction. The results are demonstrated in Figure 3.49. A sharp temperature gradient was observed due to the large mismatch in thermal conductivities between the carbon-fiber tow and the resin, indicating a more effective thermal transport along and near the continuous fiber surface. And this results in a higher propagation rate for the c-CFRC printing.

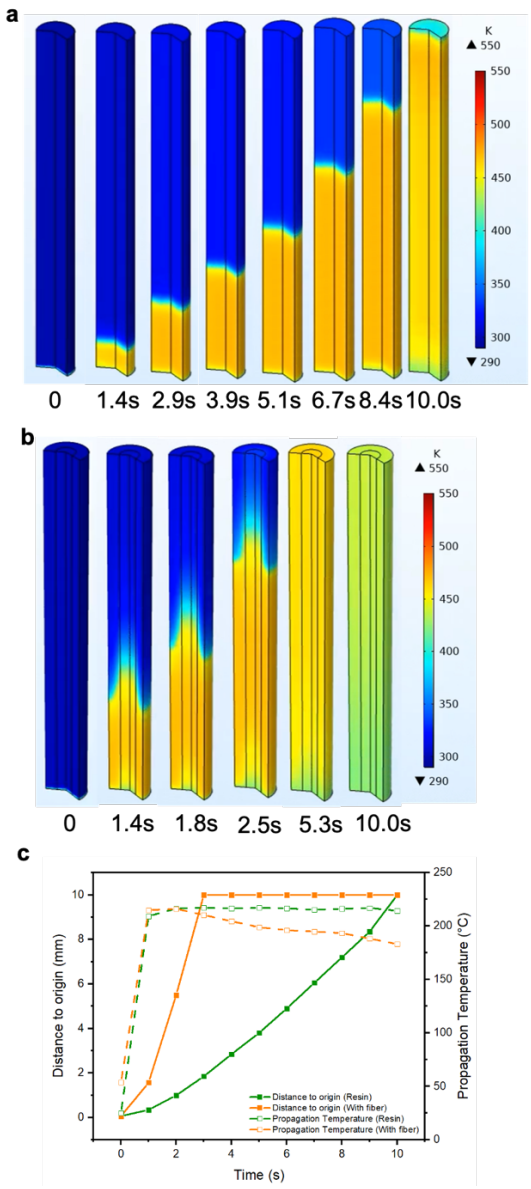

Figure 3.49 Simulation of FCDIW. a, c-CFRC (0.5mm diameter fiber rod, 1.12mm total diameter, length 10mm) and b, neat resin (1mm diameter rod, length 10mm); c, summarized front propagation velocity and temperature of a and b. Orange: c-CFRC Green: neat resin. The resins volume kept same for a and b. The resin's reaction profile used experimental data with I-TI and I-Al concentration of 4mol%: 0.05mol%.

Thus, in c-CFRCs FCDIW process, the front behaviors (V_f and T_f) can be controlled by adjusting the resin volume, print direction, and platform conditions. This shows the promise of constructing parts with complex geometry. Free-standing spiral, honeycomb, star, and multilayer cuboids are printed within a few minutes, as shown in Figure 3.50.

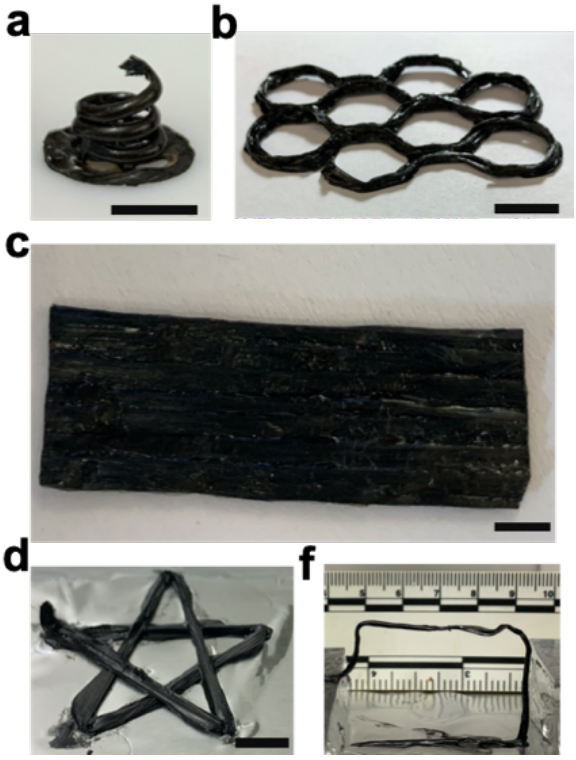

Figure 3.50 c-CFRC printing demonstration. a, printed spiral structure of continuous carbon fiber composites with neat epoxy coating in free space. b, printed multi-layer honeycomb structure of CNT/epoxy/c-CFRCs. c, printed multi-layer CNT/epoxy/c-CFRCs cuboid. d, printed star structure of c-CFRCs with CNT/epoxy coating on a flat substrate. e, free-standing structure print in different orientations.

The high exothermicity and rate of reaction of the ink help to minimize the resin volume for high fiber volume fraction and exceptional mechanical performance. The tensile properties of as-printed c-CFRCs parts demonstrate exceptional tensile

performance that is comparable to or even exceeds other 3D printed c-CFRC, reaching a tensile strength of ~1,147 MPa for printed parts (Figure 3.51). The continuous fiber tow impregnated with reactive resins was applied to ensure a stronger intermolecular crosslinking. Fiber volume plays an important role in increasing tensile strength. When fiber volume increased from 18% to 48%, the tensile strength increased from ~420 MPa to ~1.147 MPa.

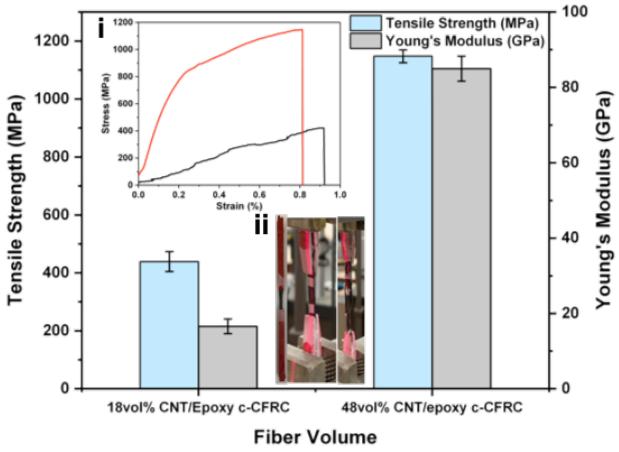

Figure 3.51 Tensile strength and Young's modulus of CNT/epoxy/c-CFRC with varied fiber volume. Insets are the printed c-CFRC specimens for tensile test and the specimen loaded for tensile testing with a laser extensometer. Inset i, the plot of the original stress-strain curve of c-CFRC tensile bars. ii, demonstration of printed tensile bars and pulling process.

Those methods are directly applied to conventional additive manufacturing techniques, such as fused filament deposition (FFF), direct ink writing (DIW), stereolithography (SLA). Our FCDIW fabricated epoxy-based c-CFRCs, with 18% fiber volume, even show a higher tensile strength to some thermoplastics-based c-CFRCs with much higher fiber volume (34%), as shown in Figure 3.52. Further, the tensile strength of specimens with a higher fiber volume (48%) is superior to the other thermosets-based c-CFRCs with higher fiber volume (51% - 57%) (Figure 3.52 and Table 3.5).

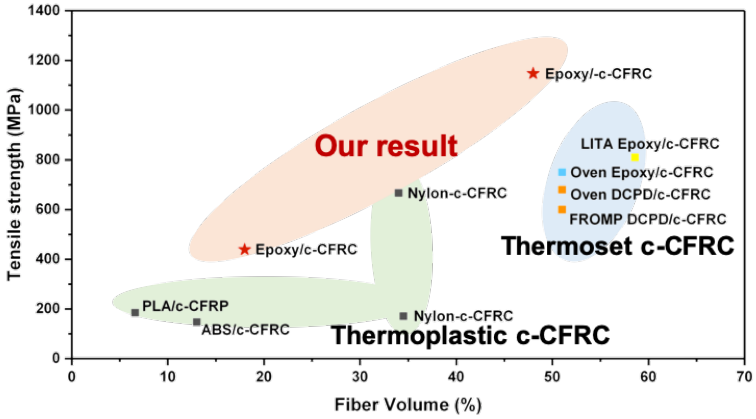

Figure 3.52 Comparison of tensile strength and Young's Modulus of FCDIW fabricated specimens with other representative additive manufacturing methods[31, 38, 92, 94, 96, 162-167] (our results are presented in star symbol and previous reports are noted in square symbol).

Table 3.5 Comparison among state-of-art 3D printed c-CFRCs and unidirectional epoxy composites

Method	Material	Tensile strength (MPa)	Modulus (GPa)	Fiber Volume (%)	Reference
FFF	PLA/c-CFRC	256	20.6	-	94
FFF	Epoxy/c-CFRC	793	161.4	-	96
FFF	PLA/c-CFRP	185	19.5	6.6	162
FFF	Epoxy/c-CFRC	1470	100.28	-	31
FFF	PLA/c-CFRP	155	8.6	-	92
FFF	ABS/c-CFRC	147	4	13	167
FFF	Nylon-c-CFRC	171	-	34.5	166
FFF	Nylon-c-CFRC	667	53.3	34	165
LITA	Epoxy/c-CFRC	810	108	58.6	164
Layup	Oven Epoxy/c-CFRC	750	60	51	38
Layup	FROMP DCPD/c-CFRC	600	55	51	38
Layup	Oven DCPD/c-CFRC	680	56	51	38
FCDIW	Epoxy/c-CFRC	438.82047	34.51481	18	This work
FCDIW	Epoxy/-c-CFRC	1147	84.96032	48	This work
Layup	Unidirectional epoxy composites	2171.85	-	60	31, 163

3.3.8 Energy consumption calculation

Oven curing claimed an energy intensity over 10^5 J/cm^3, indicating a great promise for energy-efficient technology advances in polymer and composites production[2, 168]. Such high energy-intensity is mainly caused by the energy intensive oven and its hours of oven curing. Considering the large demand for epoxy resin (market size: nearly USD 10 billion in revenue in 2019[169] compared to DCPD with a market size of USD 0.86 billion[169]), FCDIW showed a much significant total energy reduction in epoxy resin fabrication (Figure 3.53a, Table B3). Energy consumed for parts fabricated with different volume were considered for energy-saving calculation. The red band in Figure 3.53a represents a potential energy saving of printed parts with 50 cm^3 (lower bond) and 2000 cm^3 (upper bond). The dashed lines and red annotations represent the total energy consumption (product of energy intensity and market volume in a year. If FCDIW is applied to epoxy resins and composites fabrication, potentially 1.3×10^{10} MJ/year of energy (3.6 billion kilowatt-hours/year) can be reduced while only 10% of the amount of energy can be reduced for applying FCDIW in DCPD (Figure 3.53a and Table B3). Comparing to the conventional oven curing process, the FCDIW of epoxy resins presents an energy intensity six of magnitude lower for a large piece (2000 cm^3) printing (Figure 3.53b). Besides, specimens printed by FCDIW showed comparable tensile strength to other reported additive manufacturing methods but takes seven orders of magnitude less energy consumption (Figure 3.53b and Table B4-5). This demonstrates the great promise of FCDIW in epoxy resins and composites fabrication.

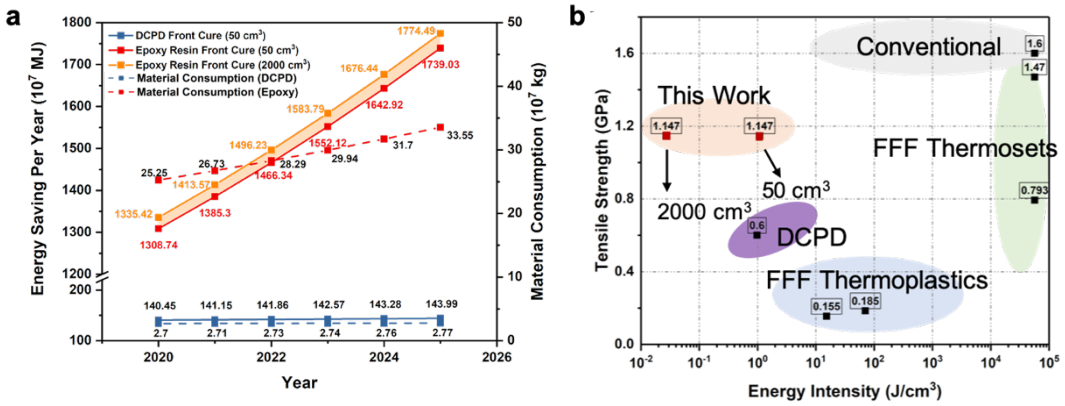

Figure 3.53 Production efficiency calculation and comparison to other reported continuous CFRCs printing methods. a, energy saving and material consumption over the years (2020-2025)[38]. b, Comparison of tensile performance of continuous CFRC versus energy intensity. Frontally cured continuous CFRC exhibited equivalent or higher tensile strength than other reported methods including both thermoplastics and thermosets-based c-CFRC fabrication[2, 31, 92, 96, 162].

3.4 Summary

In summary, rapid and energy-efficient in-situ print-and-cure of aerospace-grade BPA-epoxy based thermosets and composites have been demonstrated via frontal curable epoxy resins. Both the experimental and numerical simulation results demonstrated that the I-TI/I-AI initiator concentration in the range of 2mol%-6mol%/ 0.05mol%-0.08mol% (except for 2mol%/0.05mol%) is suitable for FCDIW. Further, the introduction of thermally conductive fillers facilitates the frontal curing process. The addition of 1wt% CNT effectively lowered T_f by ~4.4% while maintaining sufficient V_f. Further lowering the T_f can reduce the polymer degradation during the frontal curing process. Besides, the proposed inks were used for FCDIW of c-CFRCs with a high level of flexibility. The FCDIW printed c-CFRCs exhibited a tensile strength of ~1.147 GPa, far exceeding the 3D printed thermoplastic based c-CFRCs and is comparable to other thermosets-based c-

CFRCs. The as-printed c-CFRCs met the requirements for high-performance applications and showed great promise in producing parts for industrial applications. Notably, the energy-efficient FCDIW method could reduce 3.6 billion kilowatt-hours/year of energy for the epoxy resin and composites market. The current study popularizes the FPAM to a more commonly used material. The successful demonstration of FCDIW epoxy and composites makes the realization of autonomous production foreseeable and could revolutionize the epoxy production industry.

CHAPTER IV

ENHANCING INTERLAYER BONDING OF 3D PRINTED DICYCLOPENTADIENE VIA FRONTL POLYMERIZATION

4.1 Introduction

Thermosetting polymers are well known to be mechanically robust and capable of withstanding high service temperature for extended periods that outweighed the state-of-the-art thermoplastics. But 3D printed parts are less mechanically strong compared to conventional molded parts because of the layer-by-layer fashion of constructing the 3D object. Thus, improving the overall mechanical performance to match the conventional molded parts is the target for 3D printing.

Many efforts are made to improve the mechanical performance of printed parts. Sweeney et al. coated a thin layer of carbon nanotube onto their polylactic acid (PLA) filament and applied intense localized heating for polymer diffusion to increase the interlayer bonding (as shown in Figure 4.1a), thus improving the overall fractural strength by ~4 times[170]. The comparison of mechanical performance of 3D printed bulk manufactured parts and localized heating enhanced printed parts is shown in Figure 4.1b. Kuang et al. introduce a secondary thermal induced polymer network to the first photocured network to enhance the mechanical performance (as shown in Figure 4.2a)[71]. Zhang et al. and et al. introduced the dynamic covalent bond to the polymer network which will form the covalent bond across adjacent layers after heat treatment to strengthen the printed parts(as shown in Figure 4.2b-c)[171]. Besides, filler incorporation is known to be an

effective way to enhance the mechanical performance of manufactured parts, especially improving the tensile strength as well as the modulus[172]. Nanofillers (such as CNT[173]) and microfillers (such as CF[174]) were incorporated to modify the polymer matrix properties. Despite their superior properties, the interfacial bonding between fillers and the polymer matrix affects the overall performance of the composites. Surface modification is an effective way of improving the filler-matrix interface. Various functional groups including carboxyl[175], hydroxyl[176], and amine[177] were decorated onto the filler surface. After surface modification, the filler dispersion and interaction between fillers and matrix were improved.

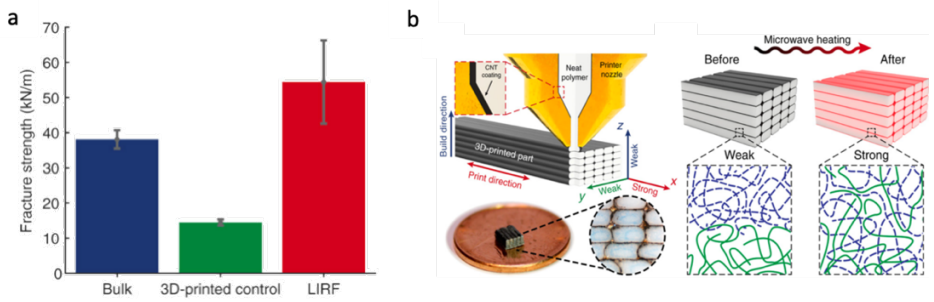

Figure 4.1 Weakened strength for polymer extrusion-based 3D printing reprinted with permission from[170]. (a) Fracture strength comparison between bulk, regular 3D printed specimens and localized heating enhanced 3D printed parts; (b) Schematic illustration of localized heating enhanced 3D printed polymers.

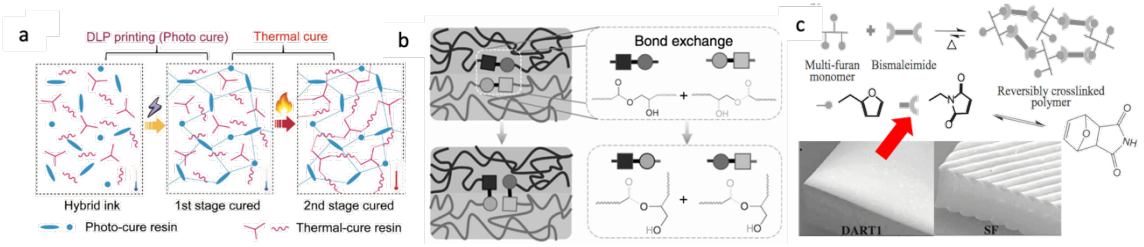

Figure 4.2 Previous attempts of enhancing interlayer bonding strength of 3D printed specimens. (a) two-step curing: photo cure and thermal cure, reprinted with permission from [71]; (b, c) Dynamic covalent bonds, reprinted with permission from[69, 171].

In this chapter, we innovatively modified the discontinuous CFs surface chemistry with norbornene functional groups grafted to realize the in-situ frontal polymerization and filler-matrix interaction enhancement simultaneously. With the incorporation of norbornene functional groups modified CFs in the DCPD monomer matrix, their rheological behavior, printing process and printed part performance were monitored. The filler-matrix interaction was furthered proved by the interlayer bonding strength measurements.

4.2 Experiment

4.2.1 Surface modification of carbon fiber (CF)

As-designed carbon fiber decorated with norbornene functional group for in-situ polymerization will be synthesized in the following sequence: carboxyl groups, acyl chlorides with subsequent grafting of triol groups and norbornene group grafting via esterification. The schematic illustration of the modification process was shown in Figure 4.3. Specifically, the raw carbon fibers (100 mg) were treated in 100 mL acetone at 80 °C in an oil bath and refluxed for 48 hours to remove sizing on the surface of the carbon fiber. De-sized carbon fibers were then treated with HNO3 (67%, 100 mL) and bath sonicated for 15 min for initial dispersion with subsequent reflux at 100 °C for 6 hours to prepare carboxyl functionalized carbon fibers. The treated carbon fibers were washed with deionized (DI) water to remove the residual acid and dried in a vacuum oven. Then, an excess amount of thionyl chloride was treated with carboxy functionalized carbon fibers with a catalytic amount of N, N'-Dimethylformamide (DMF) to form acyl chloride. The synthesis was operated using a Schlenk line under N_2 protection at 70 °C for 48 hours.

Later thionyl chloride was removed. Pentaerythritol (1.14g) and tetrahydrofuran (THF) were treated with the acyl chloride for 36 hours at 70°C and washed with 300 mL dichloromethane (DCM) and 100 mL THF alternatively to remove the residual chemicals. The products were dried under vacuum. The 5-norbornene-2-carboxylic acid (6.0 mL) was mixed with an excess amount of thionyl chloride in a flask and stirred under N_2 protection for 24 hours, as shown in Figure 4.4a. After the removal of thionyl chloride, the triol-functionalized carbon fibers were added with the addition of DCM, anhydrous DMF and triethylamine, as shown in Figure 4.4b. The acyl substitution was proceeded under N_2 protection for another 48 hours at 50 °C and washed with 300 mL dichloromethane (DCM) and 100 mL THF alternatively to remove the residual chemicals. Figure 4.4c shows the Schlenk set up used in the synthesis.

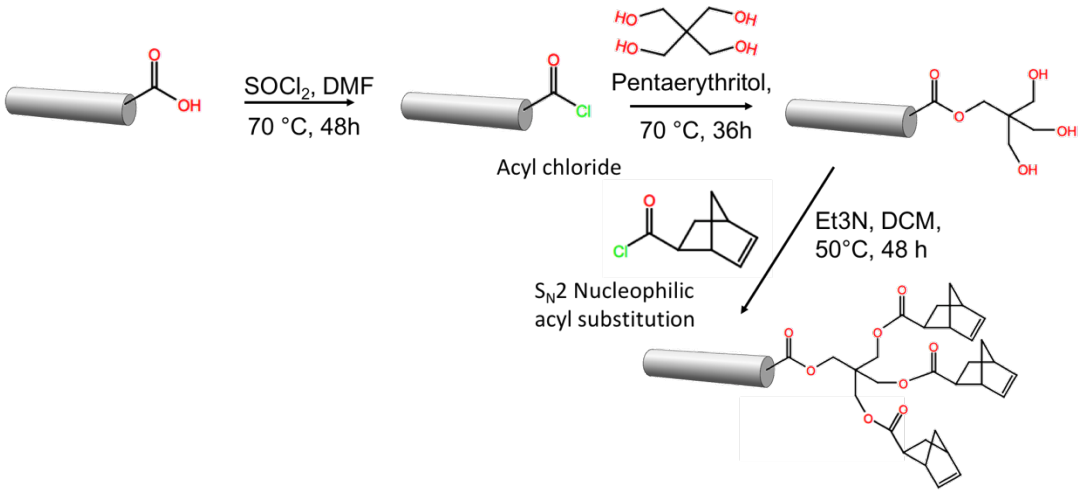

Figure 4.3 Schematic illustration of norbornene functionalized carbon fiber

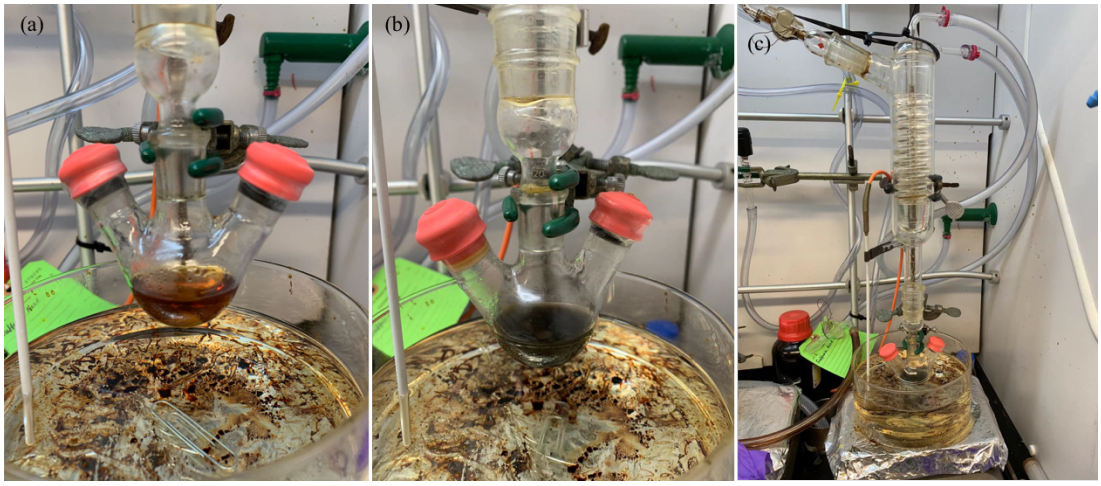

Figure 4.4 Carbon fiber surface modification process. (a) Norborne group modification. (a) preparation of 5-norbornene-2-carboxylic acyl chloride; (b) addition of triol-functionalized carbon fiber for esterification; (c) Schlenk setup for anhydrous and N2 protected reaction.

4.2.2 Frontal curable and printable DCPD ink preparation

The frontal curable and printable DCPD ink was prepared following Robertson et al.'s procedure with modifications[38]. Specifically, to reduce the melting point of DCPD solution to under room temperature, 5wt% 5-ethylidene-2-norbornene (ENB) was added to Dicyclopentadiene (DCPD) at 40°C. Second-generation Grubbs' catalyst (GC2) was dissolved in phenylcyclohexane (PC) to obtain a 1wt% GC2 solution. The inhibitor, triethyl phosphite (TEP), was added to PC to obtain a 10 vol% TEP solution. The ink was prepared by adding 6.4 µl TEP solution, 341 µl GC2 solution into 5g DCPD solution. So the molar ratio of the ink is 10000:1:1 for DCPD, GC2, and TEP respectively. The mixture was degassed and stored at room temperature for 2 hours.

For carbon fiber incorporated DCPD inks, the fiber (functionalized and unfunctionalized) was incorporated in the ENB and DCPD mixtures via vigorous stirring followed by ultrasonication before any addition of catalyst and inhibitor.

4.2.3 Printing process

The geometric model of CF composites was prepared and converted to g-code. The same direct ink writing based 3D printer, Allevi 1 was used in this study with a build volume of 90 × 60 × 130 mm. Also, thermocouples were added as a heat source for reaction activation. 18-gauge needles were selected, and the printing speed is set to 2 mm/s. The printer has a printing accuracy of 7.5 um in the X-, Y-axis, and 1 um on Z-axis. The printer can be auto-calibrated every time before the print job starts. The extruder head can hold a 5 ml cartridge and caped with a pneumatic pipeline. The extrusion pressure can be adjusted by tuning the pneumatic flow. Prepared ink is loaded in the extruder and forced out of the nozzle via pneumatic force. thermocouple underneath the glass substrate is set to 85 °C to activate the polymerization. The printer, printing process, and printed specimens with different geometries were demonstrated in Figure 4.5.

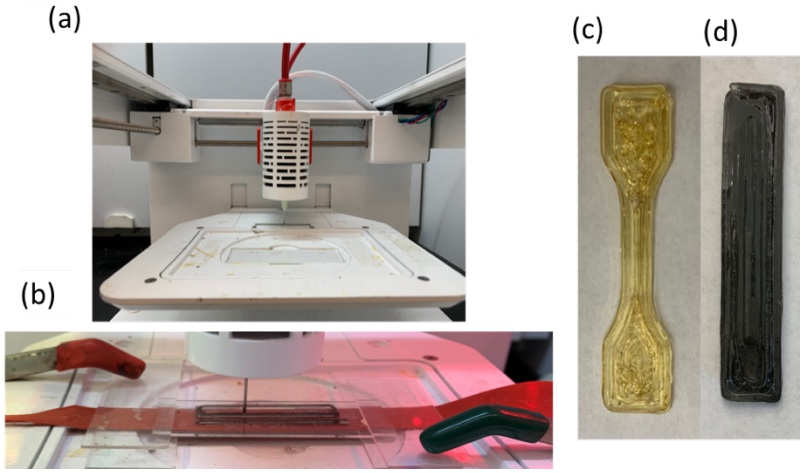

Figure 4.5 Extrusion based printer setup and pure resin/carbon fiber composites printing demonstration; (a) printer set up (commercially available printer Allevi 1); (b) carbon fiber composites printing demonstration, thermocouple (red belt beneath the glass substrate) used as the initial heat supply for polymerization initiation; (c) printed virgin PDCPD tensile bar; (d) printed carbon fiber composites cuboid.

4.2.4 Rheological behavior and cure kinetics study

The rheological behavior of DCPD and CF/DCPD inks was measured via the Anton Paar Physica MCR-301 rheometer. The viscosities and shear stress were measured using 50mm CP 50-1 plate geometry. The DCPD and CF/DCPD inks were stored at room temperature/ ice bath for different period before measurements.

Cure kinetics of DCPD and CF/DCPD with different CF filler concentrations were tested using Differential Scanning Calorimeter (DSC, Q20 TA Instruments).

4.2.5 Mechanical measurement

Tensile bars were prepared followed by the same procedure described in Section 3.2.6.1. The tensile specimen was designed according to the ASME D638-type V standard model. The tensile test was performed on an Instron tensile machine. The tensile test speed was set to 10 mm min^{-1}. Ultimate tensile strength, Young's modulus, and elongation at break were calculated using the strain-stress curve.

Another batch of specimens was prepared following ASTM D3163 standard with a modified dimension for the interfacial shear test. The modified specimen has a dimension of 10mm on each side and 5mm for the interfacial area. The test speed was set to 6 mm min^{-1}. Interfacial shear strength was determined by the maximum loading force per unit interfacial area.

All specimens were tested directly after printing without any post-treatment.

4.3 Characterization and results

4.3.1 CF surface modification

The norbornene functionalization of carbon fiber was subject to Fourier-transform infrared spectroscopy (FTIR) analysis. The spectrums of untreated, de-sized, carboxyl functionalized and norbornene functionalized carbon fiber are shown in Figure 4.6. In the spectrum of carboxyl grafted carbon fiber, the broad peak at 3100 to 3700 cm^{-1} corresponds to the -OH stretching of carboxyl groups. The peak at 1690 cm^{-1} is assigned to C=O stretching of carboxyl groups. In contrast, the broad -OH peak disappeared for the norbornene functionalized carbon fiber with the new peak showed at 1540 cm^{-1} which corresponds to C=C bonds for norbornene groups. Besides, the redshift of the C=O bond from 1690 cm^{-1} to 1720 cm^{-1} provides further evidence of the formation of ester.

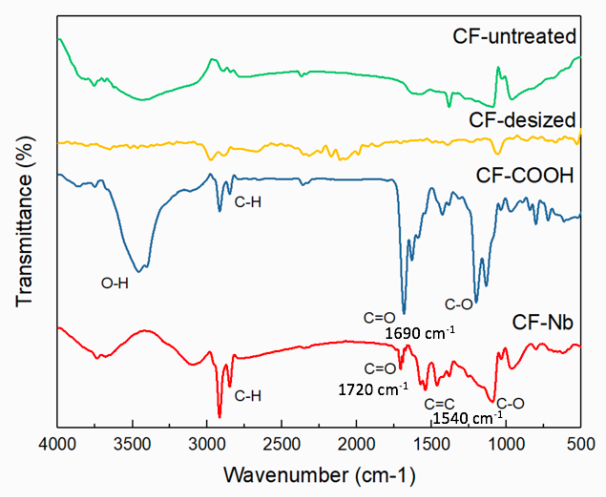

Figure 4.6 FTIR characterization of norbornene functionalized carbon fiber.

4.3.2 Rheology

The rheological behavior of the neat resin and CF-filled resin was measured to determine ink formulation and process parameters for extrusion printing. For DCPD based

frontal polymerizable inks used in this research, their rheological behavior is more complicated. The viscosity changes over time since the polymer chain starts to propagate even at 0 °C due to resin high reactivity with the proposed catalytic system. The viscosity change is due to chain propagation where the increased chain length increases the ink viscosity. Hence, the ramping rate of viscosity over time is dependent on the polymerization kinetics.

To understand and determine the printing windows, the rheological behavior of neat resins was examined, and the results are shown in Figure 4.7. The viscosity of the ink was increased dramatically from 1 mPa s to 800 mPa s in the first 4 hours at room temperature which means the polymerization starts directly after the addition of initiator and inhibitor into the monomer. The reaction can be partially inhibited at lower temperatures proved by the slightly changed viscosity observed for solution stored at 0°C. The viscosity measurement shown in Figure 4.7a indicates the process window for the DCPD solution with the exact amount of catalyst and inhibitor addition. Also, the shear stress and viscosity as a function of shear rate were measured and the profile was shown in Figure 4.7b. The shear thinning behavior was observed for the solution stored at room temperature for 4 hours. For the solution stored at 0°C, it shows the linear relationship between shear stress and shear rate which corresponding to the Newtonian fluid characteristic. Based on the rheological study, the inks were kept at 0°C for 2-4 hours before printing.

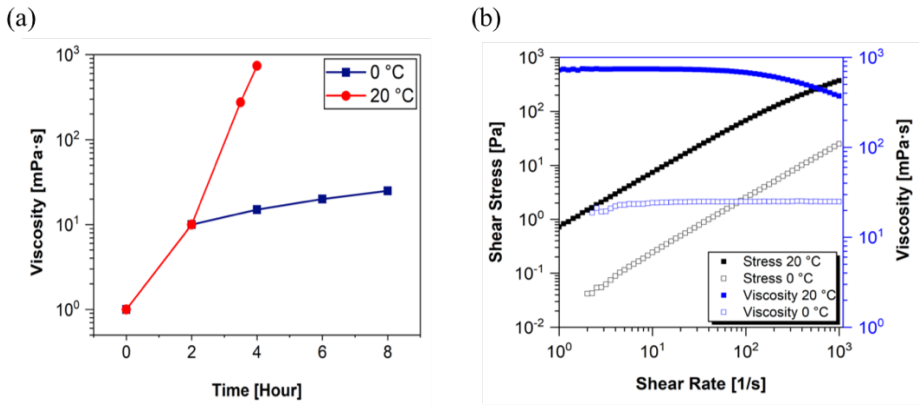

Figure 4.7 Rheological behavior of DCPD. (a) time and temperature effect of DCPD solution; (b) shear rate effect on shear stress and viscosity[178].

The addition of CF increased the composite ink viscosity, as shown in Figure 4.8. A higher CF loading yields a higher ink viscosity. The fiber ratio studied in this research ranges from 0~5wt%. Because of the high aspect ratio of CF, it induced the shear thinning behavior of the ink which compensates for the low viscosity and Newtonian fluid behavior of neat resin and potentially improves the dimensional accuracy for printing. The shear thinning behavior refers to the decreasing viscosity with increasing shear rate and reverts to original viscosity at a low shear rate.

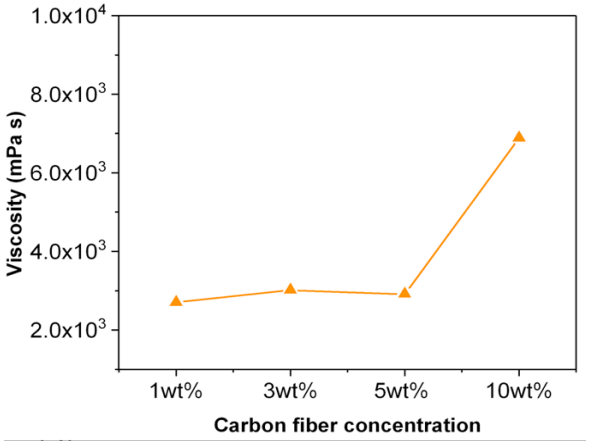

Figure 4.8 Viscosity of CF-incorporated DCPD ink vs. CF-loading concentration

During extrusion printing, when ink flows into the narrow nozzle tip by pneumatic force, the small size nozzle induces large pressure against its flow, so the decreased viscosity could reduce the resistance and facilitate ink flow. When the ink was squeezed out of the nozzle tip, resistant force disappeared and the shear rate was reduced, the viscosity of the ink could recover at the same time. The demonstration of the rheological behavior of composite ink and the comparison with neat resin are shown in Figure 4.9. The grey and red line represent the viscosities at different shear rates for DCPD and 3wt% fiber composites, respectively. The viscosity vs. shear rate curve obeys a power-law model:

$$\eta = K\dot{\gamma}^{n-1}$$

where $\dot{\gamma}$ is the shear rate; K is the consistency index, and n is the power-law index. K represents the value of apparent viscosity of the fluid at a shear rate of 1 s^{-1}, and n indicates the degree of shear thinning behavior[179]. Besides, the shear rate that ink undergoes for different process period: in the cartridge, during printing, and after printing, can be determined via the following model:

$$\dot{\gamma} = \frac{8v}{d}$$

where ν is the printing speed and d is the inside diameter of the cartridge or needle[179]. In this study, the printing speed was 2 and 2.5 mm s^{-1} for neat DCPD and composite ones. The cartridge's inner diameter was 16 mm, and the needle inner diameter was 838 um. The corresponding viscosities at different process periods were calculated and are shown in Figure 4.8. The CF/DCPD fluids demonstrated obvious shear thinning at $\gamma<1s^{-1}$, and then remained at a low viscosity independent of the shear rate.

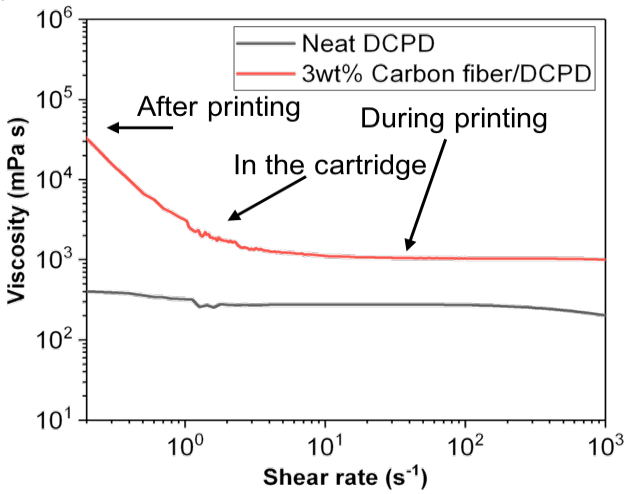

Figure 4.9 Viscosity of neat DCPD and 3wt% CF-incorporated DCPD at different shear rates

4.3.3 Cure kinetics

In addition to the rheological behavior, frontal curable ink also requires high reactivity, which is shown in the Differential Scanning Calorimeter (DSC) curve in Figure 4.10. The grey and red line represent the DSC curve of pure DCPD solution and DCPD solution with the addition of carbon fiber. From the DSC curve, both neat DCPD ink and DCPD composite ink exhibit high reactivity with an enthalpy of ~78.38 J g^{-1} and ~75.54 J g^{-1} calculated by accumulating the area under the curve, respectively. With the addition of carbon fiber, the exothermic peak shifted slightly to a lower temperature which suggests that the formulation become more reactive with the addition of carbon fiber. Also, the exothermic peak slightly shifted to a lower temperature, indicating the formulation becomes more reactive with the addition of CFs. The peak of CF loaded resin was slightly lower than that of neat DCPD because the highly thermal conductive fiber facilitates thermal transport and speeds up the frontal polymerization process.

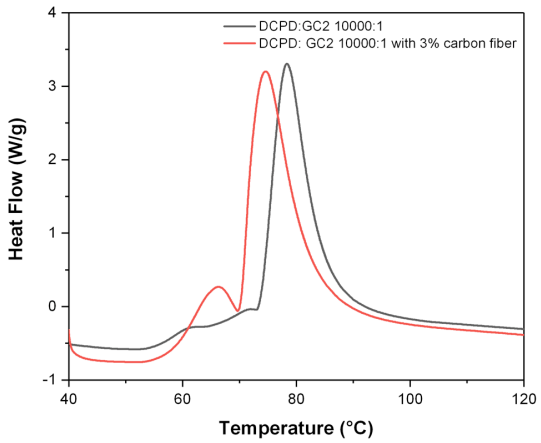

Figure 4.10 Cure kinetics characterization of pure DCPD and DCPD-carbon fiber solution.

4.3.4 Extrusion printing process

3D printing of CF/DCPD composites with in-situ curing was illustrated in Figure 4.11. The printing speed was set to 6mm s^{-1}, and the curing condition was 70°C for less than 10s (for initiation). This process setting was referred to Robertson et al.[38] as they claimed for the optimal process settings for FROMP DCPD. Specifically, the chemical structure of norbornene functional group and monomer structure of the thermosetting polymer matrix is shown in Figure 4.11a. The key concept for improving interlayer adhesion while printing is to introduce the reactive groups onto the fiber surface. During the printing, frontal polymerization occurred spontaneously with the presence of the GCII catalytic system, and polymerization of monomers in the nearby region resulted in highly crosslinked polymer matrix. Some reactive sites from frontal ring-opening metathesis polymerization (FROMP) of highly reactive dicyclopentadiene (DCPD) could leftover and remain active for second crosslinking of olefin addition, as shown in Step 1 of Figure 4.11b. Similarly, when the crosslinked polymer chains approach the reactive norbornene

groups on a fiber surface that contains a similar chemical structure and shares the same ring-opening reaction route with DCPD monomer, it initiates the FROMP reaction and bridges CF to the propagating DCPD chains as shown in Figure 4.11b step 2. As a result, strong covalent bonding between the polymer chain and CFs will be produced[75, 180]. More importantly, since the norbornene group is reacted with the same catalyst of DCPD, the CF/matrix reaction is also happened spontaneously and concurred with the printing process by taking advantage of the heat released from the previous polymerization nearby, resulting in in-situ bridged CF/matrix interfaces[75]. When the fiber sits between two adjacent filament traces, the generated covalent bonds between fiber and polymer matrix could also present at the interlayer, as illustrated in Figure 4.11c, and thus considerably boost the interfacial bonding as shown in Figure 4.11d. The inset drawing (dashed grey box) in Figure 4.11d demonstrates the crosslinkage between fiber and polymer matrix. The crosslinkage not only creates adhesion perpendicular to the printing plane (XY plane) but also provides adhesion between filament traces in the same layer as long as fiber extrudes or presents at the filament boundary. This statement was also confirmed by the optical microscope images of a cross-section of interlayer test specimens (after the test). Tiber-matrix interactions for different fiber surface conditions were shown in Figure C1-2 in appendix C. Further descriptions are also included in Note C1-2.

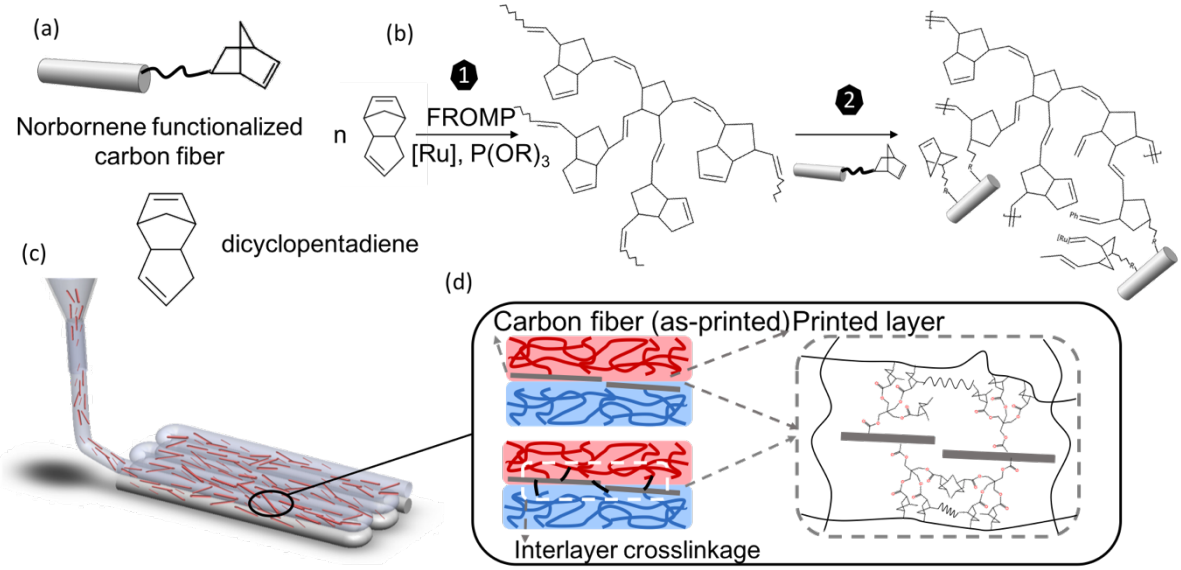

Figure 4.11 Illustration of frontal polymerization-enabled printing and interlayer bonding; (a) chemical structure of grafted norbornene group and monomer dicyclopentadiene used as polymer matrix; (b) Scheme of functionalized CF based self-reinforcement. Step 1: FROMP of poly (DCPD); Step 2: chemical crosslinking of functionalized CF to poly (DCPD) matrix; (c), (d) Schematic illustration of functionalized CF reinforcement through in-situ Interlayer bonding.

Fiber loading and the large surface to volume ratio of the microscale filler reinforcement provide a large number of reactive sites for crosslinkage, resulting in effective load transferring between CF and matrix. Moreover, the interlayer crosslinkage not only happens between polymer matrix and CFs but also generates secondary crosslinkage of olefin addition, resulting in covalent bonds among polymer matrices across interlayers, as shown in Figure 4.11d. With the assistant of the norbornene functioned fiber, the overall mechanical performance of the 3D printed DCPD carbon fiber composites could be strengthened via frontal polymerization while eliminating post-treatment for energy-efficient, high-performance thermoset composites fabrication.

4.3.5 Tensile properties

For mechanical properties measurements, the effect of CF concentration on tensile strength, tensile modulus of the printed composites was analyzed. Dogbone shaped ASTM D638 Type-V tensile bars were printed following the same ink formulation described in Section 4.2.2 and the printing procedure introduced in Section 4.2.3. Firstly, neat DCPD and CF/DCPD composites with different fiber concentrations were printed and tested, where sized CFs were used as received. The CF concentration was set to 1wt%, 3wt%, and 5wt%. Tensile bars were sealed in two load cells for tensile testing. Sandpaper was used to increase friction. Typical strain-stress curves of printed thermosets and composites specimens are shown in Figure 4.12a. Black, red, blue, and yellow curve represent neat DCPD, 1wt%, 3wt% and 5wt% fiber loading DCPD composites, respectively. The strain was measured by the displacement between grips during the tensile testing corresponding to the original grip distance. The Young's modulus was determined by the slope of the elastic region with a strain rate of 0-2% of the original stress–strain curve. Toughness was obtained by integrating the areas under the original stress-strain curve. With the addition of CF, both tensile strength and breakage elongation were increased considerably, even though only limited amount of fiber was loaded. Both the tensile strength and Young's modulus continuously rise with the increasing weight percent of carbon fiber to 3wt%. However, beyond 3wt%, for 5wt% carbon fiber composites, there was a reduction in tensile strength and breakage elongation due to the fiber aggregation and random orientation. The results of the tensile strength and Young's modulus results of DCPD and CF/DCPD composites were shown in Figure 5b. DCPD loaded with 3wt% CFs exhibited

the highest tensile strength. Compared to neat DCPD, the 3wt%CF/ DCPD composites exhibited an increase of ~88% in tensile strength. For modulus, 3wt%CF/ DCPD composites exhibited an increase of ~44% in modulus where DCPD based composites with 5wt% CFs showed an increase of ~160% in modulus compared to neat DCPD. DCPD with higher CF concentration showed a higher modulus because CF is highly rigid and strong, and it helps to improve the stiffness when further increasing fiber concentration. The inset picture of Figure 4.12b shows printed tensile bars (left) and broken bars after tensile testing (right).

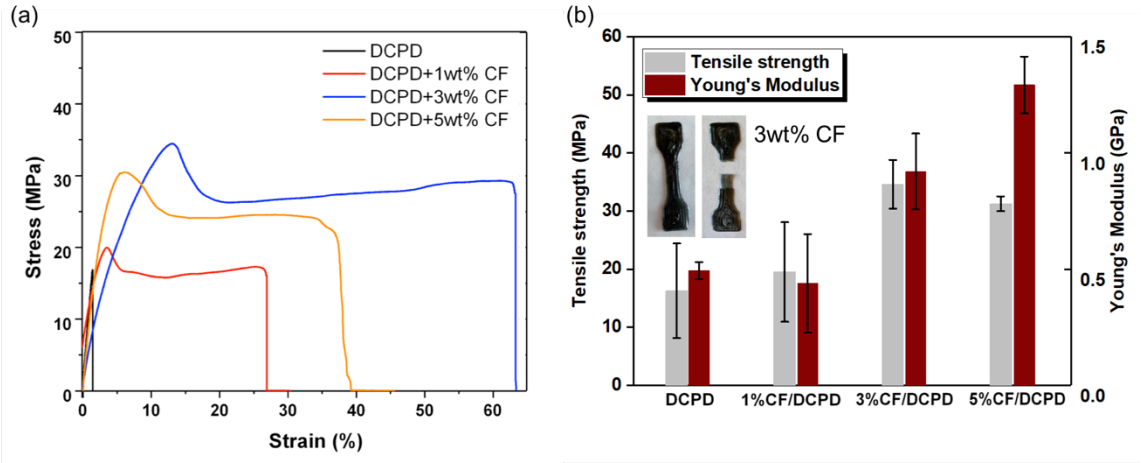

Figure 4.12 Effect of carbon fiber on the mechanical performance of printed composites; (a) original strain-stress curve of neat DCPD and CF/DCPD composites with different loading; (b) comparison of tensile strength and Young's modulus of DCPD and its carbon fiber composites.

According to the results studied above, 3wt% CF loading was selected for further study of the effect of CF surface chemistry on the mechanical properties, as shown in Figure 4.13. The tensile strength of norbornene-CF composites was as high as 43.3MP, demonstrating a 1.7-fold enhancement about the neat resins. As-printed carboxyl-CF/DCPD also demonstrated tensile strength of 37.9 MPa, 1.3-fold enhancement

regarding the neat resin. As-printed sizing-CF/DCPD composites demonstrated tensile strength of 34.6MPa, 1.1-fold enhancement in comparison with neat resin. This is because of the improved fiber/matrix interface with norbornene functionalization and the formation of covalent bonding between fiber and polymer matrix. Sample toughness was calculated by accumulating the areas under the stress-strain curve. The calculated toughness shows similar trends for printed tensile bars, so does fracture strength, also known as breaking strength, as shown in Figure 4.13b.

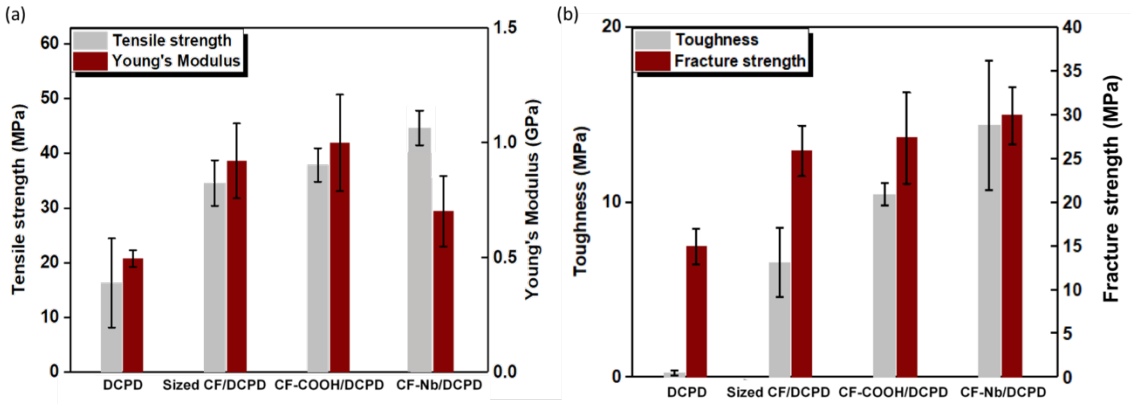

Figure 4.13 Effect of carbon fiber functionalization on the mechanical performance of printed composites; (a) tensile strength and Young's modulus of neat DCPD and DCPD composites with 3wt% loading; (b) toughness and fracture strength of neat DCPD and DCPD composites. The norbornene grafting was represented with CF-Nb.

The less-effective enhancement of Young's modulus for norbornene-CF/DCPD was caused by fiber shortening during multi-step and long-time mechanical agitation and sonication dispersion. Fibers that were subjected to different treatments were analyzed by an optical microscope, and their lengths were measured, as shown in Figure 4.14, Table 4.1, and Figure 4.15. Long fibers were found to be chopped during the intensive mechanical agitation or sonication in the surface modification of norbornene while de-

sizing and oxidation treatments did not affect the fiber length due to mild mechanical agitation. This is consistent with the reported literature that intensive mechanical agitation or sonication could synergistically work with chemical etching to significantly shorten the fiber [181]. In the future work, effective dispersion of fibers with only mild mechanical agitation or further simplifying process steps could avoid considerable fiber shortening while achieving the surface functionalization.

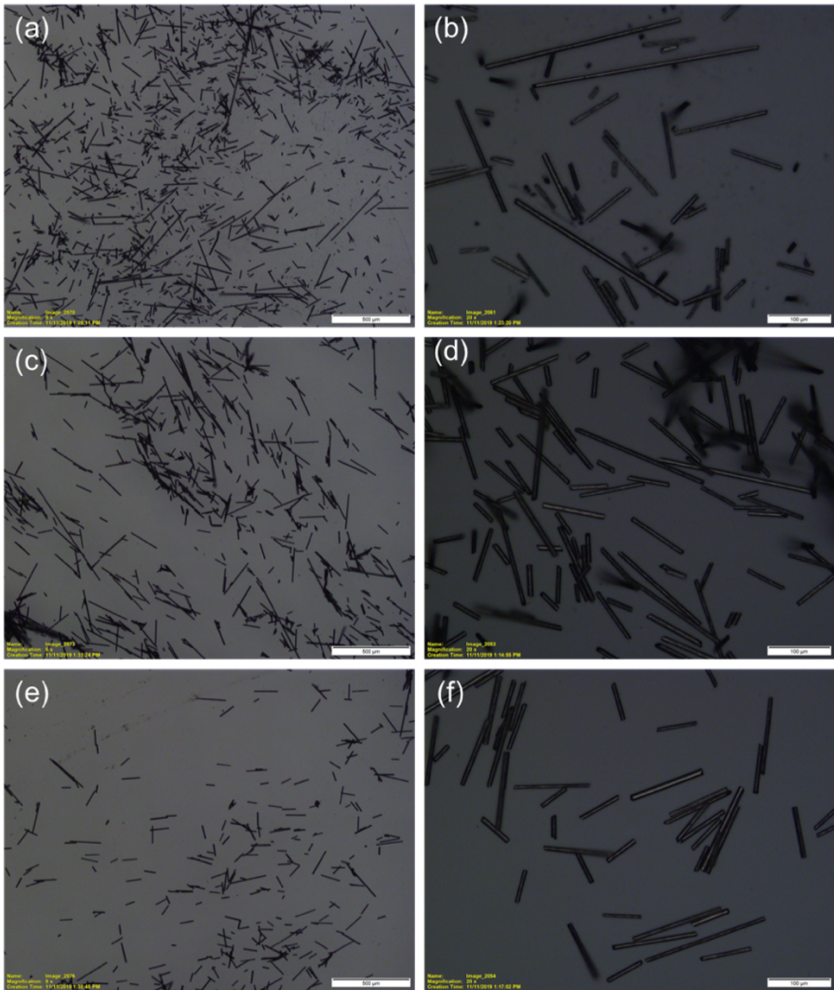

Figure 4.14 Optical microscope images of CFs underwent different surface modification processes. (a, b) As-received CF; (c, d) hydroxyl-CF; (e, f) norbornene-CF. Note: (a, c, e) 5x magnification; (b, d, f) 20x magnification. Scale bar locates at the bottom right.

Table 4.1 Table of average and standard deviation of fiber lengths for as-received CF, CF-COOH and CF-Nb.

	As-received CF	CF-COOH	CF-Nb
Average	404.875	310.372	83.7533393
Standard Deviation	399.325	323.856	35.2103632

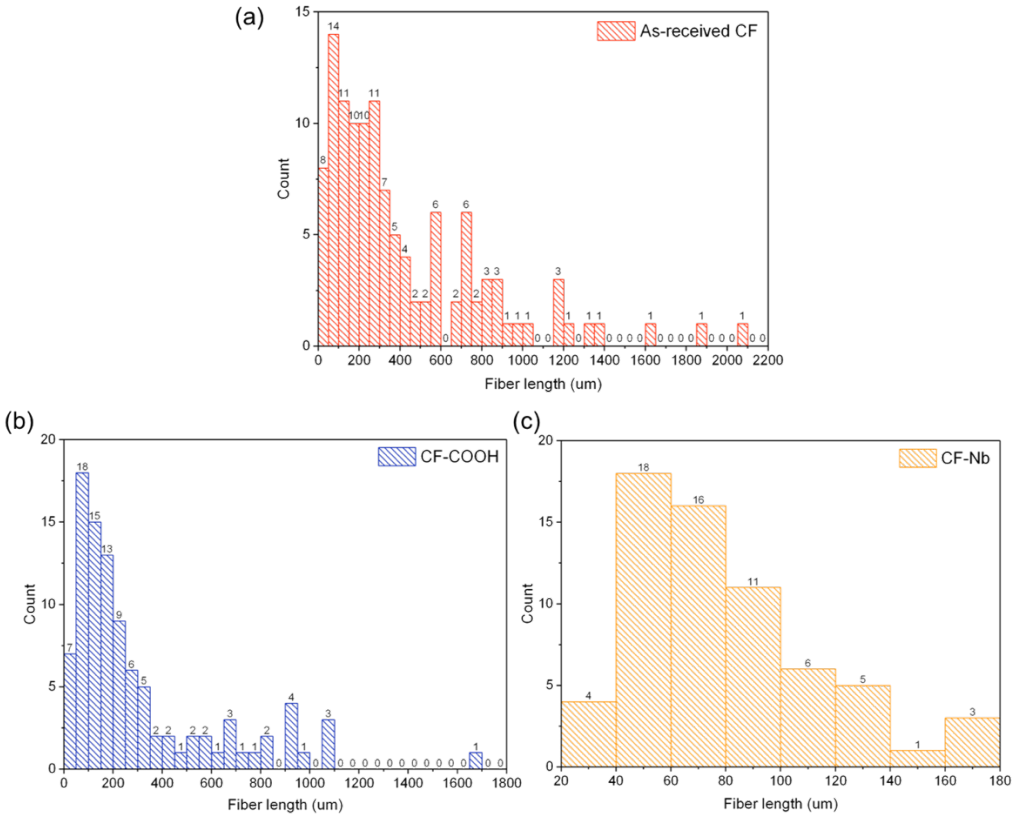

Figure 4.15 Histogram of fiber lengths for (a) as-received CF; (b) CF-COOH; (c) CF-Nb.

4.3.6 Fiber-matrix interaction

To test the function of functionalized fibers in fiber-matrix interaction enhancement, interlayer shear stress of printed specimens was analyzed via a lap shear test. A two-layer specimen with 2mm^2 contact area was printed, as shown in the inset pictures a, b in Figure 4.16. The other dimensions of the lap shear test specimen are

described in Section 4.2.5. The two ends were griped and tightened in the load cell. Sandpapers were used to increase friction during the pulling process. The lap shear testing is shown in the inset picture (b) in Figure 4.16. As shown in Figure 4.16. the interlayer shear strength of norbornene-grafted fiber was significantly improved compared to neat resins. On average, the interlayer shear strength of the norbornene-grafted fiber was improved by ~133%, ~52%, and ~255% concerning carboxyl-grafted fiber/DCPD, sized-fiber/DCPD, and neat DCPD. This proves the fiber-matrix interlayer improvement with the fiber surface modification where the presence of functional fiber at the interface and the enhanced bonding between fiber and matrix help improve the interfacial shear stress.

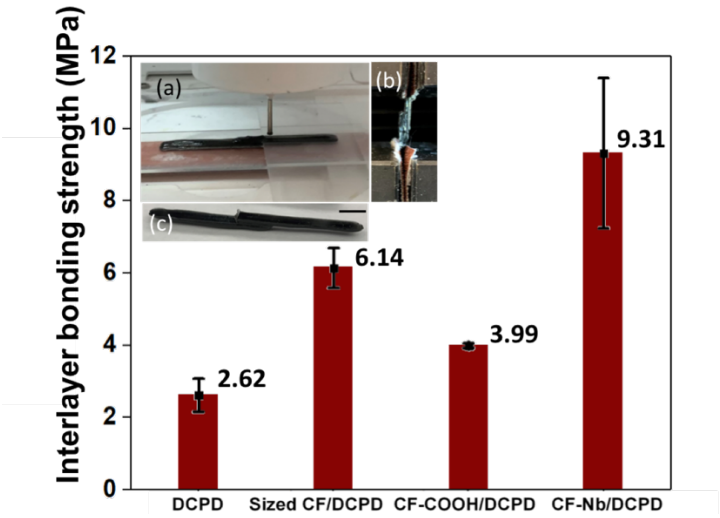

Figure 4.16 Effect of functionalized carbon fiber on interfacial bonding of printed composites. Inserted in inset image c is the scale bar, which stands for 2mm.

Besides, FTIR analysis was carried out for characterizing the interfacial shear stress specimens (specifically the interfacial area). The delaminated surface was analyzed using the ATR-FTIR module. The results are shown in Figure 4.17. From the FTIR graph,

CF-Nb/DCPD composites and neat DCPD ones exhibit identical peaks while functional chemical bonds are missing for the as-received CF/DCPD ones. Interestingly, sized-CF filled composites exhibited a higher interlayer bonding strength than carboxyl-CF filled composite. That attributes to the sizing agent coated on the fiber surface. The sizing usually contains a great number of active functional groups that can help improve wettability and affinity on the fiber surface, thus, creating strong binding energy between polymer matrix and fibers[182]. On the other side, unitary surface modification of carboxyl group on the fiber surface along with oxygen-deprived alkene chain dominated DCPD matrix together weakened binding energy, thus compromising the interlayer bonding strength between carboxyl-CF and DCPD matrix. Microscopy characterization of cross-section structures were applied and shown in Figure C1 and C2.

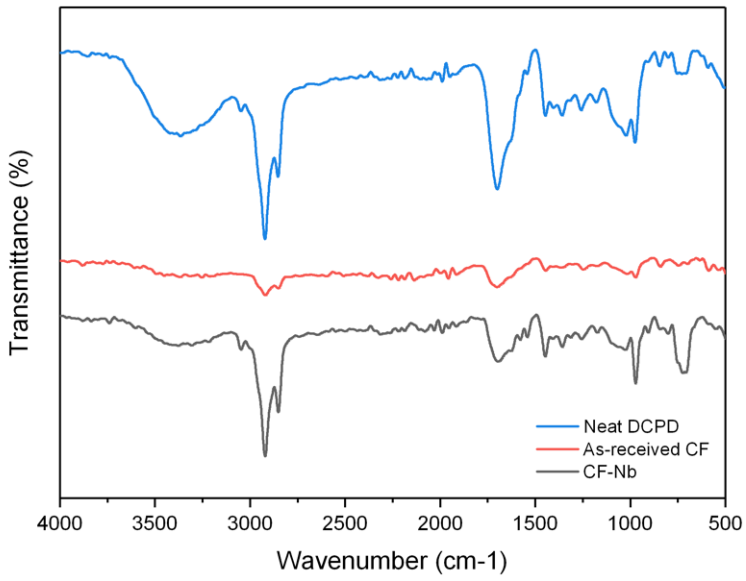

Figure 4.17 Fourier-transform infrared (FTIR) of the delaminated surface of lap shear testing bars. Blue, red and gray represent neat DCPD, as-received CF/DCPD composites and CF-Nb/DCPD composites, respectively.

4.4 Summary

Lightweight short carbon fiber/DCPD thermosetting composites were printed via frontal polymerization. The incorporation of short CF was aimed to strengthen the DCPD polymer matrix. Surface modification of fibers with highly reactive norbornene groups facilitate the in-situ print-and-cure and the simultaneous fiber-matrix interaction enhancement. The tensile strength of the printed norbornene-CF composites was around 43.3MPa, which was 170% higher than printed neat DCPD resin and 32% higher than as-received sized-fiber/DCPD composites. The toughness of the printed composites was ~14 MPa, ~33.3% higher than printed sizing CF/DCPD composites. Moreover, with the filler-matrix interaction enhancement, the interlayer bonding strength of printed norbornene carbon fiber composites were 9.31 MPa, which was a ~255% increase compared to neat DCPD. The aforementioned experimental results demonstrated the effectiveness of adopting norbornene functionalized CF in enhancing the mechanical performance of printed DCPD composites. Further research needs to avoid fiber shortening during the surface modification process. Simplifying surface modification process, involving less agitative process and better fiber dispersion methods will be investigated to achieve effective surface functionalization while maintaining the original length, and thus significantly transforming the mechanical properties of printed thermosets.

CHAPTER V

3D PRINTING SUPER STRONG HYDROGEL FOR ARTIFICIAL MENISCUS*

Reprinted with permission from [179]

5.1 Introduction

The meniscus is a piece of crescent-shaped cartilage that cushions and stabilizes the knee joint[11-13, 183-187]. Each year, in the US and Europe, around 1.5 million people need meniscus treatments according to the reports[11-14]. Tissue engineering is a promising approach to solve limited donor supply, biocompatibility and mismatch problems. The emerging 3D printing technique could engineer on-demand customer-specific artificial meniscus. One challenge for 3D printing artificial meniscus is the mechanical performance, which highly depends on the material properties in combination with the printing process. Previous endeavors have devoted to synthesizing hydrogel with varying formulations, but the resultant mechanical performance is inferior to the natural meniscus. Thus, it is not able to meet the demand.

Hydrogels that consist of crosslinked polymer chains and high water content are a class of biomaterials commonly used in nowadays tissue fabrication, including meniscus. In general, nanocomposites (NC) gel[15-17], double network (DN) gel[18-20], slide-ring (SR) gel[21, 22] and ionic-covalent entanglement (ICE) gel[23, 24] are four typical types of hydrogels used or studied in medical applications. Among them, DN hydrogel is known as the most attractive one for its exceptional mechanical properties attributed to the synergistic effect of interpenetrated soft and hard polymer chains via the energy dissipation mechanism. One example is the poly (2-acrylamido,2-methyl,1-propanesulfonic acid)

(PAMPS)/PAAm hydrogel reported by Guo et al[18-20] with a tensile strength of 1-10 MPa, compressive strength from 20 to 60 MPa, and toughness from 10^3 to 10^4 kJ m^{-3}. In 2017, the PAMPS/PAAm DN hydrogel was printed. A two-step method was employed where the second PAAm polymer network was formed after the first PAMPS network was printed and crosslinked by UV light[26]. This reported DN gel exhibited a tensile strength of 1.4 MPa[26], not comparable to the traditional molding one, and is unable to meet the original meniscus tissue performance.

In this chapter, a single network hydrogel polymer that containing both soft (AAm) and stiff (phenyl acrylate (PA)) components are selected and 3D printed. The soft and stiff components differ in hydrophilic and hydrophobic properties are crosslinked in one step to form the P(PA-co-AAm) copolymer. Here, PA is selected because it introduces the hydrophobic benzene groups in the copolymer chain to enhance mechanical performance. The synthesized copolymer performed superior mechanical strength and toughness. This is attributed to the synergistic effect of stiff (hydrophobic) and soft (hydrophilic) components. To facilitate printing, cellulose nanocrystals (CNCs) were incorporated to adjust the viscosity. The mechanical performance (tensile) of printed hydrogel was included in this study as well as the dimensional check for printing accuracy.

5.2 Experiments

5.2.1 Preparation of printable hydrogel inks

Phenyl acrylate (PA, Tokyo Chemical Industry Co., Ltd) monomer was mixed with another monomer acrylamide (AAm, Sigma Aldrich) and crosslinker N,N'-methylenebisacrylamide (MBAA, Sigma Aldrich) in Dimethyl sulfoxide (DMSO, Micro

Fine Chemicals). A series of inks with varied PA, AAm, MBAA molar concentrations were prepared and studied in this research, denoted as PA: AAm: $MBAA_{(x:y:z)}$, thus corresponding inks forms copolymer hydrogels and denoted as $P(PA\text{-}co\text{-}AAm)_{(x:y:z)}$. Here x, y and z represent the molar concentration of PA, AAm and MBAA, respectively. To tune the rheological behavior of the inks, 1.0 g cellulose nanocrystal (CNC, CelluForce Inc) was dissolved in 8.1g DMSO and the mixture was homogenized via vigorous stirring and degassed before use. And 50mg Irgacure 2959 was added to the mixture as the photoinitiator.

5.2.2 3D printing of super-strong hydrogel

The printed structure was firstly designed in SolidWorks and then converted into g-code via Slic3r for printing purposes. Allevi 1 3D bioplotter was used to print the copolymer hydrogel. The prepared precursors were loaded into the cartridge and extruded out of the printhead via pneumatic force control. The diameter of the printed strands can be controlled by the pneumatic force. In this work, 5-10 psi is used for extrusion depends on the viscosity of the printed inks for a 24-gauge needle printed at a speed of 2 mm/s. The printed constructs were crosslinked under UV irradiation (Spectroline, ENF-280 C) in a nitrogen environment for about 10 min. The wavelength of the UV light source used here is 365 nm which is in the best absorption range for Irgacure 2959 photoinitiator.

5.2.3 Rheological characterization

Rheometer (Anton Paar Physica MCR-301) was implemented to study the rheological behavior of prepared inks. Inks with CNC concentrations ranging from 1-12wt% were measured via the 50 mm CP50-1 plate geometry.

5.2.4 Morphology characterization

Micromorphology of printed hydrogels was analyzed using Scanning electron microscopy (JEOL JSM-7500F). Before SEM characterization, the printed specimens underwent the solvent exchange and freeze-dried to remove the solvent content.

5.2.5 Solvent content measurement

The DMSO solvents in the as-printed hydrogels were then undergone the solvent exchange. The DMSO content (Q_1) before solvent exchange and water content (Q_2) after solvent exchange were analyzed, and their weights are denoted as $W_a \; and \; W_a'$, respectively. Noted: W_a' is the weight of the hydrogel after placing in air and dried for 1 hour. Then, the freeze-dried specimen was measured and denoted as W_d. Thus, solvent content was determined as:

$$Q_1 = \frac{W_i - W_d}{W_d} \times 100\% \tag{5.1}$$

$$Q_2 = \frac{W_a - W_d}{W_d} \times 100\% \tag{5.2}$$

Also, the water content of hydrogel specimens after 1-hour exposure in the air was noted as Q_2'. So Q_2' was calculated as:

$$Q_2' = \frac{W_a' - W_d}{W_d} \times 100\% \tag{5.3}$$

5.2.6 Mechanical characterization

Tensile specimens were printed with a modified dimension of the ASME D638 Type-V standard model. The tensile testing was performed on the Instron 3345 tensile machine (Instron Corporation, MA, USA) with a 2 kN load cell. The cross-section area of

the tensile specimen was measured by a caliper. Sandpaper was used to prevent slippery during the testing. The crosshead speed was set to 10 mm min^{-1}. The testing was performed at room temperature (~25 °C). Young's modulus was calculated using the strain of 0- 10%. The gel toughness (Γ_c) was obtained by integrating the area under the stress-strain curve.

Compression test was performed on cylinders with 10 mm diameter and 3 mm height on the same Instron test machine with a 10 kN load cell. The crosshead speed was set to 5 mm min^{-1} for the single-cycle compression test. Dimensions of the compression specimens were measured. A dynamic compression test with 25 cycles was also performed. The maximum compression strain for the dynamic compression test is set to 40%. The crosshead speed was set to 1 mm min^{-1}.

All specimens were tested as-printed or after solvent exchange.

5.2.7 Statistical Analysis

All quantitative experimental results were measured and presented as mean ± standard deviation. One-way analysis of variance (ANOVA), and Bonferroni method-based pairwise comparison were used in the statistical analysis. Here *, ** and *** indicated statistical significance: $p < 0.1$, $p < 0.005$, and $p < 0.0005$, respectively.

5.3 Characterization and results

5.3.1 Extrusion based 3D printing process

The 3D printed hydrogel was inspired by the one discovered by Jeon et al[188]. Hydrogel precursors containing co-monomers were 3D printed and formed single network copolymer chains via a one-pot reaction. The hydrogel was created based on the idea of incorporating the stiff (hydrophobic) and soft (hydrophilic) polymer segments in a single

network. The hydrogel precursors were first soaked in an organic solvent (DMSO) followed by the solvent exchange to get the hydrogel since PA is insoluble in water. The hydrogel fabrication process is illustrated in Figure 5.1.

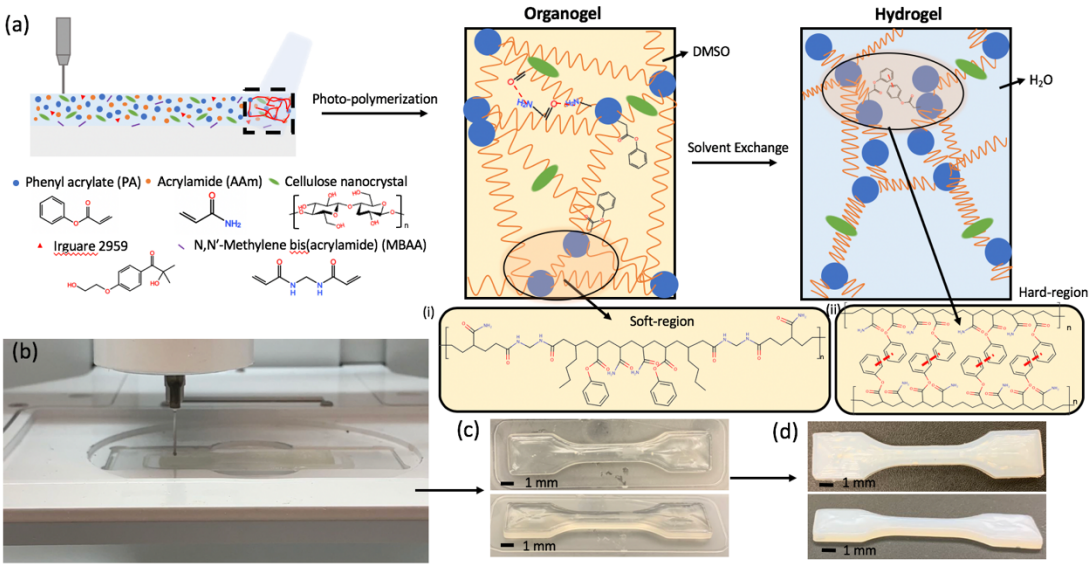

Figure 5.1 3D printing of hydrophilic-hydrophobic copolymer. (a) Illustration of the 3D printing process and structure transformation after solvent exchange; (b) Image of the 3D printing process; (c) Image of as-printed dogbone specimen; (d) Image of dogbone specimen after solvent exchange.

For the current hydrogel, its precursor contains PA (stiff region with the presence of phenol groups), AAm (soft region with exceptional elasticity) and MBAA crosslinker. CNCs were also introduced for adjusting the viscosity of the ink to facilitate printing. The presence of photoinitiators (Irgacure 2959) crosslink and form the polymer chains under UV irradiation (365 nm), thus, transformed the liquid to gel. After crosslinking, the copolymer networks (Figure 5.1a shows their chemical structures) extended when soaked in organic solvents. In DMSO solvent environment, phenol groups grafted on the copolymer chains were well dispersed and the phenol groups were separated by amides to

prevent π-π interactions. The copolymers with hydrophilic amide groups, dispersed phenol groups and the corresponding chemical structure were shown in Figure 5.1(i). When water diffused into the gel, benzene groups tended to expel water and aggregate together forming a densely packed 3D hard region with lower water content. Bendable stiff hydrogels were formed after solvent exchange. The chemical structures of the stiff region and the aromatic interactions between two phenol groups were shown in Figure 5.1a (ii). Because of the one-pot synthesis, the soft and stiff regions were randomly distributed in the copolymer chains. In Figure 5.1b, the 3D bioprinter is printing the proposed hydrogel precursor. Figures 5.1c is the image of as-printed organogel and Figure 5.1d is the obtained hydrogel after one-hour soaking of as-printed organogel in DI water. Color changed was observed after solvent exchange changing from clear transparent to opaque white, as shown in Figure 5.1c and 5.1d. The chemical composition is examined via FTIR (Bruker, ALPHA-Platinum), as shown in Figure 5.2. The missing peak at 1560 and 1570 cm^{-1} indicates the successful crosslinking of PA and AAm.

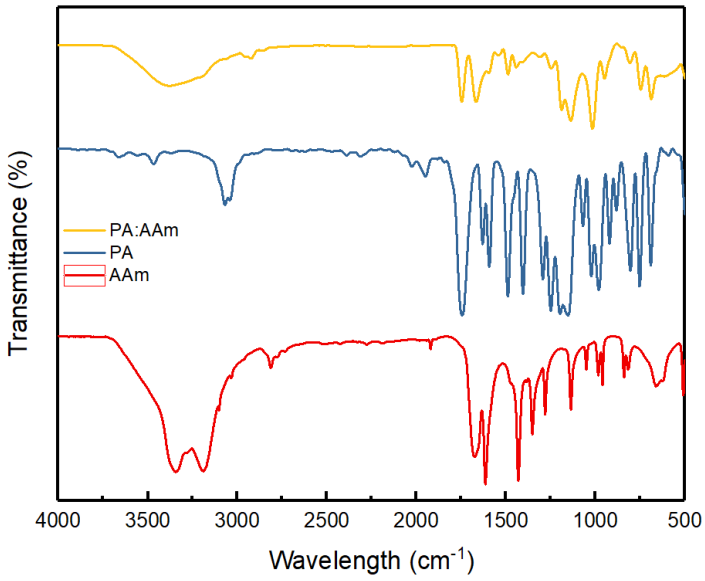

Figure 5.2 FTIR analysis of phenyl acrylate (PA), acrylamide (AAm) and crosslinked PA-AAm gel

SEM was applied to characterize the microstructure of the printed hydrogel, shown in Figure 5.3. The SEM image of P(PA-co-AAm)$_{(3:2)}$ hydrogel shows a densely compacted microstructure with small-scale 0.5-1.5 µm micropores.

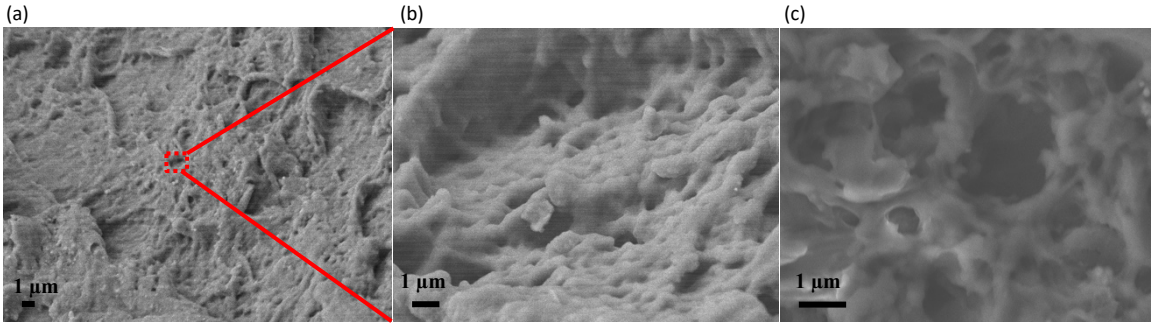

Figure 5.3 SEM image of prepared hydrogel with PA-AAm molar ratio of 3:2.

5.3.2 Rheological performance

To tune the printability of hydrogel, CNCs were incorporated as the rheological modifier to tune the viscosity and viscoelasticity. With the incorporation of CNC, shear thinning behavior was observed, because of its high aspect ratio CNC[189-192]. CNC is a biocompatible nano-filler derived from natural woods with crystallized structure. It has been widely studied in several biomedical applications for improved mechanical performance[193].

Viscosities (η) of DMSO solution with different CNC concentrations were measured to determine the suitable nanofiller concentrations for printing. The viscosity results are shown in Figure 5.4a. The viscosity-shear rate curve of the PA: $AAm_{(3:2)}$/12 wt% CNC solution was presented in Figure 5.4b. The shear rates that loaded precursors endured in the needle as well as the cartridge were calculated using the equation 5.4[194]:

$$\dot{\gamma} = \frac{8v}{d} \tag{5.4}$$

Here, $\dot{\gamma}$ stands for the testing shear rate, ν stands for the linear fluid flow rate (printing speed), and d stands for cartridge or needle's inside diameter (ID). Here, the printing speed is 2 mm s^{-1}. The ID of cartridge and needle used here are 16 mm and 0.311 mm, respectively. So, the corresponding shear rates at both conditions are 1 s^{-1} (in the cartridge) and 51 s^{-1} (in the needle), and these correspond to 100 Pa·s and 1.1 Pa·s viscosity points in Figure 5.4b. After precursors were printed on the platform, the shear rate was reduced to 0 resulting in a dramatic increase in viscosity[23]. Compared to the previous report[26], the precursor is printable since the required viscosity for printing varies according to needle

gauge, printing speed, and adjustable pressure range. Here, needles with a 24-gauge were used for printing under the pressure of 5-10 psi.

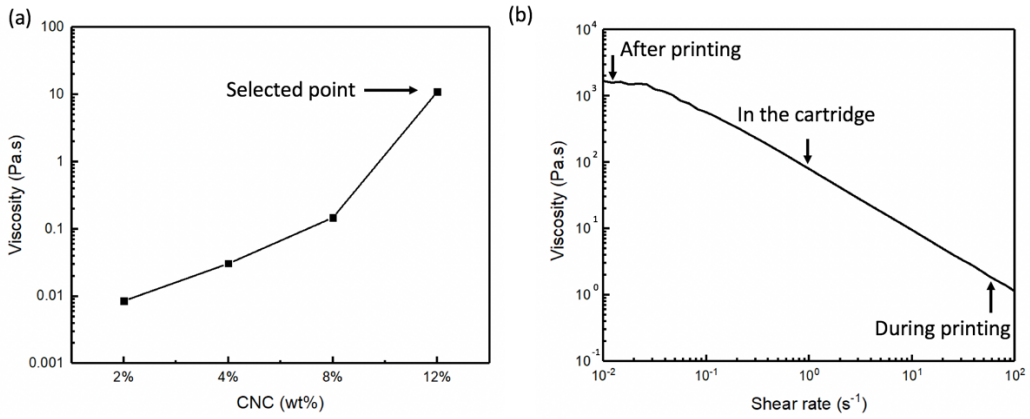

Figure 5.4 Rheology measurement. (a) The viscosity of aqueous solutions with different CNC concentrations at a constant shear rate of 10 s^{-1}; (b) Viscosity of the 3D printable solution as a function of shear rate.

Other viscosity-shear rate curves for CNC concentrations ranging from 2wt%-12wt% are showed in Figure 5.5.

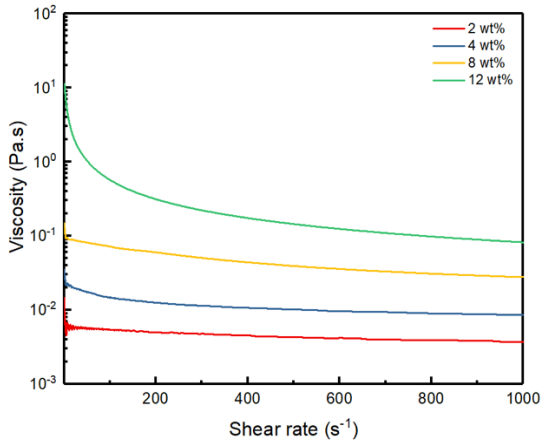

Figure 5.5 Viscosity vs. shear rate at different CNC concentrations

The viscosity-shear rate curves exhibited shear thinning behavior where the ink viscosity dramatically reduced with the growing shear rate and the shear force suddenly

decreased and showed high viscosity at a lower shear rate. The viscosity-shear rate curves follow a power-law model[195]:

$$\eta = K\dot{\gamma}^{n-1} \tag{5.5}$$

Here, *K* stands for the consistency index, and *n* stands for the power-law index. *K* is the apparent viscosity of fluids at a shear rate of 1 s^{-1}, and *n* stands for the degree of shear thinning behavior. When CNC concentration increased to 8 wt%, *n* is smaller than 1, and shear thinning behavior was observed. When CNC concentration continued to increase to 12wt%, its shear thinning behavior was more significant (*n* increased), and much thicker (*K* increased). The calculated values are shown in Table 5.1 and Figure 5.6. 12wt% CNC concentration was selected for its apparent shear thinning behavior and relatively higher viscosity that can help avoid sagging and spreading[24].

Table 5.1 Rheological parameters for CNC solutions. All the data listed above were measured at room temperature (25 °C).

Cellulose Nanocrystal (wt%)	Consistency (K [Pa s])	Power Law (n)
2	0.008	1.0
4	0.095	1.0
8	0.512	0.9
12	0.848	0.8

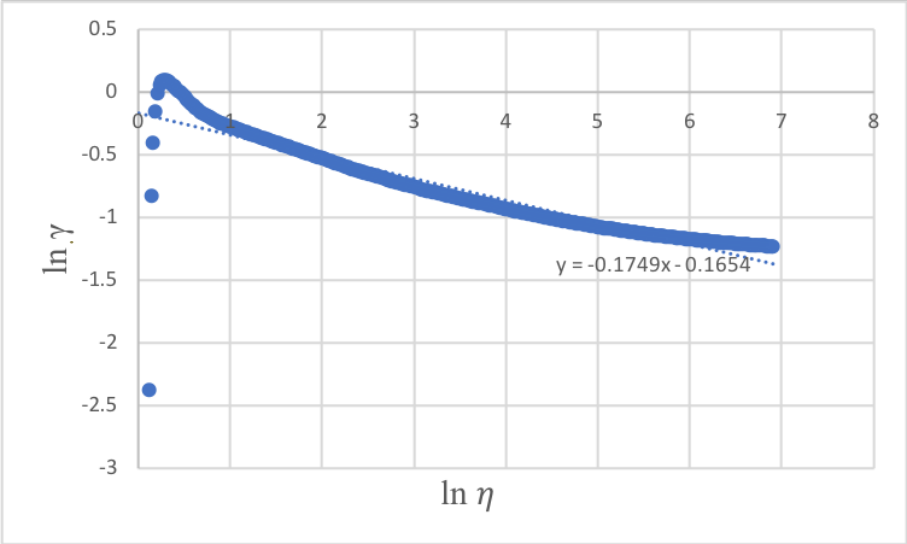

Figure 5.6 Example of Determining power law (n) and consistency (K) of 12 wt% CNC solution via linear regression

The power law (n) and consistency (K) were determined using the following conversion of the equation of viscosity power law (equation 5.6) to equation 5.7 before linear regression:

$$\eta = K\dot{\gamma}^{n-1} \tag{5.6}$$

$$ln\eta = ln\,K + (n-1)\,ln\,\dot{\gamma} \tag{5.7}$$

One example of the linear regression of determining n and K were shown in Figure 5.6. Hence, $n = 1 - 0.1749 = 0.8251$ and $K = e^{-0.1654} = 0.8476$.

5.3.3 Tensile performance

Compared to previous 3D printed hydrogels, the single network copolymer exhibited superior performance with the simplified printing process. Characterization and analysis of its printability, mechanical performance and water content are included.

The prospects of the printed PA: AAm hydrogels in load-bearing applications were evaluated in tension first. Dogbone shaped specimen was printed for tensile testing, shown in Figures 5.7a-c. The typical stress-strain curves of printed hydrogels with various PA: AAm compositions are illustrated in Figure 5.7d. P(PA-co-AAm)$_{(4:2)}$ presented a superior strength (~19 MPa) but limited strain (~20%) compared to other compositions due to the high concentration of PA. For other compositions, extended strain up to 180% was observed while the strength was less than 5 MPa. This was due to the higher molar ratio of the elastic AAm group in the copolymer chain. Besides, comparable tensile strength was observed for molded and printed hydrogels where the organogel demonstrated a significantly lower strength (~0.5 MPa) at the same material concentration. This indicates the effective tensile strength enhancement of P(PA-co-AAm) gel after solvent exchange. The enhancement in tensile strength may contribute to the aggregation of hydrophobic benzene groups which expelled the surrounding water molecules and formed a hard region in the hydrogel. Furthermore, unlike the conventional printing process where the tensile performance of 3D printed specimens deteriorates due to the lack of interlayer bonding, the involvement of solvent exchange helps reduce the interfacial gap. The reduction in the height of the printed specimens further proved the reduction in the interfacial gap, as shown in Table C1.

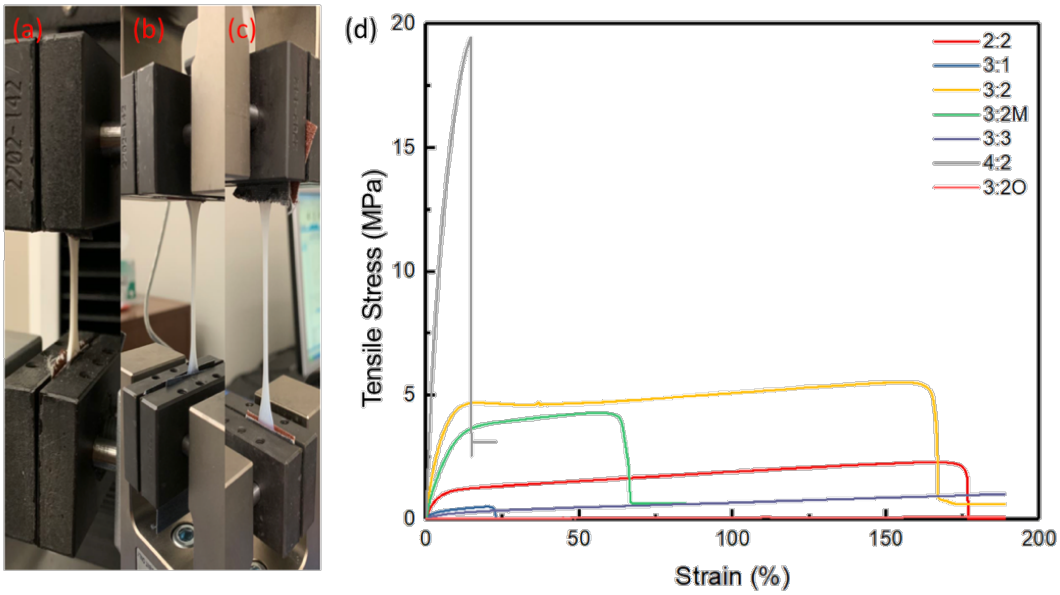

Figure 5.7 Tensile characterization. (a) Tensile experiment of P(PA-co-AAm)$_{(4:2)}$ hydrogel; (b), (c) Tensile experiment of P(PA-co-AAm)$_{(3:2)}$ hydrogel. (d) Tensile stress-strain curve.

The tensile strength, Young's modulus and toughness of the hydrogels with a series of PA: AAm molar ratios are shown in Figure 5.8.

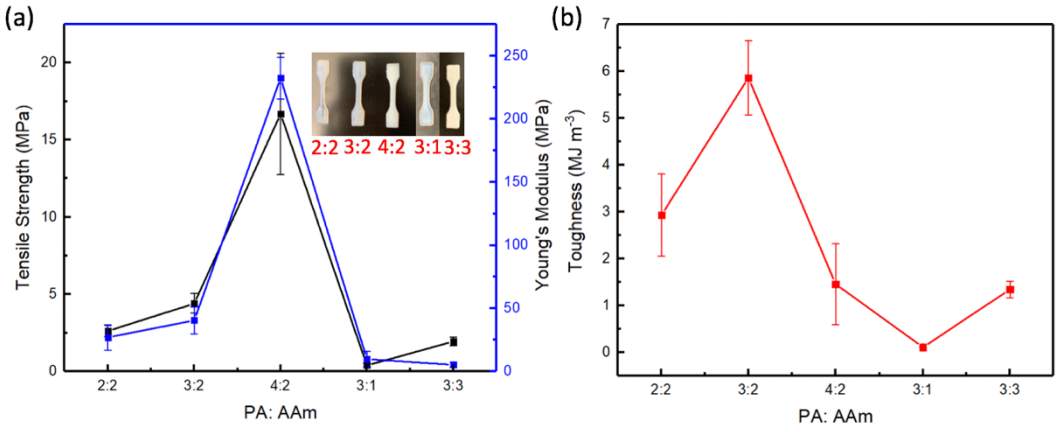

Figure 5.8 (a) Tensile strength, Young's modulus and (b) Toughness of printed hydrogel with varied PA and AAm concentrations.

At least three specimens were prepared for each hydrogel composition. Figures 5.8a demonstrate the effect of PA monomer concentration on tensile performance. The inset picture in Figure 4a shows hydrogel specimens of different PA: AAm molar ratios (2:2, 3:2, 4:2, 3:1, 3:3 from left to right). With the increasing PA concentration, the hydrogel was getting less transparent. When the PA: AAm molar ratio reached 4:2, the specimen became completely white and opaque. This was caused by the high concentration of hydrophobic PA and increased aggregation of the benzene groups. The tensile strength was greatly improved with the increasing PA concentration at the same AAm concentration. Young's modulus was determined by the slope of the elastic region (linear potion) of the stress-strain curve, while toughness was calculated by the area under the curve. Tensile strength, Young's modulus and toughness were ~4.4 MPa, ~40.6 MPa, and ~5.9 MJ m^{-3} at P(PA-co-AAm)$_{(3:2)}$ molar concentrations and changed to ~16.7 MPa, ~232.4 MPa, and 1.5 MJ m^{-3} at the higher PA molar concentration of P(PA-co-AAm)$_{(4:2)}$. The decrease of toughness can be explained by the higher PA molar ratio which resulted in the significant reduction of fracture strain. Thus, the PA concentration was fixed at 3 mol% and the suitable AAm concentration was then determined. Similarly, the tensile strength, Young's modulus and toughness of hydrogels with fixed PA concentration but different AAm concentrations were analyzed. Toughness of printed hydrogels with different PA: AAm molar ratios are shown in Figure 5.8b. For specimens of P(PA-co-AAm)$_{(3:1)}$, the tensile strength, Young's modulus and toughness all reached their summit, which are ~0.4 MPa, ~ 9.7 MPa, and ~0.1 MJ m^{-3}, respectively, much inferior to the P(PA-co-AAm)$_{(3:2)}$ hydrogels. Further increase of AAm concentration above 2 mol% led to the

reduction of tensile performance. These results indicated that the copolymer exhibits the optimal tensile performance when the elastic component and the rigid component reach their balance[188]. The statistical significance of the aforementioned measurement results shown in Figure 5.8 including tensile strength, modulus and toughness were indicated in Table C2.1-2.4.

The effect of solvent exchange time was characterized by immersing specimens in DI water for a different period ranging from 0 to 60 minutes with an interval of 15 minutes. The stress-strain curves are given in Figure 5.9 and the inset picture shows the tested specimens with different immersing times. There is a significant increase in tensile stress after immersing in water for 60 minutes, but a slight decrease in fracture strain. The results also indicate that the water content of the hydrogel specimens affects the tensile performance.

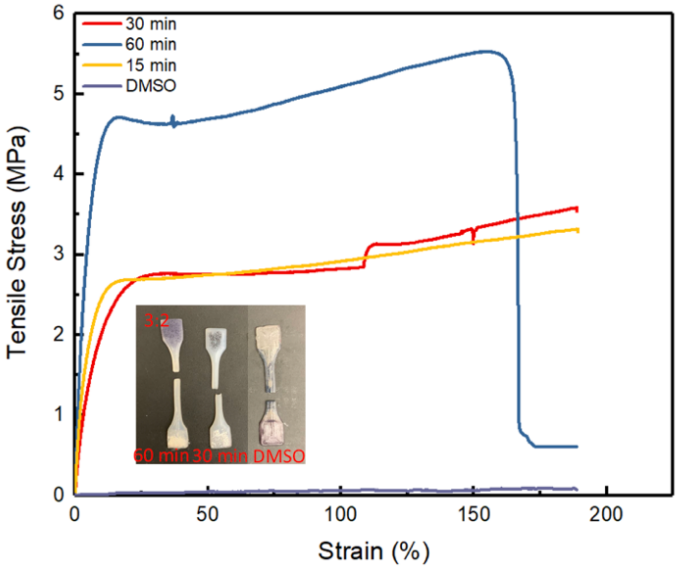

Figure 5.9 Tensile stress-strain curve of different solvent exchange times

To further understand the solvent effect on mechanical performance, the water content was calculated for each PA: AAm composition, shown in Figure 5. Both the water content after solvent exchange and the water content after placing the hydrogel specimens in the air for 1 hour after solvent exchange was characterized. These are represented by the weight loss ratio (Q_1, Q_2) after hydrogel was freeze-dried. From the calculation results, the water content was closely related to the PA: AAm concentration. The water content greatly reduced with the increasing concentration of PA, whereas the water content increases with the increasing concentration of AAm. This can be explained by the intrinsic hydrophobicity of PA and hydrophilicity of AAm. Besides, the loss of water content is indicated by the difference between the two water content values. It is observed that a higher concentration of PA is more susceptible to water loss due to the increase of PA aggregation which expelled an increased amount of water. This phenomenon is also validated by the color change during the solvent exchange where higher PA concentration resulted in whiter and more opaque hydrogels, as shown in the inset image of Figure 5.9.

Specimens with high PA concentration and low AAm concentration, though exhibiting exceptional tensile strength, are hard to keep water from evaporation. They can easily drop below the water content lower bound of natural soft tissues such as skin and cartilage, specifically in the range of 50 wt% to 70 wt%[196, 197]. Therefore, exceeding PA concentrations like 3:1, 4:2 compositions are not ideal. The composition of P(PA-co-AAm)$_{(3:2)}$ which exhibited a high water content and the rate of water loss is considered more suitable for artificial meniscus fabrication. The above results further confirmed the importance of water content in determining hydrogel performance. The statistical

significance of the comparison between specimens with different PA: AAm compositions presented in Figure 5.10 were analyzed and the results were shown in Table C2.5-2.6.

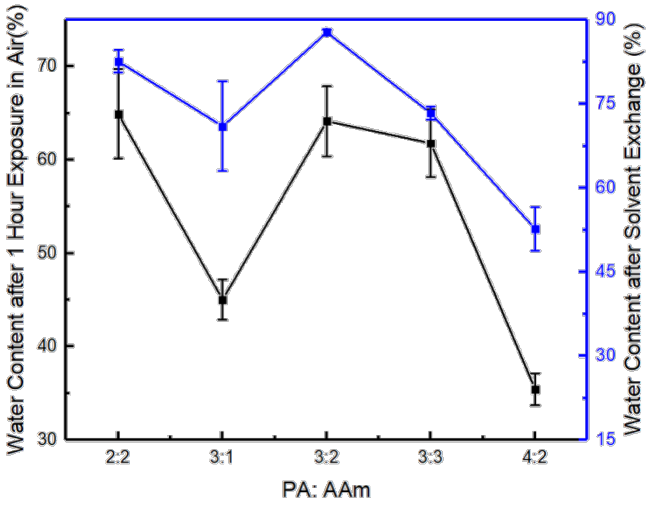

Figure 5.10 Water content calculation of hydrogel specimens with varying PA: AAm ratios.

The crosslinker effect on the tensile performance was also studied, shown in Figure 5.11. The image of tested specimens is given in the inset of Figure 5.11a. By tuning the concentration of MBAA (0.25 mol% to 0.75 mol%) while fixing PA: AAm molar ratio (3:2), no obvious difference in tensile strength was observed. The typical stress-strain curves of specimens with varied crosslinker concentrations are shown in Figure 5.12. The hydrogels with lower MBAA concentration (0.25 mol%) exhibited a higher tensile strain, while the tensile strengths of specimens at 0.5 mol% and 0.75 mol% MBAA concentrations are comparable and ~12.5% higher than specimens at MBAA concentration of 0.25 mol%. The increase in strength was due to the increased crosslinking density resulted from higher crosslinker concentrations, thus creating adequate three-dimensional crosslinking polymer structures. The obtained Young's modulus of

specimens with 0.75 mol% MBAA concentration was ~10 MPa higher than 0.5 mol% and 0.25 mol%. However, hydrogel specimens with 0.25 mol% MBAA concentration yielded a higher toughness (~1.7 MJ m^{-3}), about 15% and 17% increase from 0.5 mol% and 0.75 mol%, respectively. By tuning the MBAA concentrations, the printed hydrogels can have either superior tensile strength or improved toughness. Specifically, hydrogel specimens with 0.25 mol% MBAA concentration, which showed improved toughness and well-balanced hydrophilic and hydrophobic chain fractions, have comparable properties to load-bearing tissues like the meniscus. The level of significance of the comparison between the tested specimens with different crosslinker concentrations was compared and the results were presented in Table C3.1-3.4. The level of significance is shown in Table C4.

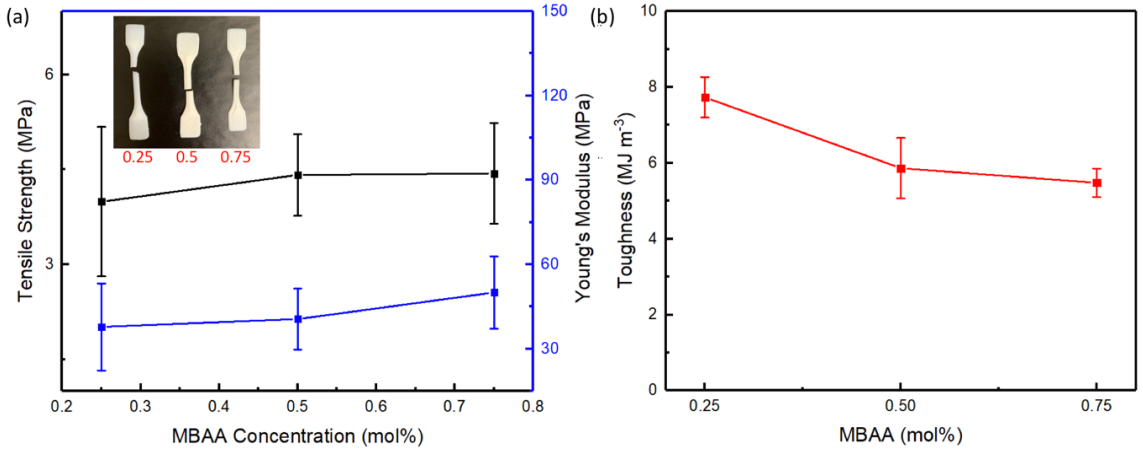

Figure 5.11 Tensile characterization. (a) Tensile strength; (b) Young's modulus; (c) toughness for various MBAA concentrations.

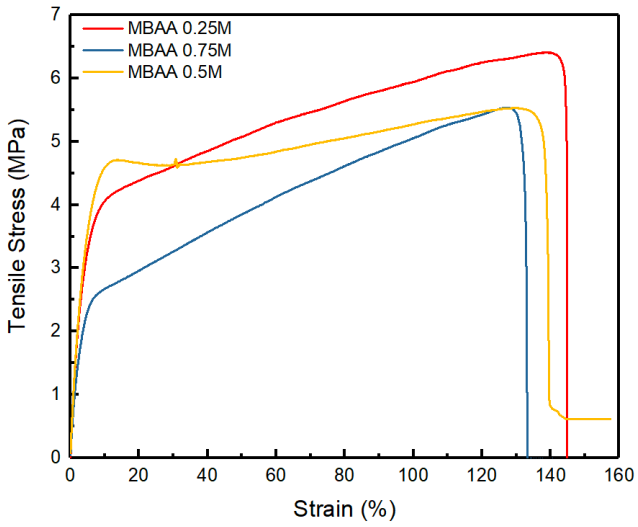

Figure 5.12 Tensile stress-strain curves of P(PA: AAm)(3:2) hydrogel with different MBAA concentrations

5.3.4 Compression performance

Compression performance is critical to hydrogels for load-bearing tissue applications. Compression tests of hydrogel specimens with a series of PA: AAm concentrations were conducted. Figure 5.13a shows the typical compression stress-strain curves of P(PA-co-AAm)$_{(3:2)}$ gels before and after solvent exchange. The organogel exhibited a higher compression strain (up to 70%) compared to the hydrogel specimen (less than 50%) with the same composition. However, the compression strength of the hydrogel was ~21 MPa, about 13-fold higher than the organogel (~1.5 MPa). The compression strength and compressive modulus of varied PA: AAm concentrations are given in Figures 5.13b and 5.13c. At the same AAm concentration, the compression strength and compressive modulus increased with the increasing PA concentration due to the intrinsic rigidity of the benzene ring and enhanced benzene-benzene aggregation[198].

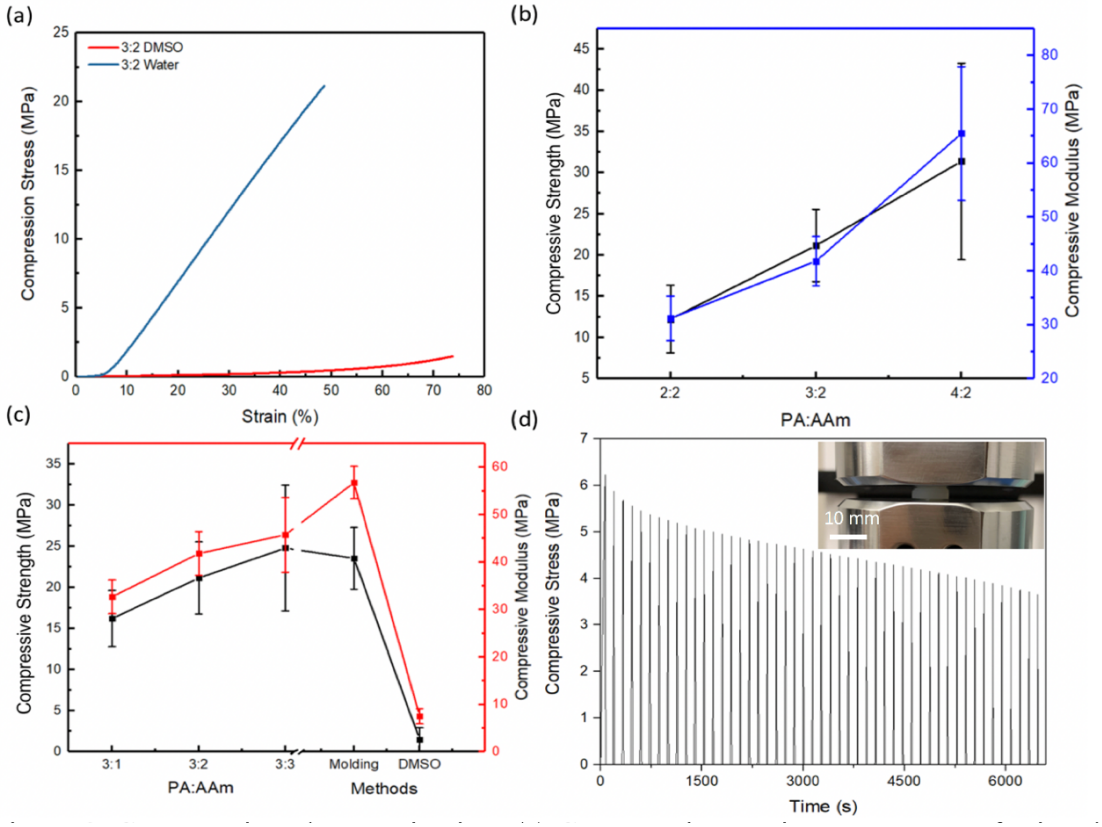

Figure 5.13 Compression characterization. (a) Compression strain-stress curve of printed hydrogel with PA: AAm composition of 3:2; (b) Compression strength as a function of AAm concentration and various treatment methods; (c) Compression strength as a function of PA concentration; (d) Dynamic compression test of 25 cycles.

The compression strength and compressive moduli were ~31.1 MPa and ~65.5 MPa, respectively, for P(PA-co-AAm)$_{(4:2)}$, ~9 MPa and ~20 MPa increased compared to P(PA-co-AAm)$_{(3:2)}$ specimens. Similarly, the compression strength and compressive modulus slightly increased with the increasing amount of AAm with the same level of PA concentration. The compression strength and compressive modulus were ~21.2 MPa and ~41.8 MPa for P(PA-co-AAm)$_{(3:2)}$, and increased to ~23 MPa and ~45.8 MPa when AAm concentration increased to 3 mol% at the same PA concentration. The increase was less

significant compared to PA because AAm with linear alkene structure is known to be less hard than aromatic PA, thus exhibited a smaller impact in improving compression strength compared to PA. Compared to the printed specimens, the compressive strength and compressive modulus of the molded specimens with the same PA: AAm molar ratio was ~1.5 MPa and ~12 MPa higher.

To further test the dynamic performance of hydrogel under compression, a cylindrical hydrogel with P(PA-co-AAm)$_{(3:2)}$ composition was compressed to a strain of 37% at a rate of 2 mm s^{-1} and released to its original height at the same speed after holding the position for 1 s, as shown in the inset of Figure 5.14. The specimens were continuously tested for 25 cycles. High levels of hysteresis are observed in the compression stress-strain curves of the first loading-unloading cycle (Figure 5.14). After the first cycle, 34% of hysteresis was recovered in the second cycle. The deformation was not recoverable after waiting for 18 hours. This was due to the permanent damage of the PA region for further deformation while energy was only partially dissipated through the soft AAm region. The maximum compression stress gradually decreased from ~6.18 MPa to 3.8 MPa after 25 compression iterations, as shown in Figure 5.13d. The previous damaged rigid region was softened and no longer effective in energy dissipation, which caused a decrease of maximum compression stress. All the characterized mechanical performance are summarized in Table 5.2.

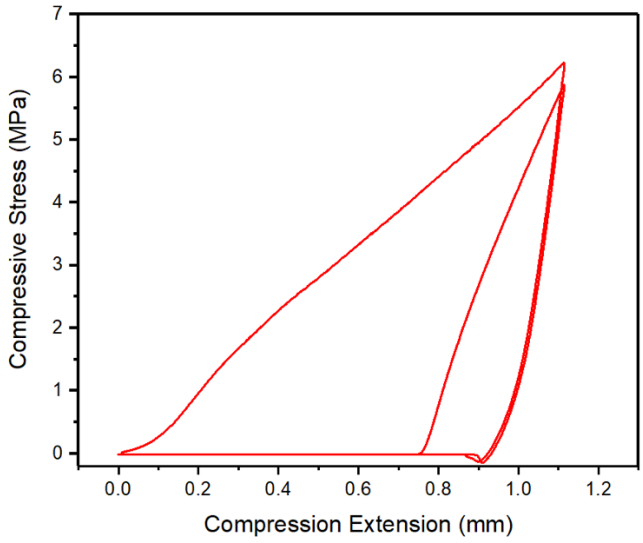

Figure 5.14 1st and 2nd loading-unloading compression stress-compression extension curves of hydrogel P(PA-AAm)(3:2)

Table 5.2 Mechanical properties of printed gel and bovine cartilage

Sample composition (PA: AAm)	Tensile strength (MPa)	Young's modulus (Tensile) (MPa)	Compressive strength (MPa)	Young's modulus (Compression) (MPa)	Toughness (kJ m^{-3})
2:2[a]	2.6 ± 0.35	27 ± 10.06	12.2 ± 4.11	31.2 ± 4.12	2.9 ± 0.88
3:2[a]	4.4 ± 0.65	40.6 ± 10.83	21.2 ±4.37	41. 8 ± 4.59	5.9 ± 0.80
4:2[a]	16.5 ± 3.94	232.4 ± 16.46	31.1 ± 11.94	65.5 ± 12.44	1.5 ± 0.86
3:1[a]	0.4 ± 0.13	9.7 ± 6.18	16.2 ± 3.42	32.7 ± 3.54	0.1 ± 0.02
3:3[a]	1.9 ± 0.26	5.2 ± 1.96	24 ± 7.64	45.8 ± 7.87	5.86 ± 0.80
Bovine Cartilage[29]	0.53-9	10.1-28.3	14-59	0.31	-

[a] Contains with 0.5 wt% MBAA

5.3.5 3D printing meniscus

The capability of our printing process and proposed inks were tested. The demonstration of printing meniscus as a typical meniscus-like shape is given in Figure 5.15.

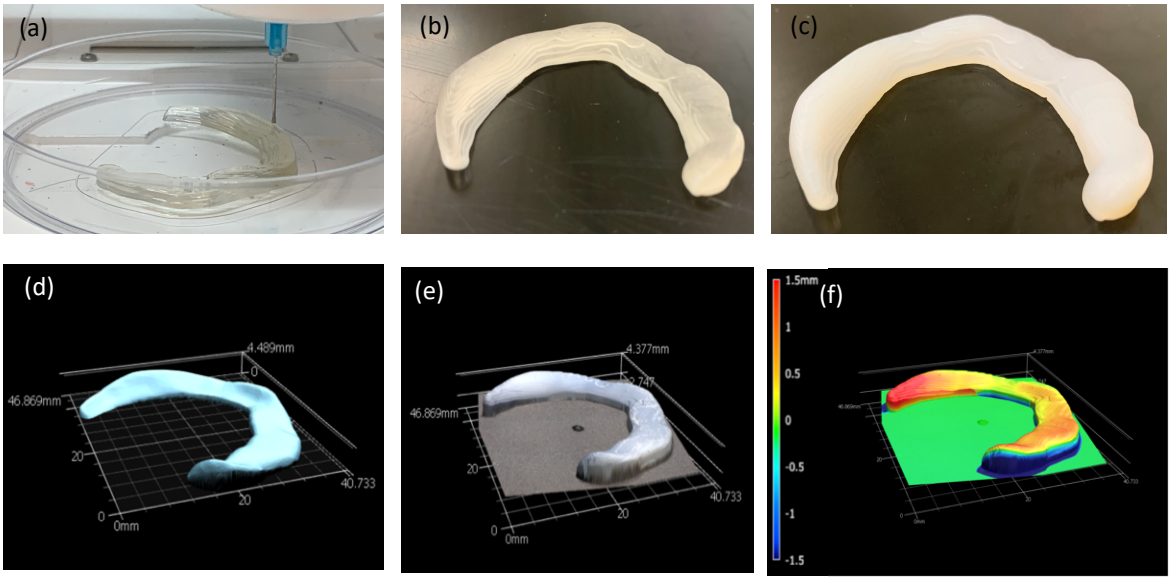

Figure 5.15 3D printing of meniscus demonstration. (a) Printing process; (b) As-printed meniscus; (c) Obtained meniscus hydrogel after solvent exchange; (d) original CAD model; (e) printed model (60 min solvent exchange) generated from 3D scanning; (f) comparison of the original CAD model and printed model in height.

Here, PA: $AAm_{(3:2)}$ formulation was used for printing the artificial meniscus. Figure 5.15a shows the meniscus printing process using the extrusion-based bioprinter. The printed meniscus presented clear features, as shown in Figure 5.15b. The as-printed organogel was transparent and gradually became opaque white after immersing in DI water. After 60 min solvent exchange, the meniscus maintained the original features without noticeable shrinkage, as shown in Figure 5.15c.

A 3D wide-area measurement system (VR-5000 Series, Keyence) was used to further examine the precision of the printed artificial meniscus. The set up was shown in Figure 5.16.

Figure 5.16 3D wide-area measurement system (VR-5000 Series, Keyence)

The printed meniscus (after 60 min solvent exchange) was positioned on the stage and scanned using the 3D measurement system, as shown in Figure 5.16. The original computer aided design (CAD) model and the generated model of 3D printed meniscus from 3D scanning were shown in Figure 8d and e, respectively. Besides, the top view of the original CAD model, the printed model and the overlay between the aforementioned two models were shown in Figure 5.17a, b, c, respectively. The inset in Figure 5.17b indicates the overall x-, y-dimension of the printed meniscus. In Figure 5.17c, the two models highly overlapped, and only observed a slight shrinkage in the printed model.

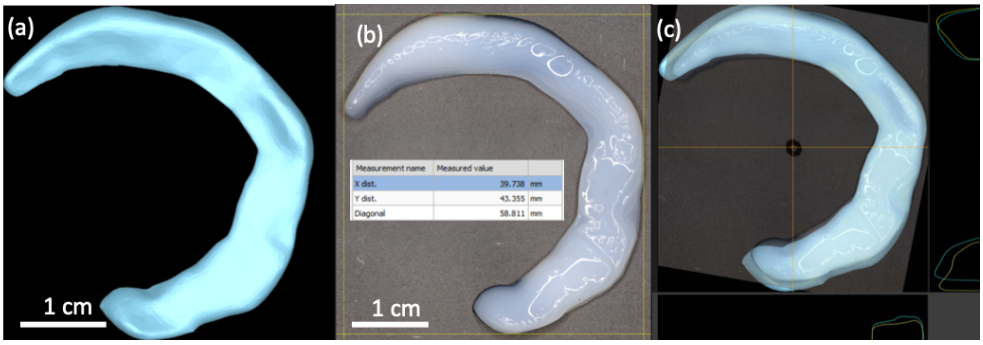

Figure 5.17 (a) Original model for printing (CAD file); (b) Printed model (60 min solvent exchange, 3D scanned model); (c) CAD file and 3D scanned model overlay

A more detailed comparison of two models in height and position alignment was shown in Figure 5.15 and 5.18. The yellow and light blue represent the original CAD model and printed model, respectively. Only a ~0.4mm left shift of the printed model was observed for the bottom area. The 3D height model was also generated by comparing the printed model to the original ones, as shown in Figure 5.15f. The height color bar was shown in the left of Figure 5.15f which indicated that the height difference between the two models was within the range of 1.5 mm. Specifically, green indicates zero difference in height, yellow and light blue indicate a slight ($\pm$ 0.5 mm) difference and red and dark blue indicate a larger difference ($\pm$ 1.5 mm). A more thorough comparison in height was shown in Figure 5.18.

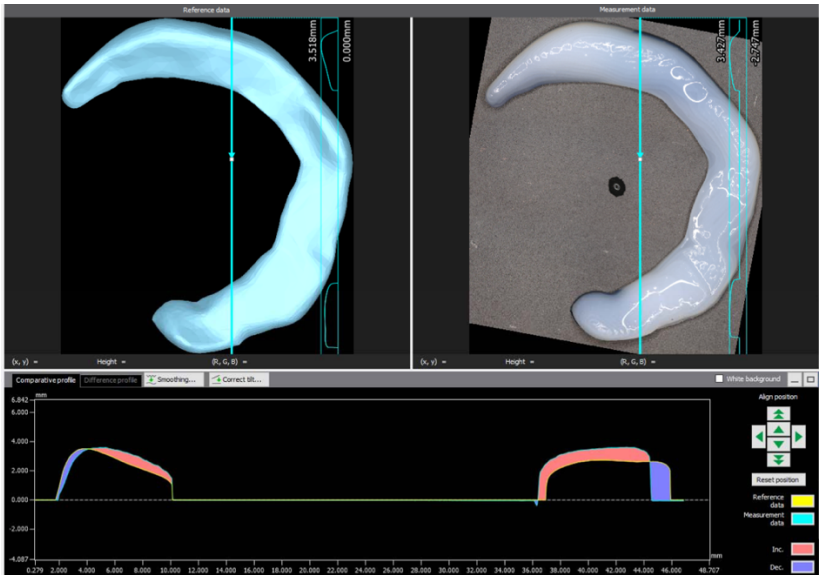

Figure 5.18 CAD file (left) against the printed model (right) in height and position alignment.

The above demonstration is appealing. It suggested the feasibility of adopting 3D printing in patient-specific load-bearing tissue engineering. This will help in resolving current challenges in engineered meniscus fabrication[26].

5.3.6 Comparison to state-of-art 3D printed and molded hydrogels

PAAm has been known as one of the most promising hydrogels and used in many DN hydrogels as either soft or hard polymer network. A great number of PAAm based hydrogels accompany by other hard or soft, synthetic or natural biomaterials were reported[23, 26, 99, 106, 137, 189, 199] and their results are summarized in Figure 5.19 and Table 5.3. In this work, instead of incorporating the PAAm polymer chain as one network, PAAm was introduced as one component in the alternated copolymer network of AAm and PA monomers. Figure 5.19 compares the mechanical properties (tensile strength and toughness) of the proposed P(PA-co-AAm) hydrogel with previously reported PAAm

based DN hydrogels. The proposed P(PA-co-AAm) hydrogel with hydrophobic/hydrophilic components reached a tensile strength almost 3-fold higher than the 3D printed hydrogels. The obtained toughness of the proposed hydrogel is comparable to the molded PAAm based hydrogels. Moreover, there was a big difference in 3D printed and molded structures due to the weak interlayer bonding. With the incorporation of the solvent exchange process, the interlayer bonding was strengthened.

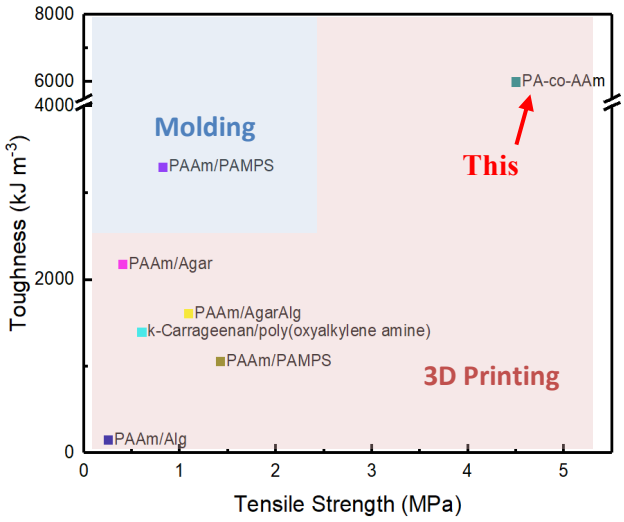

Figure 5.19 Comparison of tensile strength and toughness of PAAm based single polymer hydrogels[15, 18, 26, 137, 199-202]. The proposed hydrogel outperforms other 3D printed hydrogels. Compared with molded hydrogels, the proposed hydrogel has higher tensile strength and comparable work of extension.

Though the proposed copolymer structure with the designed alternating hard and soft region performed exceptional mechanical performance including strength and toughness, the introduction of benzene groups induced the poor the anti-fatigue properties of the proposed gel. The future endeavor will focus on improving anti-fatigue properties of the proposed material, thus making it more suitable for artificial load-bearing tissues.

Besides, the biocompatibility of the proposed gel remains unknown, the future work will examine the biological response to the material and the fabricated artificial tissue. Both the in vivo and in vitro experiments will be conducted to analyze the toxicity and biocompatibility.

Table 5.3 Summary of tensile strength and toughness of PAAm single polymer hydrogels and comparison with this co-polymer hydrogel and bovine cartilage

Method		Tensile Strength (MPs)	Compressive Strength (MPa)	Toughness (kJ m^{-3})	References
Molding	PAAm/Agar	1	38	9000	[18]
	PAAm/PAMPS	0.819	60	3300	[201, 202]
3D Printing	PAAm/PAMPS	1.417	61.9	1060	[26]
	PAAm/Agar	0.402	-	2180	[137]
	PAAm/Agar/Alginate	1.09	40	1610	[137]
	PAAm/Alginate	0.25	-	154	[6]
	PA-AAm copolymer	4.4	21.2	6000	This work
	Bovine Knee joint Cartilage	0.53-9	14-59	-	[7]

5.4 Summary

In conclusion, this research demonstrated a facile approach to 3D print a PA: AAm based single network copolymer hydrogel. The synergistic effect of the hydrophobic (PA) and hydrophilic (AAm) components induced a significant increase in tensile strength (~4.4 MPa), compressive strength (~20 MPa) and toughness (~6000 kJ m^{-3}). The results are superior to a great number of 3D printed hydrogels. The hydrogel performance can be further improved by regulating the periodicity of the hydrophobic and hydrophilic regions in the copolymers in the printing process. More importantly, this method can be extended

to other high-performance copolymers to construct super-strong hydrogels and thus pave the way to future 3D printing of load-bearing tissues like meniscus.

CHAPTER VI

CONCLUSION AND FUTURE WORK

6.1 Conclusion

Direct ink writing (DIW) is a fast-developing technology that has gained the spotlight in recent decades. DIW shares the common advantages of 3D printing including the geometric flexibility, free-of-mold in fabrication, and can reduce the waste of materials as well as lead-time, which is suitable for emergency request. For polymeric materials printing, DIW expands the printable polymer materials to thermal curable or photo curable liquid, gel or paste, and can fabricate objects at different scales. In DIW, the ink is extruded out of the nozzle with controlled flow rate and deposited along the print path to form 3D structures. The fundamentals of 3D printing technology lie in the material availability and process capability for different applications. Compared to other printing modalities including stereolithography (SLA), fused filament fabrication (FFF) and etc., DIW is a simple process with ease-of-accessibility, which can be modified with other advanced process for functional materials fabrication.

One major challenge of DIW is the inferior mechanical of the printed parts compared to conventional manufacturing process. With the material advances, improved mechanical performance for printed parts and advanced manufacturing process can be realized with various applications. In this dissertation, frontal curing enabled DIW of epoxy-based and DCPD-based thermosetting polymers and composites for structural applications, as well as DIW of super strong hydrogel for medical applications were studied.

Firstly, frontal curing enabled DIW printing process is a promising method for thermosetting polymers and composites fabrication with low energy consumption. Mechanically strong, thermally and chemically inert epoxy resins with large market revenue ($8 Billion USD in 2020) was selected as the matrix material for frontal curing enable DIW printing. To realize frontal curable enabled DIW printing, the effect of I-TI and I-Al (the initiating system) on the frontal reaction kinetics were analyzed and their concentrations were adjusted for controlling the frontal propagation behavior. Reducing the I-Al concentration can effectively lower the front reaction temperature and I-TI are less effective in tuning the front propagation behavior. With the incorporation of 4mol% I-TI and 0.05 mol% I-Al, the front temperature can be reduced to ~240°C. Nano-/micro-fillers were added in the epoxy resin system as catalyst to tune the reaction kinetics and further reduce the front temperature. With the addition of 1 wt% CNT, the front temperature was reduced to ~227°C and front velocity was remained. The reaction profiles of inks were analyzed for cure kinetics analysis. The left shift of CNT incorporated inks' reaction profiles indicated a lower reaction energy required compared to the neat resins. The activation energy was reduced with the CNT incorporation, which further proves its catalytic function in frontal curing reaction in current resin systems. Besides, the proposed inks were used for c-CFRCs fabrication with a high level of flexibility. The printed c-CFRCs exhibited a tensile strength of ~1.147 GPa, far exceeding the 3D printed thermoplastic based c-CFRCs, and it is comparable to other thermosets-based c-CFRCs. The as-printed c-CFRCs exhibited high tensile strength suitable for high-performance structural applications. The rapid and free-form printing capabilities showed great promise

in industrial production. Notably, by generalizing the energy-efficient frontal curing and printing method to a more commonly used epoxy resins and composites fabrication, potentially 3.6 billion kilowatt-hours/year of energy could be saved. The successful demonstration of frontal curing enabled DIW of epoxy and composites revolutionize the epoxy production industry and make the realization of autonomous production foreseeable.

Secondly, DCPD is one type of thermosetting polymer that is suitable for frontal propagation with the presence of highly efficient ruthenium Grubbs'-type II (GC2) catalyst. Its short carbon fiber composites were printed via frontal polymerization. Short carbon fiber with hydroxyl, norbornene groups were synthesized and compared to non-functionalized ones. The effect of surface modification on tensile properties were examined for the printed parts. The tensile strength of the printed norbornene-CF composites was around 43.3MPa, which was 170% higher than printed neat DCPD resin and 32% higher than as-received sized-fiber/DCPD composites. The toughness of the printed composites was ~14 MPa, ~33.3% higher than printed sizing CF/DCPD composites. Moreover, the interlayer bonding strength of printed norbornene carbon fiber composites was 9.31 MPa, which was 255% higher compared to neat DCPD. The aforementioned experimental results demonstrated the effectiveness of adopting norbornene functionalized CF in enhancing the mechanical performance of printed DCPD composites.

Lastly, a super strong printable hydrogel was designed and fabricated for load-bearing tissue applications. A new ink is designed for the 3D printing process with a single

polymer network consisting of both stiff and soft components. The synergistic effect of the stiff and soft components in the polymer chain helps improve the mechanical properties of the 3D printing hydrogel. And the single network facilitates the printing process with one-step crosslinking comparing to other 3D printed DN hydrogels with multiple printing and crosslinking process and inferior mechanical performance. A meniscus shape was printed and underwent the dimensional check to study the effect of solvent exchange process on dimensional accuracy. The printed parts showed an adequate dimensional accuracy. The printed meniscus shape with an overall dimension of ~50mm by ~40mm by ~10mm exhibited a ~0.4mm difference in XY direction, 1.5 mm difference in height.

6.2 Future Work

1. The stability of frontal curing enabled printing process with I-Al/I-TI initiators and CNT catalyst incorporated epoxy resins systems will be investigated. The factors that drive the frontal propagation stability need to be determined and their relationships need to be understood for controllable propagation and printing. Mitigating the propagation instability will also help to improve the un-uniform crosslinking of the printed parts.

2. Further investigation over the process parameters is needed for reliable prints. Digital twin model can be developed for determining the optimal printing process parameters for different shapes and different material formulations.

3. More efficient frontal curing system with new initiating systems needs further investigation. Single initiator with low cost and high initiation efficiency is desirable. The

mechanism of the frontal curing process and the effect of molecular structure on the frontal curing process need further exploration, which helps to find the new initiating systems. The exploration process is labor-intensive in the traditional experimental way, while machine learning assisted search in complement to the traditional search will be employed for the new material discovery with ease and low cost.

4. Biocompatibility of the printed hydrogel will be further studied for its feasibility in in-vitro and/or in-vivo applications. Besides, further reducing the dimensional effect of solvent exchange process on the printing accuracy is needed.

REFERENCES

1. Fiorina, M.; Seman, A.; Castanié, B.; Ali, K. M.; Schwob, C.; Mezeix, L., Spring-in prediction for carbon/epoxy aerospace composite structure. *Composite Structures* **2017,** *168*, 739-745.

2. Jakubinek, M. B.; Ashrafi, B.; Zhang, Y.; Martinez-Rubi, Y.; Kingston, C. T.; Johnston, A.; Simard, B., Single-walled carbon nanotube–epoxy composites for structural and conductive aerospace adhesives. *Composites Part B: Engineering* **2015,** *69*, 87-93.

3. Liu, T.; Zhang, M.; Guo, X.; Liu, C.; Liu, T.; Xin, J.; Zhang, J., Mild chemical recycling of aerospace fiber/epoxy composite wastes and utilization of the decomposed resin. *Polymer Degradation and Stability* **2017,** *139*, 20-27.

4. Liu, Y.; Wilkinson, A., Rheological percolation behaviour and fracture properties of nanocomposites of MWCNTs and a highly crosslinked aerospace-grade epoxy resin system. *Composites Part A: Applied Science and Manufacturing* **2018,** *105*, 97-107.

5. May, C., *Epoxy resins: chemistry and technology*. Routledge: 2018.

6. Polydoropoulou, P. V.; Katsiropoulos, C. V.; Pantelakis, S. G., The synergistic effect of CNTs and flame retardants on the mechanical behavior of aerospace epoxy resin. *Polymer Engineering & Science* **2017,** *57* (5), 528-536.

7. Pascault, J. P.; Williams, R. J. J., Overview of thermosets: present and future. In *Thermosets*, Elsevier: 2018; pp 3-34.

8. Campana, C.; Léger, R.; Sonnier, R.; Ferry, L.; Ienny, P., Effect of post curing temperature on mechanical properties of a flax fiber reinforced epoxy composite. *Composites Part A: Applied Science and Manufacturing* **2018,** *107*, 171-179.

9. Moreno, M.; Armentano, I.; Fortunati, E.; Mattioli, S.; Torre, L.; Lligadas, G.; Ronda, J. C.; Galià, M.; Cádiz, V., Cellulose nano-biocomposites from high oleic sunflower oil-derived thermosets. *European Polymer Journal* **2016,** *79*, 109-120.

10. Timmis, A. J.; Hodzic, A.; Koh, L.; Bonner, M.; Soutis, C.; Schäfer, A. W.; Dray, L., Environmental impact assessment of aviation emission reduction through the implementation of composite materials. *The International Journal of Life Cycle Assessment* **2015,** *20* (2), 233-243.

11. Timothy Brindle, J. N., Darren L. Johnson, The Meniscus: Review of Basic Principles With Application to Surgery and Rehabilitation. *Journal of Athletic Training* **2001,** *36* (2), 10.

12. Packer, J. D.; Rodeo, S. A., Meniscal Allograft Transplantation. *Clinics in Sports Medicine* **2009,** *28* (2), 259-+.

13. A. J. Schoenfeld, W. J. L., D. B. Kay, Tissue-engineered meniscal constructs. *American Journal of Orthopedics* **2007,** *36* (11), 7.

14. Zhang, Z.; Wu, Q.; Zeng, L.; Wang, S. In *Modeling-Based Assessment of 3D Printing-Enabled Meniscus Transplantation*, 2019; Multidisciplinary Digital Publishing Institute: p 69.

15. Gao, G.; Du, G.; Cheng, Y.; Fu, J., Tough nanocomposite double network hydrogels reinforced with clay nanorods through covalent bonding and reversible chain adsorption. *Journal of Materials Chemistry B* **2014,** *2* (11), 1539-1548.

16. Liu, R.; Liang, S.; Tang, X.-Z.; Yan, D.; Li, X.; Yu, Z.-Z., Tough and highly stretchable graphene oxide/polyacrylamide nanocomposite hydrogels. *Journal of Materials Chemistry* **2012,** *22* (28), 14160-14167.

17. Miyazaki, S.; Endo, H.; Karino, T.; Haraguchi, K.; Shibayama, M., Gelation mechanism of poly (N-isopropylacrylamide)− clay nanocomposite gels. *Macromolecules* **2007,** *40* (12), 4287-4295.

18. Chen, Q.; Zhu, L.; Zhao, C.; Wang, Q.; Zheng, J., A robust, one‐pot synthesis of highly mechanical and recoverable double network hydrogels using thermoreversible sol‐gel polysaccharide. *Advanced materials* **2013,** *25* (30), 4171-4176.

19. Gong, J. P.; Katsuyama, Y.; Kurokawa, T.; Osada, Y., Double‐network hydrogels with extremely high mechanical strength. *Advanced Materials* **2003,** *15* (14), 1155-1158.

20. Sun, J. Y.; Zhao, X.; Illeperuma, W. R.; Chaudhuri, O.; Oh, K. H.; Mooney, D. J.; Vlassak, J. J.; Suo, Z., Highly stretchable and tough hydrogels. *Nature* **2012,** *489* (7414), 133-6.

21. Okumura, Y.; Ito, K., The polyrotaxane gel: A topological gel by figure‐of‐eight cross‐links. *Advanced materials* **2001,** *13* (7), 485-487.

22. Fleury, G.; Schlatter, G.; Brochon, C.; Hadziioannou, G., From high molecular weight precursor polyrotaxanes to supramolecular sliding networks. The 'sliding gels'. *Polymer* **2005,** *46* (19), 8494-8501.

23. Chimene, D.; Peak, C. W.; Gentry, J. L.; Carrow, J. K.; Cross, L. M.; Mondragon, E.; Cardoso, G. B.; Kaunas, R.; Gaharwar, A. K., Nanoengineered Ionic-Covalent Entanglement (NICE) Bioinks for 3D Bioprinting. *ACS Appl Mater Interfaces* **2018,** *10* (12), 9957-9968.

24. Bakarich, S. E.; Beirne, S.; Wallace, G. G.; Spinks, G. M., Extrusion printing of ionic–covalent entanglement hydrogels with high toughness. *Journal of Materials Chemistry B* **2013,** *1* (38), 4939-4946.

25. Haque, M. A.; Kurokawa, T.; Gong, J. P., Super tough double network hydrogels and their application as biomaterials. *Polymer* **2012,** *53* (9), 1805-1822.

26. Yang, F.; Tadepalli, V.; Wiley, B. J., 3D Printing of a Double Network Hydrogel with a Compression Strength and Elastic Modulus Greater than those of Cartilage. *ACS Biomaterials Science & Engineering* **2017,** *3* (5), 863-869.

27. Chen, Q.; Chen, H.; Zhu, L.; Zheng, J., Fundamentals of double network hydrogels. *Journal of Materials Chemistry B* **2015,** *3* (18), 3654-3676.

28. Hull, C. W., Apparatus for production of three-dimensional objects by stereolithography. Google Patents: 1986.

29. Rengier, F.; Mehndiratta, A.; von Tengg-Kobligk, H.; Zechmann, C. M.; Unterhinninghofen, R.; Kauczor, H. U.; Giesel, F. L., 3D printing based on imaging data: review of medical applications. *International Journal of Computer Assisted Radiology and Surgery* **2010,** *5* (4), 335-341.

30. Ligon, S. C.; Liska, R.; Stampfl, J.; Gurr, M.; Mülhaupt, R., Polymers for 3D printing and customized additive manufacturing. *Chemical reviews* **2017,** *117* (15), 10212-10290.

31. Ming, Y.; Duan, Y.; Wang, B.; Xiao, H.; Zhang, X., A novel route to fabricate high-performance 3D printed continuous fiber-reinforced thermosetting polymer composites. *Materials* **2019,** *12* (9), 1369.

32. Aumnate, C.; Pongwisuthiruchte, A.; Pattananuwat, P.; Potiyaraj, P., Fabrication of ABS/graphene oxide composite filament for fused filament fabrication (FFF) 3D printing. *Advances in Materials Science and engineering* **2018,** *2018*.

33. Butt, J.; Bhaskar, R., Investigating the Effects of Annealing on the Mechanical Properties of FFF-Printed Thermoplastics. *Journal of Manufacturing and Materials Processing* **2020,** *4* (2), 38.

34. Skornyakov, I. A.; Tarasova, T. V.; Terekhina, S. M., Investigation of the strength characteristics of samples made of nylon by FFF technology. *ARPN Journal of Engineering and Applied Sciences* **2019,** *14* (13), 2427-2432.

35. Lee, K.-Y.; Cho, J.-W.; Chang, N.-Y.; Chae, J.-M.; Kang, K.-H.; Kim, S.-C.; Cho, J.-H., Accuracy of three-dimensional printing for manufacturing replica teeth. *Korean journal of orthodontics* **2015,** *45* (5), 217.

36. Datta, P.; Ayan, B.; Ozbolat, I. T., Bioprinting for vascular and vascularized tissue biofabrication. *Acta Biomaterialia*.

37. Visscher, D. O.; Farré-Guasch, E.; Helder, M. N.; Gibbs, S.; Forouzanfar, T.; van Zuijlen, P. P.; Wolff, J., Advances in bioprinting technologies for craniofacial reconstruction. *Trends in biotechnology* **2016,** *34* (9), 700-710.

38. Robertson, I. D.; Yourdkhani, M.; Centellas, P. J.; Aw, J. E.; Ivanoff, D. G.; Goli, E.; Lloyd, E. M.; Dean, L. M.; Sottos, N. R.; Geubelle, P. H.; Moore, J. S.; White, S. R., Rapid energy-efficient manufacturing of polymers and composites via frontal polymerization. *Nature* **2018,** *557* (7704), 223-227.

39. Anguita, J. V.; Smith, C. T. G.; Stute, T.; Funke, M.; Delkowski, M.; Silva, S. R. P., Dimensionally and environmentally ultra-stable polymer composites reinforced with carbon fibres. *Nat Mater* **2020,** *19* (3), 317-322.

40. Chen, Z.; Chisholm, B.; Kim, J.; Stafslien, S.; Wagner, R.; Patel, S.; Daniels, J.; Wal, L. V.; Li, J.; Ward, K., UV‐curable, oxetane‐toughened epoxy‐siloxane coatings for marine fouling‐release coating applications. *Polymer international* **2008,** *57* (6), 879-886.

41. Han, W.; Chen, S.; Campbell, J.; Zhang, X.; Tang, Y., Fracture toughness and wear properties of nanosilica/epoxy composites under marine environment. *Materials Chemistry and Physics* **2016,** *177*, 147-155.

42. Janvier, M.; Hollande, L.; Jaufurally, A. S.; Pernes, M.; Ménard, R.; Grimaldi, M.; Beaugrand, J.; Balaguer, P.; Ducrot, P. H.; Allais, F., Syringaresinol: A Renewable and Safer Alternative to Bisphenol A for Epoxy‐Amine Resins. *ChemSusChem* **2017,** *10* (4), 738-746.

43. Martí, M.; Armelin, E.; Iribarren, J. I.; Alemán, C., Soluble polythiophenes as anticorrosive additives for marine epoxy paints. *Materials and Corrosion* **2015,** *66* (1), 23-30.

44. Mazzon, E.; Habas-Ulloa, A.; Habas, J.-P., Lightweight rigid foams from highly reactive epoxy resins derived from vegetable oil for automotive applications. *European Polymer Journal* **2015,** *68*, 546-557.

45. Chen, J.; Lekawa-Raus, A.; Trevarthen, J.; Gizewski, T.; Lukawski, D.; Hazra, K.; Rahatekar, S. S.; Koziol, K. K. K., Carbon nanotube films spun from a gas phase reactor for manufacturing carbon nanotube film/carbon fibre epoxy hybrid composites for electrical applications. *Carbon* **2020,** *158*, 282-290.

46. de Luzuriaga, A. R.; Martin, R.; Markaide, N.; Rekondo, A.; Cabanero, G.; Rodriguez, J.; Odriozola, I., Epoxy resin with exchangeable disulfide crosslinks to obtain reprocessable, repairable and recyclable fiber-reinforced thermoset composites. *Materials Horizons* **2016,** *3* (3), 241-247.

47. Gu, J.; Yang, X.; Lv, Z.; Li, N.; Liang, C.; Zhang, Q., Functionalized graphite nanoplatelets/epoxy resin nanocomposites with high thermal conductivity. *International Journal of Heat and Mass Transfer* **2016,** *92*, 15-22.

48. Luo, H.; Zhang, D.; Jiang, C.; Yuan, X.; Chen, C.; Zhou, K., Improved dielectric properties and energy storage density of poly (vinylidene fluoride-co-hexafluoropropylene) nanocomposite with hydantoin epoxy resin coated BaTiO3. *ACS applied materials & interfaces* **2015,** *7* (15), 8061-8069.

49. Beda, A.; Taberna, P.-L.; Simon, P.; Ghimbeu, C. M., Hard carbons derived from green phenolic resins for Na-ion batteries. *Carbon* **2018,** *139*, 248-257.

50. Deng, P.; Shi, Y.; Liu, Y.; Liu, Y.; Wang, Q., Solidifying process and flame retardancy of epoxy resin cured with boron-containing phenolic resin. *Applied Surface Science* **2018,** *427*, 894-904.

51. Foyer, G.; Chanfi, B. H.; Boutevin, B.; Caillol, S.; David, G., New method for the synthesis of formaldehyde-free phenolic resins from lignin-based aldehyde precursors. *European Polymer Journal* **2016,** *74*, 296-309.

52. Shudo, Y.; Izumi, A.; Hagita, K.; Nakao, T.; Shibayama, M., Structure-mechanical property relationships in crosslinked phenolic resin investigated by molecular dynamics simulation. *Polymer* **2017,** *116*, 506-514.

53. Ohashi, S.; Pandey, V.; Arza, C. R.; Froimowicz, P.; Ishida, H., Simple and low energy consuming synthesis of cyanate ester functional naphthoxazines and their properties. *Polymer Chemistry* **2016,** *7* (12), 2245-2252.

54. Uhlig, C.; Bauer, M.; Bauer, J.; Kahle, O.; Taylor, A. C.; Kinloch, A. J., Influence of backbone structure, conversion and phenolic co-curing of cyanate esters on side relaxations, fracture toughness, flammability properties and water uptake and toughening with low molecular weight polyethersulphones. *Reactive and Functional Polymers* **2018,** *129*, 2-22.

55. Arslan, M.; Kiskan, B.; Yagci, Y., Benzoxazine-based thermosets with autonomous self-healing ability. *Macromolecules* **2015,** *48* (5), 1329-1334.

56. Arslan, M.; Motallebzadeh, A.; Kiskan, B.; Demirel, A. L.; Kumbaraci, I. V.; Yagci, Y., Combining benzoxazine and ketene chemistries for self-healing of high performance thermoset surfaces. *Polymer Chemistry* **2018,** *9* (15), 2031-2039.

57. Deliballi, Z.; Kiskan, B.; Yagci, Y., Main-chain benzoxazine precursor block copolymers. *Polymer Chemistry* **2018,** *9* (2), 178-183.

58. Iredale, R. J.; Ward, C.; Hamerton, I., Modern advances in bismaleimide resin technology: a 21st century perspective on the chemistry of addition polyimides. *Progress in Polymer Science* **2017,** *69*, 1-21.

59. Ding, Z.; Yuan, L.; Guan, Q.; Gu, A.; Liang, G., A reconfiguring and self-healing thermoset epoxy/chain-extended bismaleimide resin system with thermally dynamic covalent bonds. *Polymer* **2018,** *147*, 170-182.

60. Lipson, H.; Kurman, M., *Fabricated: The new world of 3D printing*. John Wiley & Sons: 2013.

61. Roller, M. B., Rheology of curing thermosets: a review. *Polymer Engineering & Science* **1986,** *26* (6), 432-440.

62. Compton, B. G.; Lewis, J. A., 3D-printing of lightweight cellular composites. *Adv Mater* **2014,** *26* (34), 5930-5.

63. Chandrasekaran, S.; Duoss, E. B.; Worsley, M. A.; Lewicki, J. P., 3D printing of high performance cyanate ester thermoset polymers. *Journal of Materials Chemistry A* **2018,** *6* (3), 853-858.

64. Zarek, M.; Layani, M.; Cooperstein, I.; Sachyani, E.; Cohn, D.; Magdassi, S., 3D Printing of Shape Memory Polymers for Flexible Electronic Devices. *Adv Mater* **2016,** *28* (22), 4449-54.

65. Hegde, M.; Meenakshisundaram, V.; Chartrain, N.; Sekhar, S.; Tafti, D.; Williams, C. B.; Long, T. E., 3D Printing All-Aromatic Polyimides using Mask-Projection Stereolithography: Processing the Nonprocessable. *Adv Mater* **2017,** *29* (31).

66. Kuang, X.; Zhao, Z.; Chen, K.; Fang, D.; Kang, G.; Qi, H. J., High-Speed 3D Printing of High-Performance Thermosetting Polymers via Two-Stage Curing. *Macromolecular Rapid Communications* **2018,** *39* (7).

67. Zhang, B.; Kowsari, K.; Serjouei, A.; Dunn, M. L.; Ge, Q., Reprocessable thermosets for sustainable three-dimensional printing. *Nat Commun* **2018,** *9* (1), 1831.

68. Sun, H.; Kim, Y.; Kim, Y. C.; Park, I. K.; Suhr, J.; Byun, D.; Choi, H. R.; Kuk, K.; Baek, O. H.; Jung, Y. K.; Choi, H. J.; Kim, K. J.; Nam, J. D., Self-standing and shape-memorable UV-curing epoxy polymers for three-dimensional (3D) continuous-filament printing. *Journal of Materials Chemistry C* **2018,** *6* (12), 2996-3003.

69. Yang, K.; Grant, J. C.; Lamey, P.; Joshi-Imre, A.; Lund, B. R.; Smaldone, R. A.; Voit, W., Diels-Alder Reversible Thermoset 3D Printing: Isotropic Thermoset Polymers via Fused Filament Fabrication. *Advanced Functional Materials* **2017,** *27* (24).

70. Sperling, L. H., *Introduction to physical polymer science*. John Wiley & Sons: 2005.

71. Kuang, X.; Zhao, Z.; Chen, K.; Fang, D.; Kang, G.; Qi, H. J., High-Speed 3D Printing of High-Performance Thermosetting Polymers via Two-Stage Curing. *Macromol Rapid Commun* **2018,** *39* (7), e1700809.

72. Shi, Q.; Yu, K.; Kuang, X.; Mu, X.; Dunn, C. K.; Dunn, M. L.; Wang, T.; Jerry Qi, H., Recyclable 3D printing of vitrimer epoxy. *Materials Horizons* **2017,** *4* (4), 598-607.

73. Ngo, T. D.; Kashani, A.; Imbalzano, G.; Nguyen, K. T. Q.; Hui, D., Additive manufacturing (3D printing): A review of materials, methods, applications and challenges. *Composites Part B: Engineering* **2018,** *143*, 172-196.

74. Lewicki, J. P.; Rodriguez, J. N.; Zhu, C.; Worsley, M. A.; Wu, A. S.; Kanarska, Y.; Horn, J. D.; Duoss, E. B.; Ortega, J. M.; Elmer, W.; Hensleigh, R.; Fellini, R. A.; King, M. J., 3D-Printing of Meso-structurally Ordered Carbon Fiber/Polymer Composites with Unprecedented Orthotropic Physical Properties. *Sci Rep* **2017,** *7*, 43401.

75. Jeong, W.; Kessler, M. R., Toughness enhancement in ROMP functionalized carbon nanotube/polydicyclopentadiene composites. *Chemistry of Materials* **2008,** *20* (22), 7060-7068.

76. Chechilo, N. M.; Khvilivitskii, R. J.; Enikolopyan, N. S. In *Propagation of the polymerization reaction*, 1972; pp 1180-1181.

77. Chekanov, Y.; Arrington, D.; Brust, G.; Pojman, J. A., Frontal curing of epoxy resins: Comparison of mechanical and thermal properties to batch‐cured materials. *Journal of applied polymer science* **1997,** *66* (6), 1209-1216.

78. Washington, R. P.; Steinbock, O., Frontal polymerization synthesis of temperature-sensitive hydrogels. *Journal of the American Chemical Society* **2001,** *123* (32), 7933-7934.

79. Chen, S.; Tian, Y.; Chen, L.; Hu, T., Epoxy resin/polyurethane hybrid networks synthesized by frontal polymerization. *Chemistry of materials* **2006,** *18* (8), 2159-2163.

80. Mariani, A.; Nuvoli, L.; Sanna, D.; Alzari, V.; Nuvoli, D.; Rassu, M.; Malucelli, G., Semi-interpenetrating polymer networks based on crosslinked poly(N

-isopropyl acrylamide) and methylcellulose prepared by frontal polymerization. *Journal of Polymer Science Part A: Polymer Chemistry* **2018,** *56* (4), 437-443.

81. Bomze, D.; Knaack, P.; Liska, R., Successful radical induced cationic frontal polymerization of epoxy-based monomers by C–C labile compounds. *Polymer Chemistry* **2015,** *6* (47), 8161-8167.

82. Goli, E.; Robertson, I. D.; Geubelle, P. H.; Moore, J. S., Frontal Polymerization of Dicyclopentadiene: A Numerical Study. *J Phys Chem B* **2018,** *122* (16), 4583-4591.

83. Robertson, I. D.; Pruitt, E. L.; Moore, J. S., Frontal Ring-Opening Metathesis Polymerization of Exo-Dicyclopentadiene for Low Catalyst Loadings. *ACS Macro Letters* **2016,** *5* (5), 593-596.

84. Mariani, A.; Fiori, S.; Chekanov, Y.; Pojman, J. A., Frontal ring-opening metathesis polymerization of dicyclopentadiene. *Macromolecules* **2001,** *34* (19), 6539-6541.

85. Ruiu, A.; Sanna, D.; Alzari, V.; Nuvoli, D.; Mariani, A., Advances in the frontal ring opening metathesis polymerization of dicyclopentadiene. *Journal of Polymer Science Part A: Polymer Chemistry* **2014,** *52* (19), 2776-2780.

86. Robertson, I. D.; Dean, L. M.; Rudebusch, G. E.; Sottos, N. R.; White, S. R.; Moore, J. S., Alkyl Phosphite Inhibitors for Frontal Ring-Opening Metathesis Polymerization Greatly Increase Pot Life. *ACS Macro Letters* **2017,** *6* (6), 609-612.

87. Klikovits, N.; Liska, R.; D'Anna, A.; Sangermano, M., Successful UV-Induced RICFP of Epoxy-Composites. *Macromolecular Chemistry and Physics* **2017,** *218* (18).

88. Mariani, A.; Bidali, S.; Fiori, S.; Sangermano, M.; Malucelli, G.; Bongiovanni, R.; Priola, A., UV‐ignited frontal polymerization of an epoxy resin. *Journal of Polymer Science Part A: Polymer Chemistry* **2004,** *42* (9), 2066-2072.

89. Sangermano, M.; D'Anna, A.; Marro, C.; Klikovits, N.; Liska, R., UV-activated frontal polymerization of glass fibre reinforced epoxy composites. *Composites Part B: Engineering* **2018,** *143*, 168-171.

90. Bomze, D.; Knaack, P.; Koch, T.; Jin, H.; Liska, R., Radical induced cationic frontal polymerization as a versatile tool for epoxy curing and composite production. *Journal of Polymer Science Part A: Polymer Chemistry* **2016,** *54* (23), 3751-3759.

91. Yang, C.; Tian, X.; Liu, T.; Cao, Y.; Li, D., 3D printing for continuous fiber reinforced thermoplastic composites: mechanism and performance. *Rapid Prototyping Journal* **2017,** *23* (1), 209-215.

92. Tian, X.; Liu, T.; Yang, C.; Wang, Q.; Li, D., Interface and performance of 3D printed continuous carbon fiber reinforced PLA composites. *Composites Part A: Applied Science and Manufacturing* **2016,** *88*, 198-205.

93. Li, N.; Li, Y.; Liu, S., Rapid prototyping of continuous carbon fiber reinforced polylactic acid composites by 3D printing. *Journal of Materials Processing Technology* **2016,** *238*, 218-225.

94. Tian, X.; Liu, T.; Wang, Q.; Dilmurat, A.; Li, D.; Ziegmann, G., Recycling and remanufacturing of 3D printed continuous carbon fiber reinforced PLA composites. *Journal of cleaner production* **2017,** *142*, 1609-1618.

95. Goh, G. D.; Yap, Y. L.; Agarwala, S.; Yeong, W. Y., Recent progress in additive manufacturing of fiber reinforced polymer composite. *Advanced Materials Technologies* **2019,** *4* (1), 1800271.

96. Hao, W.; Liu, Y.; Zhou, H.; Chen, H.; Fang, D., Preparation and characterization of 3D printed continuous carbon fiber reinforced thermosetting composites. *Polymer Testing* **2018,** *65*, 29-34.

97. Shi, B.; Shang, Y.; Zhang, P.; Cuadros, A. P.; Qu, J.; Sun, B.; Gu, B.; Chou, T.-W.; Fu, K. K., Dynamic capillary-driven additive manufacturing of continuous carbon fiber composite. *Matter* **2020,** *2* (6), 1594-1604.

98. Tran, A. D.; Koch, T.; Knaack, P.; Liska, R., Radical induced cationic frontal polymerization for preparation of epoxy composites. *Composites Part A: Applied Science and Manufacturing* **2020**, 105855.

99. Zhang, Z.; Wang, B.; Hui, D.; Qiu, J.; Wang, S., 3D bioprinting of soft materials-based regenerative vascular structures and tissues. *Composites Part B: Engineering* **2017,** *123*, 279-291.

100. Zhang, Y. S.; Khademhosseini, A., Advances in engineering hydrogels. *Science* **2017,** *356* (6337).

101. Fung, Y. C.; Liu, S. Q.; Zhou, J. B., Remodeling of the constitutive equation while a blood vessel remodels itself under stress. *Journal of biomechanical engineering* **1993,** *115* (4B), 453-459.

102. Nonoyama, T.; Gong, J. P., Double-network hydrogel and its potential biomedical application: A review. *Proceedings of the Institution of Mechanical Engineers, Part H: Journal of Engineering in Medicine* **2015,** *229* (12), 853-863.

103. Du, X.; Fu, S.; Zhu, Y., 3D printing of ceramic-based scaffolds for bone tissue engineering: an overview. *Journal of Materials Chemistry B* **2018,** *6* (27), 4397-4412.

104. Bilgen, B.; Jayasuriya, C. T.; Owens, B. D., Current Concepts in Meniscus Tissue Engineering and Repair. *Adv Healthc Mater* **2018,** *7* (11), e1701407.

105. Zhang, Z.; Jin, Y.; Yin, J.; Xu, C.; Xiong, R.; Christensen, K.; Ringeisen, B. R.; Chrisey, D. B.; Huang, Y., Evaluation of bioink printability for bioprinting applications. *Applied Physics Reviews* **2018,** *5* (4).

106. Li, X.; Wang, H.; Li, D.; Long, S.; Zhang, G.; Wu, Z., Dual Ionically Cross-linked Double-Network Hydrogels with High Strength, Toughness, Swelling Resistance, and Improved 3D Printing Processability. *ACS Appl Mater Interfaces* **2018,** *10* (37), 31198-31207.

107. Ozbolat, I. T.; Hospodiuk, M., Current advances and future perspectives in extrusion-based bioprinting. *Biomaterials* **2016,** *76*, 321-343.

108. Richards, D.; Jia, J.; Yost, M.; Markwald, R.; Mei, Y., 3D bioprinting for vascularized tissue fabrication. *Annals of biomedical engineering* **2017,** *45* (1), 132-147.

109. Khalil, S.; Sun, W., Biopolymer deposition for freeform fabrication of hydrogel tissue constructs. *Materials Science and Engineering: C* **2007,** *27* (3), 469-478.

110. Cohen, D. L.; Malone, E.; Lipson, H. O. D.; Bonassar, L. J., Direct freeform fabrication of seeded hydrogels in arbitrary geometries. *Tissue engineering* **2006,** *12* (5), 1325-1335.

111. Annabi, N.; Tamayol, A.; Uquillas, J. A.; Akbari, M.; Bertassoni, L. E.; Cha, C.; Camci‐Unal, G.; Dokmeci, M. R.; Peppas, N. A.; Khademhosseini, A., 25th anniversary article: rational design and applications of hydrogels in regenerative medicine. *Advanced Materials* **2014,** *26* (1), 85-124.

112. Yu, Y.; Zhang, Y.; Martin, J. A.; Ozbolat, I. T., Evaluation of cell viability and functionality in vessel-like bioprintable cell-laden tubular channels. *Journal of biomechanical engineering* **2013,** *135* (9), 091011.

113. Jia, W.; Gungor-Ozkerim, P. S.; Zhang, Y. S.; Yue, K.; Zhu, K.; Liu, W.; Pi, Q.; Byambaa, B.; Dokmeci, M. R.; Shin, S. R., Direct 3D bioprinting of perfusable vascular constructs using a blend bioink. *Biomaterials* **2016,** *106*, 58-68.

114. Gao, Q.; Liu, Z.; Lin, Z.; Qiu, J.; Liu, Y.; Liu, A.; Wang, Y.; Xiang, M.; Chen, B.; Fu, J.; He, Y., 3D Bioprinting of Vessel-like Structures with Multilevel Fluidic Channels. *ACS Biomaterials Science & Engineering* **2017**.

115. Bae, S.; Kim, H.; Lee, Y.; Xu, X.; Park, J.-S.; Zheng, Y.; Balakrishnan, J.; Lei, T.; Ri Kim, H.; Song, Y. I.; Kim, Y.-J.; Kim, K. S.; Ozyilmaz, B.; Ahn, J.-H.; Hong, B. H.; Iijima, S., Roll-to-roll production of 30-inch graphene films for transparent electrodes. *Nat Nano* **2010,** *5* (8), 574-578.

116. Best, C.; Onwuka, E.; Pepper, V.; Sams, M.; Breuer, J.; Breuer, C., Cardiovascular tissue engineering: preclinical validation to bedside application. *Physiology* **2016,** *31* (1), 7-15.

117. Arai, K.; Iwanaga, S.; Toda, H.; Genci, C.; Nishiyama, Y.; Nakamura, M., Three-dimensional inkjet biofabrication based on designed images. *Biofabrication* **2011,** *3* (3), 034113.

118. Beyer, S. T.; Bsoul, A.; Ahmadi, A.; Walus, K. In *3D alginate constructs for tissue engineering printed using a coaxial flow focusing microfluidic device*, 2013; IEEE: pp 1206-1209.

119. Bahk, J.-H.; Fang, H.; Yazawa, K.; Shakouri, A., Flexible thermoelectric materials and device optimization for wearable energy harvesting. *Journal of Materials Chemistry C* **2015,** *3* (40), 10362-10374.

120. Zhang, Y.; Yu, Y.; Ozbolat, I. T., Direct bioprinting of vessel-like tubular microfluidic channels. *Journal of nanotechnology in engineering and medicine* **2013,** *4* (2), 020902.

121. Ozbolat, I. T.; Chen, H.; Yu, Y., Development of 'Multi-arm Bioprinter'for hybrid biofabrication of tissue engineering constructs. *Robotics and Computer-Integrated Manufacturing* **2014,** *30* (3), 295-304.

122. Gao, Q.; He, Y.; Fu, J.-z.; Liu, A.; Ma, L., Coaxial nozzle-assisted 3D bioprinting with built-in microchannels for nutrients delivery. *Biomaterials* **2015,** *61*, 203-215.

123. Mandrycky, C.; Wang, Z.; Kim, K.; Kim, D.-H., 3D bioprinting for engineering complex tissues. *Biotechnology advances* **2016,** *34* (4), 422-434.

124. Murphy, S. V.; Atala, A., 3D bioprinting of tissues and organs. *Nat Biotech* **2014,** *32* (8), 773-785.

125. Attalla, R.; Ling, C.; Selvaganapathy, P., Fabrication and characterization of gels with integrated channels using 3D printing with microfluidic nozzle for tissue engineering applications. *Biomedical microdevices* **2016,** *18* (1), 1-12.

126. Tasoglu, S.; Demirci, U., Bioprinting for stem cell research. *Trends in biotechnology* **2013,** *31* (1), 10-19.

127. Xu, T.; Binder, K. W.; Albanna, M. Z.; Dice, D.; Zhao, W.; Yoo, J. J.; Atala, A., Hybrid printing of mechanically and biologically improved constructs for cartilage tissue engineering applications. *Biofabrication* **2012,** *5* (1), 015001.

128. Cui, X.; Breitenkamp, K.; Finn, M. G.; Lotz, M.; D'Lima, D. D., Direct human cartilage repair using three-dimensional bioprinting technology. *Tissue Engineering Part A* **2012,** *18* (11-12), 1304-1312.

129. Chia, H. N.; Wu, B. M., Recent advances in 3D printing of biomaterials. *Journal of biological engineering* **2015,** *9* (1), 4.

130. Guvendiren, M.; Lu, H. D.; Burdick, J. A., Shear-thinning hydrogels for biomedical applications. *Soft Matter* **2012,** *8* (2), 260-272.

131. Knowlton, S.; Joshi, A.; Yenilmez, B.; Ozbolat, I. T.; Chua, C. K.; Khademhosseini, A.; Tasoglu, S., Advancing cancer research using bioprinting for tumor-on-a-chip platforms. *International Journal of Bioprinting* **2016,** *2* (2).

132. Novosel, E. C.; Kleinhans, C.; Kluger, P. J., Vascularization is the key challenge in tissue engineering. *Advanced drug delivery reviews* **2011,** *63* (4), 300-311.

133. Ozbolat, I. T., Scaffold-based or scaffold-free bioprinting: competing or complementing approaches? *Journal of Nanotechnology in Engineering and Medicine* **2015,** *6* (2), 024701.

134. Stanton, M. M.; Samitier, J.; Sánchez, S., Bioprinting of 3D hydrogels. *Lab on a Chip* **2015,** *15* (15), 3111-3115.

135. Yu, Y.; Ozbolat, I. T. In *Tissue strands as "bioink" for scale-up organ printing*, 2014; IEEE: pp 1428-1431.

136. Hospodiuk, M.; Dey, M.; Sosnoski, D.; Ozbolat, I. T., The bioink: A comprehensive review on bioprintable materials. *Biotechnology advances* **2017**.

137. Wei, J.; Wang, J.; Su, S.; Wang, S.; Qiu, J.; Zhang, Z.; Christopher, G.; Ning, F.; Cong, W., 3D printing of an extremely tough hydrogel. *RSC Advances* **2015,** *5* (99), 81324-81329.

138. Bakarich, S. E.; Gorkin III, R.; in het Panhuis, M.; Spinks, G. M., Three-dimensional printing fiber reinforced hydrogel composites. *ACS applied materials & interfaces* **2014,** *6* (18), 15998-16006.

139. Rodriguez, M. J.; Brown, J.; Giordano, J.; Lin, S. J.; Omenetto, F. G.; Kaplan, D. L., Silk based bioinks for soft tissue reconstruction using 3-dimensional (3D) printing with in vitro and in vivo assessments. *Biomaterials* **2017,** *117*, 105-115.

140. Fedorovich, N. E.; Schuurman, W.; Wijnberg, H. M.; Prins, H.-J.; van Weeren, P. R.; Malda, J.; Alblas, J.; Dhert, W. J., Biofabrication of osteochondral tissue equivalents by printing topologically defined, cell-laden hydrogel scaffolds. *Tissue Engineering Part C: Methods* **2011,** *18* (1), 33-44.

141. Rutz, A. L.; Hyland, K. E.; Jakus, A. E.; Burghardt, W. R.; Shah, R. N., A multimaterial bioink method for 3D printing tunable, cell‐compatible hydrogels. *Advanced Materials* **2015,** *27* (9), 1607-1614.

142. Rezende, R. A.; Bártolo, P. J.; Mendes, A., Rheological behavior of alginate solutions for biomanufacturing. *Journal of applied polymer science* **2009,** *113* (6), 3866-3871.

143. Malda, J.; Visser, J.; Melchels, F. P.; Jüngst, T.; Hennink, W. E.; Dhert, W. J.; Groll, J.; Hutmacher, D. W., 25th anniversary article: engineering hydrogels for biofabrication. *Advanced materials* **2013,** *25* (36), 5011-5028.

144. Highley, C. B.; Rodell, C. B.; Burdick, J. A., Direct 3D printing of shear‐thinning hydrogels into self‐healing hydrogels. *Advanced Materials* **2015,** *27* (34), 5075-5079.

145. Tian, K.; Bae, J.; Bakarich, S. E.; Yang, C.; Gately, R. D.; Spinks, G. M.; Suo, Z.; Vlassak, J. J., 3D Printing of Transparent and Conductive Heterogeneous Hydrogel–Elastomer Systems. *Advanced Materials* **2017,** *29* (10).

146. Carvalho, C.; Landers, R.; Mülhaupt, R. In *Soft and Hard Implant Fabrication Using 3D-Bioplotting™ 732*, 2004.

147. Song, K.; Kim, K.; Hong, D.; Kim, J.; Heo, C. E.; Kim, H. I.; Hong, S. H., Highly active ruthenium metathesis catalysts enabling ring-opening metathesis polymerization of cyclopentadiene at low temperatures. *Nature Communications* **2019,** *10* (1), 3860.

148. Knaack, P.; Klikovits, N.; Tran, A. D.; Bomze, D.; Liska, R., Radical induced cationic frontal polymerization in thin layers. *Journal of Polymer Science Part A: Polymer Chemistry* **2019,** *57* (11), 1155-1159.

149. Liu, Y.; Phillips, B.; Li, W.; Zhang, Z.; Fang, L.; Qiu, J.; Wang, S., Fullerene-tailored graphene oxide interlayer spacing for energy-efficient water desalination. *ACS Applied Nano Materials* **2018,** *1* (11), 6168-6175.

150. Lu, L.; Xia, L.; Zengheng, H.; Xingyue, S.; Yi, Z.; Pan, L., Investigation on cure kinetics of epoxy resin containing carbon nanotubes modified with hyper-branched polyester. *RSC Advances* **2018,** *8* (52), 29830-29839.

151. Pojman, J. A.; Ilyashenko, V. M.; Khan, A. M., Free-radical frontal polymerization: self-propagating thermal reaction waves. *Journal of the Chemical Society, Faraday Transactions* **1996,** *92* (16), 2825-2837.

152. Yang, G.; Lee, J. K., Curing kinetics and mechanical properties of endo-dicyclopentadiene synthesized using different Grubbs' catalysts. *Industrial & Engineering Chemistry Research* **2014,** *53* (8), 3001-3011.

153. Zhang, S.; Xia, M.; Zhao, S.; Xu, T.; Zhang, E., Specific heat of single-walled carbon nanotubes. *Physical Review B* **2003,** *68* (7), 075415.

154. Arutiunian, K. A.; Davtyan, S. P.; Rozenberg, B. A.; Enikolopyan, N. S. In *Curing of epoxy resins of bis-phenol a by amines under conditions of reaction front propagation*, 1975; pp 657-660.

155. Surkov, N. F.; Davtyan, S. P.; Rozenberg, B. A.; Enikolopyan, N. S. In *Calculation of the steady velocity of the reaction front during hardening of epoxy oligomers by diamines*, 1976; pp 435-438.

156. Ivankovic, M.; Incarnato, L.; Kenny, J. M.; Nicolais, L., Curing kinetics and chemorheology of epoxy/anhydride system. *Journal of Applied Polymer Science* **2003,** *90* (11), 3012-3019.

157. Zhang, B.; Kowsari, K.; Serjouei, A.; Dunn, M. L.; Ge, Q., Reprocessable thermosets for sustainable three-dimensional printing. *Nature communications* **2018,** *9* (1), 1-7.

158. Shi, Q.; Yu, K.; Kuang, X.; Mu, X.; Dunn, C. K.; Dunn, M. L.; Wang, T.; Qi, H. J., Recyclable 3D printing of vitrimer epoxy. *Materials Horizons* **2017,** *4* (4), 598-607.

159. Yang, K.; Grant, J. C.; Lamey, P.; Joshi‐Imre, A.; Lund, B. R.; Smaldone, R. A.; Voit, W., Diels‐Alder reversible thermoset 3D printing: isotropic thermoset

polymers via fused filament fabrication. *Advanced Functional Materials* **2017,** *27* (24), 1700318.

160. Chen, K.; Kuang, X.; Li, V.; Kang, G.; Qi, H. J., Fabrication of tough epoxy with shape memory effects by UV-assisted direct-ink write printing. *Soft Matter* **2018,** *14* (10), 1879-1886.

161. Compton, B. G.; Lewis, J. A., 3D‐printing of lightweight cellular composites. *Advanced materials* **2014,** *26* (34), 5930-5935.

162. Matsuzaki, R.; Ueda, M.; Namiki, M.; Jeong, T.-K.; Asahara, H.; Horiguchi, K.; Nakamura, T.; Todoroki, A.; Hirano, Y., Three-dimensional printing of continuous-fiber composites by in-nozzle impregnation. *Scientific reports* **2016,** *6*, 23058.

163. resources., H. C. D., https://www.hexcel.com/user_area/content_media/raw/HexPly_85517_us_DataSheet.pdf . accessed on October 27, 2020.

164. Shi, B.; Shang, Y.; Zhang, P.; Cuadros, A. P.; Qu, J.; Sun, B.; Gu, B.; Chou, T.-W.; Fu, K., Dynamic Capillary-Driven Additive Manufacturing of Continuous Carbon Fiber Composite. *Matter* **2020,** *2* (6), 1594-1604.

165. van de Werken, N.; Hurley, J.; Khanbolouki, P.; Sarvestani, A. N.; Tamijani, A. Y.; Tehrani, M., Design considerations and modeling of fiber reinforced 3D printed parts. *Composites Part B: Engineering* **2019,** *160*, 684-692.

166. Van Der Klift, F.; Koga, Y.; Todoroki, A.; Ueda, M.; Hirano, Y.; Matsuzaki, R., 3D printing of continuous carbon fibre reinforced thermo-plastic (CFRTP) tensile test specimens. *Open Journal of Composite Materials* **2016,** *6* (01), 18.

167. Yang, C.; Tian, X.; Liu, T.; Cao, Y.; Li, D., 3D printing for continuous fiber reinforced thermoplastic composites: mechanism and performance. *Rapid Prototyping Journal* **2017**.

168. Sunter, D.; Morrow Iii, W. R.; Cresko, J. W.; Liddell, H. P. H. In *The manufacturing energy intensity of carbon fiber reinforced polymer composites and its effect on life cycle energy use for vehicle door lightweighting*, 2015.

169. *Plastic Market Size, Share & Trends Analysis Report By Product (PE, PP, PU, PVC, PET, Polystyrene, ABS, PBT, PPO, Epoxy Polymers, LCP, PC, Polyamide), By Application, By Region, And Segment Forecasts, 2020 - 2027*; 2020.

170. Sweeney, C. B.; Lackey, B. A.; Pospisil, M. J.; Achee, T. C.; Hicks, V. K.; Moran, A. G.; Teipel, B. R.; Saed, M. A.; Green, M. J., Welding of 3D-printed carbon

nanotube–polymer composites by locally induced microwave heating. *Science advances* **2017,** *3* (6), e1700262.

171. Zhang, B.; Kowsari, K.; Serjouei, A.; Dunn, M. L.; Ge, Q., Reprocessable thermosets for sustainable three-dimensional printing. *Nature communications* **2018,** *9* (1), 1831.

172. Esawi, A. M. K.; Morsi, K.; Sayed, A.; Taher, M.; Lanka, S., Effect of carbon nanotube (CNT) content on the mechanical properties of CNT-reinforced aluminium composites. *Composites Science and Technology* **2010,** *70* (16), 2237-2241.

173. Srivastava, V. K., Modeling and mechanical performance of carbon nanotube/epoxy resin composites. *Materials & Design* **2012,** *39*, 432-436.

174. Kaynak, C.; Orgun, O.; Tincer, T., Matrix and interface modification of short carbon fiber-reinforced epoxy. *Polymer Testing* **2005,** *24* (4), 455-462.

175. Zhao, Z.; Yang, Z.; Hu, Y.; Li, J.; Fan, X., Multiple functionalization of multi-walled carbon nanotubes with carboxyl and amino groups. *Applied surface science* **2013,** *276*, 476-481.

176. Castle, A. B.; Gracia-Espino, E.; Nieto-Delgado, C.; Terrones, H.; Terrones, M.; Hussain, S., Hydroxyl-functionalized and N-doped multiwalled carbon nanotubes decorated with silver nanoparticles preserve cellular function. *ACS nano* **2011,** *5* (4), 2458-2466.

177. Ramanathan, T.; Fisher, F. T.; Ruoff, R. S.; Brinson, L. C., Amino-functionalized carbon nanotubes for binding to polymers and biological systems. *Chemistry of Materials* **2005,** *17* (6), 1290-1295.

178. Wang, B.; Arias, K. F.; Zhang, Z.; Liu, Y.; Jiang, Z.; Sue, H.-J.; Currie-Gregg, N.; Bouslog, S.; Pei, Z. Z. J.; Wang, S., 3D printing of in-situ curing thermally insulated thermosets. *Manufacturing Letters* **2019**.

179. Zhang, Z.; Liu, R.; Zepeda, H.; Zeng, L.; Qiu, J.; Wang, S., 3D printing super strong hydrogel for artificial meniscus. *ACS Applied Polymer Materials* **2019,** *1* (8), 2023-2032.

180. Liu, Y.; Adronov, A., Preparation and utilization of catalyst-functionalized single-walled carbon nanotubes for ring-opening metathesis polymerization. *Macromolecules* **2004,** *37* (13), 4755-4760.

181. Bussy, C.; Pinault, M.; Cambedouzou, J.; Landry, M. J.; Jegou, P.; Mayne-l'Hermite, M.; Launois, P.; Boczkowski, J.; Lanone, S., Critical role of surface

chemical modifications induced by length shortening on multi-walled carbon nanotubes-induced toxicity. *Particle and fibre toxicology* **2012,** *9* (1), 1-15.

182. Zhang, R. L.; Zhang, J. S.; Zhao, L. H.; Sun, Y. L., Sizing agent on the carbon fibers surface and interface properties of its composites. *Fibers and Polymers* **2015,** *16* (3), 657-663.

183. Kamata, H.; Akagi, Y.; Kayasuga-Kariya, Y.; Chung, U.; Sakai, T., "Nonswellable" Hydrogel Without Mechanical Hysteresis. *Science* **2014,** *343* (6173), 873-875.

184. Cao, L. X.; Shi, X. Y.; Chang, H. S.; Zhang, Q. F.; He, Y. N., pH-dependent recognition of apoptotic and necrotic cells by the human dendritic cell receptor DEC205. *P Natl Acad Sci USA* **2015,** *112* (23), 7237-7242.

185. Rose, S.; Prevoteau, A.; Elziere, P.; Hourdet, D.; Marcellan, A.; Leibler, L., Nanoparticle solutions as adhesives for gels and biological tissues. *Nature* **2014,** *505* (7483), 382-+.

186. Sandring, S., Gray's Anatomy: The anatomical basis of clinical practice. *Elsevier Churchil Livingstone* **2009**, 5.

187. Freeman, M. E.; Furey, M. J.; Love, B. J.; Hampton, J. M., Friction, wear, and lubrication of hydrogels as synthetic articular cartilage. *Wear* **2000,** *241* (2), 129-135.

188. Mredha, M. T. I.; Pathak, S. K.; Tran, V. T.; Cui, J.; Jeon, I., Hydrogels with Superior Mechanical Properties from the Synergistic Effect in Hydrophobic–Hydrophilic Copolymers. *Chemical Engineering Journal* **2018**.

189. Li, H.; Tan, Y. J.; Leong, K. F.; Li, L., 3D Bioprinting of Highly Thixotropic Alginate/Methylcellulose Hydrogel with Strong Interface Bonding. *ACS Appl Mater Interfaces* **2017,** *9* (23), 20086-20097.

190. Palaganas, N. B.; Mangadlao, J. D.; de Leon, A. C. C.; Palaganas, J. O.; Pangilinan, K. D.; Lee, Y. J.; Advincula, R. C., 3D Printing of Photocurable Cellulose Nanocrystal Composite for Fabrication of Complex Architectures via Stereolithography. *ACS Appl Mater Interfaces* **2017,** *9* (39), 34314-34324.

191. Siqueira, G.; Kokkinis, D.; Libanori, R.; Hausmann, M. K.; Gladman, A. S.; Neels, A.; Tingaut, P.; Zimmermann, T.; Lewis, J. A.; Studart, A. R., Cellulose Nanocrystal Inks for 3D Printing of Textured Cellular Architectures. *Advanced Functional Materials* **2017,** *27* (12).

192. Wang, J.; Chiappone, A.; Roppolo, I.; Shao, F.; Fantino, E.; Lorusso, M.; Rentsch, D.; Dietliker, K.; Pirri, C. F.; Grützmacher, H., All - in - One Cellulose

Nanocrystals for 3D Printing of Nanocomposite Hydrogels. *Angewandte Chemie International Edition* **2018,** *57* (9), 2353-2356.

193. Wang, Q.; Sun, J.; Yao, Q.; Ji, C.; Liu, J.; Zhu, Q., 3D printing with cellulose materials. *Cellulose* **2018,** *25* (8), 4275-4301.

194. Darby, R.; Darby, R.; Chhabra, R. P., *Chemical engineering fluid mechanics, revised and expanded*. CRC Press: 2001.

195. Mezger, T. G., *The rheology handbook: for users of rotational and oscillatory rheometers*. Vincentz Network GmbH & Co KG: 2006.

196. Arimoto, H.; Egawa, M., Imaging wavelength and light penetration depth for water content distribution measurement of skin. *Skin Research and Technology* **2015,** *21* (1), 94-100.

197. Bhosale, A. M.; Richardson, J. B., Articular cartilage: structure, injuries and review of management. *British medical bulletin* **2008,** *87* (1), 77-95.

198. Iwasaki, T.; Kohinata, Y.; Nishide, H., Poly (thiaheterohelicene): a stiff conjugated helical polymer comprised of fused benzothiophene rings. *Organic letters* **2005,** *7* (5), 755-758.

199. Bakarich, S. E.; Panhuis, M. i. h.; Beirne, S.; Wallace, G. G.; Spinks, G. M., Extrusion printing of ionic–covalent entanglement hydrogels with high toughness. *Journal of Materials Chemistry B* **2013,** *1* (38).

200. Bakarich, S. E.; Balding, P.; Gorkin Iii, R.; Spinks, G. M., Printed ionic-covalent entanglement hydrogels from carrageenan and an epoxy amine. *RSC Advances* **2014,** *4* (72), 38088-38092.

201. Liang, J.; Shan, G.; Pan, P., Double network hydrogels with highly enhanced toughness based on a modified first network. *Soft Matter* **2017,** *13* (22), 4148-4158.

202. Gong, J. P., Why are double network hydrogels so tough? *Soft Matter* **2010,** *6* (12).

203. https://www.marketwatch.com/press-release/global-dicyclopentadiene-dcpd-market-size-in-2020-new-report-manufacturers-data-opportunity-import-export-scenario-application-top-countries-analysis-and-outlookshowing-impressive-growth-by-2026-2020-09-07.

204. https://www.polarismarketresearch.com/industry-analysis/epoxy-resins-market.

205. Yang, Y.; Li, L.; Pan, Y.; Sun, Z., Energy consumption modeling of stereolithography‐based additive manufacturing toward environmental sustainability. *Journal of Industrial Ecology* **2017,** *21* (S1), S168-S178.

APPENDIX A

PUBLICATIONS

Peer-reviewed journal papers

1. **Z. Zhang,** R. Liu, W. Li, Y. Liu, H. Luo, X. Zhang, J. Qiu, S. Wang, Energy-efficient additive manufacturing of thermosets and composites (submitted)
2. **Z. Zhang,** R. Liu, W. Li, Y. Liu, J. Qiu, S. Wang, Self-reinforced 3D printing carbon composites via frontal curing (submitted)
3. **Z. Zhang**, R. Liu, H. Zepeta, L. Zeng, J. Qiu, S. Wang, 3D Printing Super Strong Hydrogel for Artificial Meniscus. ACS Applied Polymer Materials, 1.8 (2019): 2023-2032
4. **Z. Zhang**, Q. Wu, L. Zeng, S. Wang, Modeling-Based Assessment of 3D Printing-Enabled Meniscus Transplantation. Healthcare, 7, (2019): 69-82
5. **Z. Zhang**, B. Wang, J. Qiu, S. Wang, Roll-to-roll printing of spatial wearable thermoelectrics, Manufacturing Letters, 21 (2019): 28-34
6. **Z. Zhang**, B. Wang, D. Hui, J. Qiu, S. Wang, 3D bioprinting of soft materials-based regenerative vascular structures and tissues, Composites Part B: Engineering, 123, (2017): 279-291
7. **Z. Zhang**, J. Qiu, S. Wang, Roll-to-Roll Printing of Flexible Thin-film Organic Thermoelectric Devices, Manufacturing Letters, 8, (2016): 6-10
8. L. Wang, **Z. Zhang**, Y. Liu, B. Wang, F. Lei, J. Qiu, K. Zhang, S. Wang, Exceptional thermoelectric properties of flexible organic/inorganic hybrids with monodispersed and periodic nanophase, **Nature Communication**, 9(1), (2018) 3817.
9. L. Wang, **Z. Zhang**, L. Geng, T. Yuan, Y. Liu, J. Guo, L. Fang, J. Qiu, S. Wang, Solution-printable flexible n-type thermoelectrics, **Energy & Environmental Science**, 11, (2018): 1307-1317
10. Y. Liu, **Z. Zhang,** W. Li, R. Liu, J. Qiu, S. Wang. Water purification performance and energy consumption of gradient nanocomposite membranes, Composites Part B: Engineering, (2020): 108426
11. Y. Liu, **Z. Zhang,** S. Wang. Carbon Nanopore-Tailored reverse osmotic water desalination, ACS ES&T Water, (2020)
12. B. Wang, **Z. Zhang,** S. Wang. Current Progress on the 3D Printing of Thermosets, Advanced Composites and Hybrid Materials (2020)
13. B. Wang, K. Arias, **Z. Zhang**, Y. Liu, Z. Jiang, H. Sue, L. Fang, S. Wang, In situ 3D printing of thermally insulated thermosets, Manufacturing Letters, (2019)

14. Y. Liu, B. Phillips, W. Li, **Z. Zhang**, L. Fang, J. Qiu, S. Wang. Fullerene-Tailored Graphene Oxide Interlayer Spacing for Energy-Efficient Water Desalination. ACS Applied Nano Materials, 1, (2018): 6168-6175
15. B. Wang, L. Wang, Xi Li, Y. Liu, **Z. Zhang**, E. Hedric, S. Safe, J. Qiu, G. Lu, S. Wang, Template-Free Fabrication of Vertically Aligned Polymer Nanowire Array on the Flat-end Tip for Quantifying the Single Living Cancer Cells and Nanosurface Interaction, Manufacturing Letters, 16, (2018): 27-31
16. L. Wang, Y. Liu, **Z. Zhang**, B. Wang, J. Qiu, D. Hui, S. Wang, Polymer composites-based thermoelectric materials and devices, Composites Part B: Engineering, 122, (2017): 145-155
17. S. Zhang, L. Zou, **Z. Zhang**, Y. Ma, Graphene Oxide Multilayers Films on Cotton Fabrics through Layer-by-Layer Assembly and Its Electromagnetic Shielding Property, Journal of Donghua University (Natural Science),42, (2016):1

CONFERENCE PAPERS

1. **Z. Zhang**, S. Wang. "Patient Decision Making for Traditional Vs. 3D Printing-Based Meniscus Transplantation." Industrial and systems engineering (2017)
2. Y. Zhang, F. Xu, W. Fan, **Z. Zhang**, Y. Qiu. Interface Property of the Carbon Fiber Treated by Ultralow Temperature, The 9th Asian-Australasian Conference on Composite Materials, (2014)
3. Y. Zhang, Q. Hu, **Z. Zhang**, Y. Zuo, F. Xu. Interface Modification of Kevlar fiber/epoxy resin by The Cryogenic Treatment, The 8th International Forum of Textile & Clothing, (2014)

APPENDIX B

SUPPORTING MATERIALS FOR CHAPTER III

Table B1 Peak temperature, enthalpy and peak value comparison

I-TI/I-Al	Peak Temperature (°C)	Peak Value (W/g)	Enthalpy (J/g)
2mol%/2mol%	125.5; 140.8	9.23	488.82
2mol%/0.25mol%	120.6	6.50	486.66
2mol%/0.1mol%	117.5	6.38	485.20
2mol%/0.05mol%	114.4	6.03	484.20
4mol%/0.05mol%	121.8	6.36	488.88
6mol%/0.05mol%	114.3	7.43	477.39
8mol%/0.05mol%	119.8	9.00	478.28

Table B2 Reaction kinetics

Formulation	Isothermal temperature (°C)	k_1 (s^{-1})	k_2 (s^{-1})	m	n	Ea_1 (KJ/mol)	Ea_2 (KJ/mol)
2mol%:0.05mol%	110	0.001529	0.037257	0.885952	0.865228	111.1	265.9233
	115	0.0044	0.444	1.598972	1.791471		
	120	8.78E-05	0.65104	1.10122	1.758904		
4mol%:0.02mol%	110	1.25E-04	0.026113	0.590306	0.876159	178.2605	88.75195
	117	0.001261	0.082631	0.925223	1.344448		
	124	0.001	0.088615	0.743798	1.795862		
4mol%:0.05mol%	110	1.59E-04	0.054814	0.733167	1.237788	149.0866	153.86641
	115	5.45E-04	0.088099	0.769273	1.10852		
	120	0.002474	0.147719	0.858645	1.340846		
4mol%:0.08mol%	105	1.23E-04	0.037193	0.680722	0.991282	118.4496	163.31111
	112	8.56E-04	0.090968	0.858187	1.317452		
	119	0.00272	0.194844	0.890598	1.458588		
4mol%:0.1mol%	105	1.99E-04	0.041844	0.703074	1.055444	91.02999	77.47817
	112	9.97E-04	0.111899	0.880767	1.272529		
	119	0.002149	0.317979	1.013651	1.595467		
6mol%:0.05mol%	105	8.40E-05	0.036777	0.722372	1.22801	160.8094	116.8948
	110	2.52E-04	0.037361	0.742807	1.058903		
	115	0.001756	0.334384	1.189611	1.651972		
8mol%:0.05mol%	110	8.82E-04	0.11311	1.04347	1.531281	76.50543	180.5718
	115	0.001799	0.127804	1.11098	1.329421		
	120	5.50E-06	0.658752	0.983246	1.837559		
4mol%:0.05mol% CNT0.2wt%	100	9.67E-04	0.017713	0.658167	0.779513	135.4351	147.9892
	104	1.97E-03	0.10052	1.907824	1.542325		
	107	0.000126	0.125917	2.302041	1.659094		
4mol%:0.05mol% CNT0.5wt%	100	2.35E-04	0.022241	0.599998	0.797121	134.0549	110.4184
	107	5.52E-04	0.070644	0.815058	1.461224		
	114	0.002521	0.195053	1.141462	1.667781		
4mol%:0.05mol% CNT1wt%	110	1.25E-04	0.517028	1.071335	1.701036	121.78425	118.56733
	115	4.36E-04	0.288846	0.695001	1.329272		
	120	4.45E-05	0.320405	0.602496	1.514928		

```
clc
Data = [
0.000101249 0.000158439
0.020851711 0.004087932
0.061418363 0.008729315
0.166766916 0.016133334
0.3011654 0.020371241
0.428805501 0.021610887
0.556461881 0.020742649
0.704026529 0.016089981
0.820570233 0.008309507
0.92594559 0.001379826
0.999162744 0.000282449


];
Data = real(Data);
alpha = Data(:,1);
dalpha_dt = Data(:,2);
plot(alpha,dalpha_dt,'ro');
F = @(x,xdata)x(1).*(1-xdata).^x(2)+(1-xdata).^x(2).*x(3).*xdata.^x(4);
x0 = [0 0 0 0];
lb=[0 0 0 0];
ub=[1000000000000 1000000000000 1000000000000 1000000000000];
[x,resnorm,~,exitflag,output] = lsqcurvefit(F,x0,alpha,dalpha_dt, lb,ub);
k1 = x(1), n = x(2), k2 = x(3), m = x(4);
hold on
plot(alpha,F(x,alpha))
hold off;
```

Figure B1 Coding script of model fitting in cure kinetics section

alpha	*11x1 double*
dalpha_dt	*11x1 double*
Data	*11x2 double*
exitflag	3
F	@(x,xdata)x(1).*(1-xd...
k1	8.9729e-04
k2	0.0947
lb	[0,0,0,0]
m	0.8877
n	1.2853
output	*1x1 struct*
resnorm	7.7614e-06
ub	[1.0000e+12,1.0000e+...
x	[8.9729e-04,1.2853,0....
x0	[0,0,0,0]

Figure B2 Demonstration of cure kinetics model output

Table B3 Comparison of potential energy consumption of Epoxy and DCPD in 2021-2025

		2020	2021	2022	2023	2024	2025	Energy CAGR	Intensity (MJ/kg)
DCPD	Revenue (million $)	861.6	865.908	870.23754	874.588728	878.961671	883.35648		
	Material consumption (kg)	27009404.4	27144451.4	27280173.7	27416574.5	27553657.4	27691425.7		
	Energy consumption (Oven Cure) (MJ)	1429337680	1436484369	1443666790	1450885124	1458139550	1465430248	0.50%[1]	53.92[3]
	Energy consumption (Frontal Cure) (MJ)	24855280.1	24979556.5	25104454.3	25229976.6	25356126.4	25482907.1		0.9202[4]
Epoxy Resin	Revenue (million $)	8036.50248	8506.63787	9004.27619	9531.02634	10088.5914	10678.774		
	Material consumption (kg)	252482013	267252211	282886465	299435323	316952290	335493999		
	Energy consumption (Oven Cure) (MJ)	1.3361E+10	1.4143E+10	1.497E+10	1.5846E+10	1.6773E+10	1.7754E+10	5.85%[2]	53.92[3]
	Energy consumption (Frontal Cure) (MJ)	273993481	290022099	306988392	324947213	343956625	364078087		1.0852[a]

Note B1: Calculation of energy consumption of different manufacturing processes

Revenue data (year 2020) of DCPD and epoxy resin are obtained from reference 1, 2, respectively. Revenue data for later years are calculated based on Compound Annual

Growth Rate (CAGR) of DCPD and epoxy resin in reference 1, 2, respectively. The material consumption is estimated from the revenue in consideration of unit price of the thermosetting polymer (shown in Table S6). Energy consumption (both oven cure and frontal cure) is estimated based on the values listed energy intensity column.

[a] calculated based on this work, specified in Note 1

Table B4 Comparison of market size and price of commercial thermosetting polymers

	Revenue (million $)	Unit Price ($/L)	Unit Price ($/kg)	Material Consumption (kg)	Density (g/cm3)	Revenue Reference	Unit price
DCPD	861.6	31.9	31198.2	27009404.39	0.978	[203]	Based 1L price, Sigma
Epoxy Resin	8036.5	31.83	36922.8	252482013	1.160	[204]	Based on 1L price, EPON 828

Note B2:

In this work, energy intensity of frontally cured and printed epoxy resin was calculated by the initial energy used for initiation of the epoxy curing process (determined by the power of heat source and temperature used for curing initiation, here, the reported number is calculated based on initial temperature of 120 °C). The showed energy intensity is based on the energy used to cure 100 cm^3 cuboid and measured weight. The process time is determined by the average printing speed for neat epoxy resin with I-TI/ I-Al ratio of 4mol%: 0.05mol%. Other values in Table B4 are obtained from or estimated based on the corresponding references.

Table B5 Comparison of energy consumption and mechanical performance of different manufacturing processes

	Energy (J)	Volume(cm^3)	Energy intensity (J/cm^3)	Tensile strengt (GPa)	Modulus (GPa)	Reference
FDM	-	-	394971.43	0.793	161.4	96, 27
FDM	-	-	394971.43	1.47	100.28	31, 27
FDM	-	-	394971.43	0.185	19.5	162, 27
FDM ABS	-	-	394971.43	0.155	8.6	92, 205
50 cm^3 DCPD	48.9	50	0.978	0.6	55	2
50 cm^3 epoxy resin	54.26	50	1.0852	1.147	85.1	This work
2000 cm^3 epoxy resin	54.26	2000	0.02713	1.147	85.1	This work
Conventional Oven Curing	-	-	56500	1.6	-	2, 164

APPENDIX C

SUPPORTING MATERIALS FOR CHAPTER IV

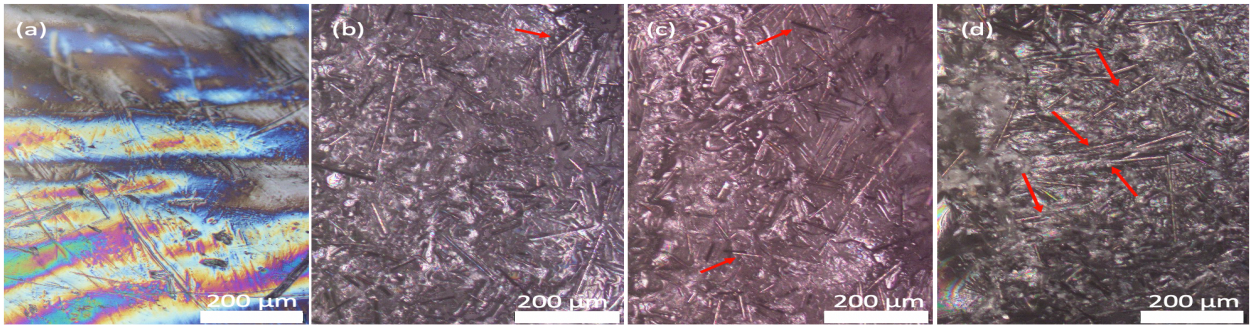

Figure C1 Optical micrographs of interfacial shear test fracture surface of (a) neat DCPD; (b)sized CF /DCPD; (c) CF-COOH/DCPD; (d) CF-Nb/DCPD.

Note C1: The optical microscope (OLYMPUS BX51) images of the interfacial shear test fracture surfaces for the four samples (neat DCPD, sized CF filled DCPD, carboxyl group grafted CF filled DCPD, norbornene group grafted CF filled DCPD) are shown in the Figure C1. It can be clearly observed the neat DCPD sample shows a smooth fracture surface compared to CF filled samples, which is a suggestion of weak interaction between printed layers. On the other hand, the fracture surfaces of fiber-filled samples (Figure (b), (c),(d)) are characterized with rougher fracture surfaces, indicating increased interlayer interactions. Additionally, the protruding fibers (marked by red arrows) were overserved with matrix residues on fiber surface, suggesting such short fibers ever bridged the printed interlayers for enhanced adhesive interactions between layers, and this led to the increasing interlayer bonding strength. These observations are consistent with the interlayer bonding tests as shown in Figure 4.16.

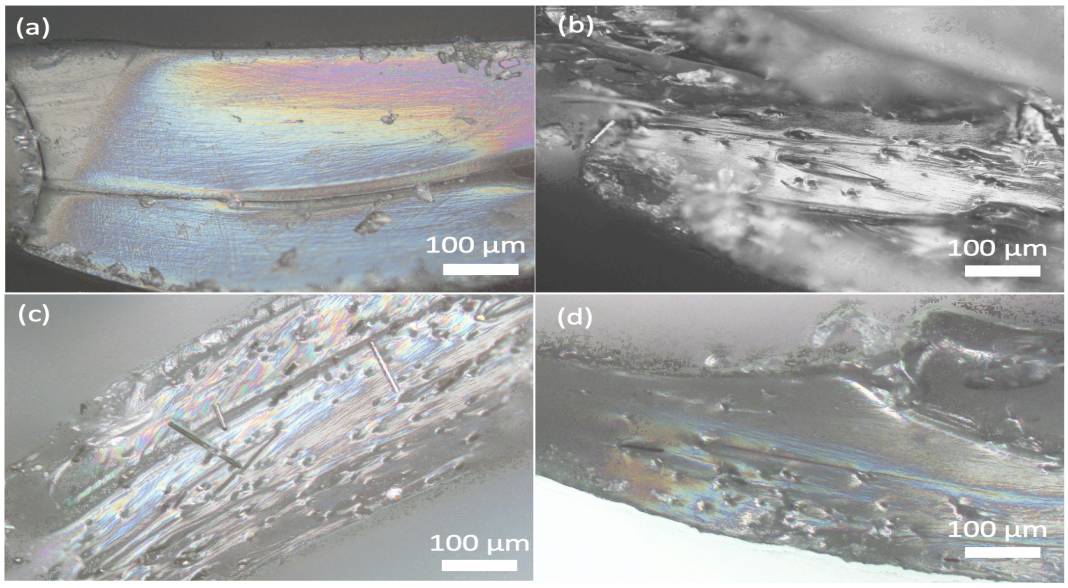

Figure C2 The cross-section tensile test samples were also characterized by microscopy. Optical micrographs of tensile test fracture surface of (a) neat DCPD ; (b) sized CF /DCPD; (c) CF-COOH/DCPD; (d) CF-Nb/DCPD.

Note C2: Neat DCPD sample (Figure 9 a) exhibit a smooth fracture surface while the fiber loaded samples (Figure C2b, c, d) showed much rougher fracture surfaces with numerous dimple structures. Such dimple rough fracture suggested micrometer-sized crack propagations were effectively prevented, owing to improved bonding between printed layers; otherwise, the continuous crack propagation would produce relatively smooth 'riverlike' patterns. These are in a good agreement with the tensile test results.

APPENDIX D

SUPPORTING TABLES IN CHAPTER V

Table D1 Changes in thickness after solvent exchange of the printed specimens

Sample composition(PA: AAm)	As Printed			After Solvent Exchange		
2:2	1.3208	1.22428	1.32588	1.69926	1.4224	1.67386
Average		1.290			1.599	
SD		0.057			0.153	
3:2	1.5748	1.270	1.4732	1.5494	1.1684	1.27
Average		1.439			1.329	
SD		0.155			0.197	
4:2	1.778	0.9652	1.27	1.6764		1.2954
Average		1.338			1.486	
SD		0.411			0.269	
3:1	1.524	2.3749	1.8034	1.3208	2.0574	1.905
Average		1.901			1.761	
SD		0.434			0.389	
3:3	1.2954	1.27	1.5494	1.27	1.3208	1.2954
Average		1.372			1.295	
SD		0.155			0.025	
3:2 MBAA 0.25%	1.651	1.27	1.524	1.7272	1.5748	1.8288
Average		1.482			1.710	
SD		0.194			0.128	
3:2 MBAA 0.75%	1.4986	1.2954	1.016	1.3716	1.143	1.397
Average		1.270			1.304	
SD		0.242			0.140	

Table D2 Statistical analysis of printed hydrogel

Table D2.1 Notation

Notation	A	B	C	D	E
Sample Composition (PA: AAm)	2:2	3:2	4:2	3:1	3:3

Table D2.2 Multiple comparison t-statistics of tensile strength

A vs B	A vs C	A vs D	A vs E	B vs C	B vs D	B vs E	C vs D	C vs E	D vs E
-5.33424	2.403845	4.598707	2.892530	7.174931	9.369792	8.226766	2.003625	0.183312	-2.01155
*		*		**	***	**			

Table D2.3 Multiple comparison t-statistics of tensile Young's modulus

A vs B	A vs C	A vs D	A vs E	B vs C	B vs D	B vs E	C vs D	C vs E	D vs E
-0.82228	-11.103	1.185481	1.313799	-10.3675	2.007764	2.136082	12.16331	12.27808	0.128318
	***			***			***	***	

Table D2.4 Multiple comparison t-statistics of toughness

A vs B	A vs C	A vs D	A vs E	B vs C	B vs D	B vs E	C vs D	C vs E	D vs E
- 50.8671 ***	26.02008 ***	47.7819 ***	25.8970447 ***	76.8871 ***	98.6490 ***	76.7641 ***	21.7618 ***	- 0.12303	- 21.8849 ***

Table D2.5 Multiple comparison t-statistics of water content after 1 hour exposure

A vs B	A vs C	A vs D	A vs E	B vs C	B vs D	B vs E	C vs D	C vs E	D vs E
-1.17771	18.92855	12.20614	0.319819	20.10626	13.38385	1.497526	-6.7224	-18.6087	-11.8863
	***	***		***	**		**	***	**

A vs B	A vs C	A vs D	A vs E	B vs C	B vs D	B vs E	C vs D	C vs E	D vs E
-7.73022	42.39926	15.09544	12.81157	50.12949	22.82566	20.54179	-27.3038	-29.5877	-2.28387
*	***	***	**	***	***	***	***	***	

Table D2.6 Multiple comparison t-statistics of water content after solvent exchange

Table D3 Multiple comparison t-statistics analysis

Table D3.1 Notation

Notation	1	2	3
Crosslinker concentration (wt%)	0.25	0.5	0.75

Table D3.2 Multiple comparison t-statistics of tensile strength (with different crosslinker concentration)

1 vs 2	1 vs 3	2 vs 3
-0.57347	-0.60409	-0.03062

Table D3.3 Multiple comparison t-statistics of tensile Young's modulus (with different crosslinker concentration)

1 vs 2	1 vs 3	2 vs 3
-0.25755	-1.13297	-0.87542

Table D3.4 Multiple comparison t-statistics of tensile strength (with different crosslinker concentration)

1 vs 2	1 vs 3	2 vs 3
3.855359	4.648083	0.792724
*	*	

Table D4 Level of significance determination

α	0.0005	0.001	0.0025	0.005	0.01	0.05	0.1
$t_{9,\frac{\alpha}{20}}$	7.87883246	7.215269	6.401855	5.829736	5.290654	4.145789	3.689662
$t_{8,\frac{\alpha}{20}}$	8.63962867	7.850647542	6.896254431	6.234038778	5.617410807	4.333549846	3.832518685
$t_{6,\frac{\alpha}{20}}$	11.57623354	10.26087355	8.729403402	7.707683999	6.78833999	4.980693514	4.316827104
$t_{5,\frac{\alpha}{6}}$	14.85599095	12.89282532	10.67277921	9.235494592	7.979653419	5.604165478	4.773340605
	***			**			*